

Azzollini, Francesco (2025) *Propagation of type III solar radio burst exciters and plasma density fluctuations.* PhD thesis.

https://theses.gla.ac.uk/85511/

Copyright and moral rights for this work are retained by the author

A copy can be downloaded for personal non-commercial research or study, without prior permission or charge

This work cannot be reproduced or quoted extensively from without first obtaining permission from the author

The content must not be changed in any way or sold commercially in any format or medium without the formal permission of the author

When referring to this work, full bibliographic details including the author, title, awarding institution and date of the thesis must be given

Enlighten: Theses
https://theses.gla.ac.uk/
research-enlighten@glasgow.ac.uk

Propagation of Type III Solar Radio Burst Exciters and Plasma Density Fluctuations

Francesco Azzollini MMathPhys

Submitted in fulfilment of the requirements for the Degree of Doctor of Philosophy

School of Physics and Astronomy

College of Science and Engineering

University of Glasgow



And you run, and you run to catch up with the Sun but it's sinking. And racing around to come up behind you again...

- Pink Floyd, Time

Abstract

Solar flare accelerated electron beams travel along open magnetic field lines in the solar corona and interplanetary (IP) medium and can interact with the local plasma to produce Langmuir waves and subsequently trigger intense radio emissions known as type III solar radio bursts. These bursts serve as a crucial diagnostic tool for advancing our understanding of electron transport in the inner heliosphere and as potential early indicators of hazardous space weather events. Despite the rapid quasilinear relaxation of electron beams towards a plateau in velocity space, observations suggest significant propagation distances, a challenge referred to as Sturrock's dilemma. Here, we develop a novel electron transport model by introducing a selfconsistently evolving quasilinear time/distance. The resulting nonlinear advectiondiffusion equation predicts super-diffusive, ballistic-like expansion of the beam; analytical predictions are consistent with the results of numerical simulations using kinetic equations and can account for some observed characteristics of type III solar radio bursts. A complementary analysis using spacecraft data from SolO/RPW, PSP/RFS, and STEREO-A/WAVES enables us to derive the speeds and accelerations of type III exciters from isolated bursts associated with flares of well-characterized angular positions. For the first time, this analysis allows the correction of velocities and accelerations for the angular separation between the spacecraft and the apparent source. The observed rate of change of velocity with heliocentric distance is then compared to theoretical predictions for a beam-plasma structure propagating through a background plasma of decreasing density, with energy loss attributed to the negative shift in velocity space of Langmuir waves and their subsequent absorption by the Maxwellian component of the plasma, shedding light on the mechanisms driving

energy dissipation in beam-plasma structures. Additionally, we investigate the impact of compressive waves in the turbulent solar atmosphere on radio wave propagation through the solar corona and solar wind. Using a new anisotropic density fluctuation model from the kinetic scattering theory for type III radio bursts, we infer the plasma velocities needed to explain observed spacecraft signal frequency broadening. At heliocentric distances beyond $10~R_{\odot}$, the velocities align with solar wind flows, while closer to the Sun ($\lesssim 10~R_{\odot}$), the broadening implies additional radial and transverse speeds consistent, respectively, with sound or proton thermal speeds and non-thermal motions measured via coronal Doppler-line broadening, interpreted as Alfvénic fluctuations. The energy deposition rates due to ion-sound wave damping peak at a heliocentric distance of $\sim (1-3)~R_{\odot}$ and are comparable to the rates available from a turbulent cascade of Alfvénic waves at large scales, suggesting a coherent picture of energy transfer, via the cascade or/and parametric decay of Alfvén waves to the small scales where heating takes place.

Contents

A	bstra	ct		ii	
List of Publications xv					
A	ckno	wledge	ements	XV	
D	eclar	ation		xvi	
1	Sola	ar Activ	vity: An Overview	1	
	1.1	To the	e Photosphere and Beyond	2	
	1.2	The A	Active Sun	3	
		1.2.1	Active Regions	4	
		1.2.2	Solar Flares	5	
		1.2.3	CMEs	ϵ	
		1.2.4	Jets	7	
		1.2.5	The Coronal Magnetic Field	7	
		1.2.6	Coronal Density Profile	Ģ	
	1.3	Densi	ity Inhomogeneities	11	
	1.4	Wave	s in plasma	12	
		1.4.1	Nonlinear Alfvénic Interactions and Turbulent Cascade	13	
		1.4.2	Velocity fluctuations and Alfvén wave cascade	14	
		1.4.3	Damping of ion-sound waves	15	
	1.5	Plasm	na Emission Mechanisms	17	
		1.5.1	Stages in Plasma Emission	17	
		1.5.2	Bump-in-Tail Instability	20	

		1.5.3 Sturrock's dilemma	21
	1.6	Solar Radio Bursts	23
	1.7	Type III	24
		1.7.1 Fine structures	27
		1.7.2 Type V	30
		1.7.3 Anisotropic Density Turbulence	30
		1.7.4 Inner and Outer Scales	33
	1.8	Instrument Overview	34
		1.8.1 Goniopolarimetric Techniques	34
		1.8.2 SolO and RPW	36
		1.8.3 STEREO-A and S/WAVES	37
		1.8.4 PSP and PSP/FIELDS(RFS)	38
		1.8.5 Wind and Wind/WAVES	39
2	Nor	llinear Diffusion with Advection of Flare Accelerated Electrons	41
	2.1	Kinetic description of electrons and Langmuir waves	42
	2.2	Hydrodynamic description	4 4
	2.3	Hydrodynamics with non-linear diffusion	46
		2.3.1 Advection and non-linear diffusion	49
	2.4	Asymptotic solution to advection-nonlinear-diffusion equation	54
		2.4.1 Initially finite beam dynamics	56
	2.5	Summary	60
3	A M	Iultispacecraft Analysis	
	and	Modeling of Type III Radio Burst Exciter Deceleration in Inhomo-	
	gen	eous Heliospheric Plasma	65
	3.1	Introduction	65
	3.2	Multi-spacecraft observations of type III burst sources	67
	3.3	Velocity and Acceleration	73
	3.3	velocity that received the rece	, ,

	3.5	Sumn	nary	84
4	Plas	sma mo	otions and compressive wave energetics in the solar corona	86
	4.1	Introd	luction	86
	4.2	Static	density fluctuations and angular broadening	89
	4.3	Inelas	tic scattering of radio waves	92
		4.3.1	Parallel propagating density fluctuations	93
		4.3.2	Transverse density fluctuations	94
		4.3.3	Random (turbulent) motions	95
	4.4	Obser	ved frequency broadening	98
	4.5	Frequ	ency broadening measurements	104
	4.6	Energ	y Cascade and Dissipation Rates	108
	4.7	Summ	nary and Discussion	111
5	Con	clusion	ns and Closing Remarks	115
	5.1	Closir	ng Remarks	117
Aj	ppen	dices		119
	A	Diffus	sion Tensor: Moving Density Fluctuations	119
		A. 1	Parallel Waves	119
		A.2	Perpendicular Waves	122
	В	Diffus	sion Tensor: Random Motions	123
		B.1	Random Motions Superimposed on a Static Background	123
		B.2	Random Motions Superimposed on Flows in a General Direction	n125

List of Tables

3.1	Parameters A_i [MHz s ^{-B}], B_i and t_{0i} [s] from Equation 3.4, where $i =$	
	F,H depending on whether fundamental or harmonic emission is assumed.	76
3.2	Parameters α_i [s ⁻¹] and β_i (top) from Equation 3.7, and γ_i [s ⁻²] and δ_i	
	(bottom) from Equation 3.8, where $i=F,H$ depending on whether fun-	
	damental or harmonic emission is assumed	78

List of Figures

1.1	Coronal density models from Allen (1947), Saito et al. (1977), Alvarez	
	and Haddock (1973b), Bougeret et al. (1984) and Leblanc et al. (1998).	
	The red curve represents the power law fit to the numerical solution to	
	the Parker model as shown in Kontar et al. (2019)	11
1.2	Flowchart showing the different stages of plasma emission. Figure adap-	
	ted from Melrose (2017)	18
1.3	One-dimensional representation of a bump-in-tail electron distribution	
	function. Electrons with sufficiently high energies can form a "bump" on	
	the high-velocity end of the distribution, referred to as an electron beam.	
	The positive slope in the beam distribution leads to instability and the	
	production of Langmuir waves	20
1.4	Artistic representation showing the five types of solar radio burst dy-	
	namic spectra. Image taken from Dąbrowski et al. (2016) and reproduced	
	under CC BY 4.0.	23
1.5	Dynamic spectra of the 07 July 2020 02:30 UT type III radio burst observed	
	by PSP (see Section 1.8.4)	24
1.6	Dynamic spectrum of a type IIIb burst on the 16 April 2015 captured	
	by both the LOw Frequency ARray (LOFAR, van Haarlem et al. (2013))	
	and the Ukrainian Radio interferometer of National Academy of Sciences	
	(URAN-2, Konovalenko et al. (2016)). A 3 s expanded view between 32-	
	36 MHz is shown at the bottom. Image taken from Kontar et al. (2017)	
	and reproduced under CC BY 4.0	28

1.7	q -space spectrum $q^2S(q)$ from Kontar et al. (2023): flat at energy-containing	
	scales; $q^{-5/3}$ in the inertial range between the outer scale $\ell_o=2\pi/q_o$ and	
	the inner scale $\ell_i=2\pi/q_i$; and $q^{-\delta}$ $(\delta>2)$ in the dissipation range. Image	
	taken from Kontar et al. (2023) and reproduced under CC BY 4.0	33
2.1	Figure 1 from Kontar et al. (1998) showing the result of the numerical sim-	
	ulations for the spreading of a monoenergetic electron beam in the weak	
	turbulence approximation. Here $v_0 \sim 10^{10}~{\rm cm~s^{-1}}$, with $v_{\rm min}$ of the beam	
	shown to be non-zero. The distribution function $f(\boldsymbol{v},\boldsymbol{x})$ here is plotted at	
	$t=3\mathrm{s}$ at different distances from the injection point	51
2.2	Electron number density profile $n(x,t)/n_b$ for the beam-plasma paramet-	
	ers as in the numerical simulations by Kontar et al. (1998): $n_b = 12 \text{ cm}^{-3}$,	
	$n_p = 6 \times 10^8 \ { m cm^{-3}}$ (i.e. $f_{pe} \simeq 220 \ { m MHz}$) and $v_0 = 10^{10} \ { m cm/s}$, $v_{ m min} = 0.1 v_0$,	
	$d=3\times 10^9$ cm. The three curves are the density profiles given by the	
	solution (Equation 2.59) for $t=0.5,3,6$ seconds. Figure made by Eduard	
	P. Kontar	58
2.3	<i>Top panel:</i> Electron number density profile $n(x,t)/n_b$ at $t=0,20,40,60$ second	ds
	for the same beam plasma parameters as in Figure 2.2 $n_b=12~{\rm cm}^{-3}$	
	in black and $n_b=60~{\rm cm}^{-3}$ in red . Bottom panel: FWHM width of the	
	beam given by equation 2.61 (solid line). The dashed line is the width	
	of Lorentzian (Equation 2.55). The horizontal dashed line is Gaussian	
	FWHM, $\Delta x_G \simeq 1.67d$. Black lines are for $n_b = 12~{\rm cm}^{-3}$ and red lines	
	are for $n_b = 60 \text{ cm}^{-3}$. Figure made by Eduard P. Kontar	62
2.4	Simulated electron distribution $f(x, v, t)$ (left), spectral energy density	
	W(x,v,t) (center), and electron beam density $n(x,t)$ (right) at three time	
	moments $t=0.5,3,6$ s for the following beam–plasma parameters: $n_b=$	
	12 cm $^{-3}$, $n_p = 6 \times 10^8$ cm $^{-3}$ (i.e., $f_{pe} \simeq 220$ MHz), $v_0 = 10^{10}$ cm/s,	
	$v_{\rm min}=0.1v_0$, and $d=3\times10^9$ cm. The analytical density profile (2.59)	
	is plotted in red, with the black dashed line showing its peak as a func-	
	tion of distance	63

2.5	The same as Figure 2.4 but for $n_b = 120 \text{ cm}^{-3}$	64
3.1	Dynamic spectra (left) and frequency-time (right) on the 11 July 2020	
	by the PSP, STEREO-A and SolO spacecraft (from top to bottom). For	
	each spacecraft, the peak flux frequencies (and the fit) are plotted on the	
	right for the times-frequencies selected by the green dashed box, contain-	
	ing peak flux points (green "X" symbols), along with their fitted curve	
	(green dashed line), while the χ^2 -fitted positions of the emitter as a func-	
	tion of time, obtained by using the density model from Equation (3.5),	
	and the normalized residuals from the fit are shown on the right. Blue	
	and red lines correspond, respectively, to the fundamental and harmonic	
	components. The steepening of the PSP profile may be attributed to scat-	
	tering projection effects	68
3.2	Type III burst peak fluxes measured by the four different spacecraft (left),	
	as well as spacecraft positions (right) in HEE coordinates during the 11	
	July 2020 (2:30 UT) event. The direction of maximum directivity is found	
	by fitting Equation 1.20 for the peak fluxes from STEREO-A, PSP, Wind	
	and SolO at 979 kHz. This frequency was selected on the assumption that	
	for $\gtrsim 1$ MHz, the Sun's magnetic field is approximately radial. In this re-	
	gion, radio waves are subject to anisotropic scattering, with the anisotropy	
	aligned along the heliospheric magnetic field (Clarkson et al. 2025). As	
	a result, the propagation of the waves is preferentially guided along the	
	magnetic field, leading the apparent radio sources to appear shifted in the	
	radial direction. On the left peak fluxes are plotted as a function of HEE	
	Longitude. The red dashed line shows the position of the radio source as	
	revealed by the directivity fit. On the right are the position of Solar Or-	
	biter, Parker Solar Probe, STEREO-A and Wind projected in the plane of	
	the HEE coordinate system	69
3.3	Dynamic spectra of the 11 July 2020 02:30 UT type III radio burst observed	
	from STEREO-A, SolO, Wind and PSP	70

3.4	Type III exciter propagating from position r_1 to r_2 with constant velocity	
	v_s at an angle ϕ to the line of sight. This simple representation allows to	
	correct for the source-to-spacecraft light travel time (Equation 3.1)	71
3.5	Exciter velocities and accelerations from the 11 July 2020 type III burst for	
	the PSP, STEREO-A and SolO spacecraft (from top to bottom). Blue and	
	red lines correspond, respectively, to the fundamental and harmonic com-	
	ponents. Velocity as a function of frequency is shown on the left, where	
	the shaded areas show velocities deduced from Krupar et al. (2015) us-	
	ing STEREO-A and STEREO-B data. Median values are shown with trans-	
	parent solid (STEREO-A) and dashed (STEREO-B) lines. On the centre	
	and right, velocity and acceleration of the exciter are plotted as a func-	
	tion of distance. Black dashed lines correspond to the result from Equa-	
	tion 3.20, where x_0 corresponds to the location where the highest analysed	
	frequency is emitted	74
3.6	The same as Figure 3.1 (top) and Figure 3.5 (bottom), but for the 21 July	
	2020 event observed by the STEREO-A spacecraft	75
3.7	The same as Figure 3.2 but for the 21 July 2020 event observed by the	
	STEREO-A spacecraft	75
3.8	MCMC method applied to the 21 July 2020 event observed by STEREO-	
	A. Spread in parameter space provides standard deviation for fitted para-	
	meters A, B and C (here denoting parameter t_0)	77

	are represented by lines different color shades, with darker to lighter shades	
	being associated to PSP, STEREO-A and SolO, respectively. Blue and red	
	shades are associated to fundamental and harmonic emission, respect-	
	ively. The top row displays fundamental emission, while the bottom row	
	represents the harmonic component. The events of July 11, 2020, and July	
	21, 2020, are distinguished using dots and crosses as markers, respectively.	
	Shaded regions represent the results from the Krupar et al. (2015) ana-	
	lysis, with median values showcased by the transparent solid (STEREO-	
	A) and dashed (STEREO-B) lines	79
4.1	Wavevector coordinate system used in our analysis; the radio wave, with	
		90
4.2	The left panel shows the Sun-centered coordinate system and its relation	
	to heliocentric distance and the line of sight from a distant point source.	
	The broadening of point sources is calculated as an integral along z . The	
	right-hand panel qualitatively shows how the $D_{\perp_2\perp_2}$ diffusion tensor com-	
	ponent (see e.g., Equation (4.8)) varies along the direction of propaga-	
	tion of the radio wave (z) , as illustrated for sources at two different helio-	
	centric distances $r(z=0)$, with $r_1 < r_2$. Figure made by Daniel L. Clarkson.	98
4.3	Left: Observed spectral broadening $\Delta f = \sqrt{\langle \Delta f^2 \rangle}$ (the square root of the	
	variance) of spacecraft signals observed through the corona from various	
	studies, where each carrier signal is scaled to $f=1$ GHz using $\Delta f/f \propto$	
	$1/f^2$. Right: Form of Δf derived from Equations (4.23) and (4.24), for	
	$v_{\perp}=30{\rm kms^{-1}}$, and $v_{\parallel}=\sqrt{v_s^2+v_{ m sw}^2}$, where the sound speed v_s is given by	
	Equation (4.27) and the solar wind speed $v_{\rm sw}$ is given by Equation (4.28).	
	The solid and dashed lines show Δf derived using $1 \times \overline{q \epsilon^2}$ for $\alpha = 0.25$	
	and $\alpha = 0.4$, respectively, while the grey area shows the range in Δf . The	
	and $\alpha=0.4$, respectively, while the grey area shows the range in Δf . The lower bound is given by $1/2 \times \overline{q \epsilon^2}$ for $\alpha=0.25$, and the upper bound is	

3.9 Velocities and accelerations deduced from PSP, STEREO-A and SolO data

- 4.4 **Left:** Plane-of-sky velocity $v_{\perp k}$ calculated using frequency broadening measurements from Figure 4.3, Equation (4.37), and the $n^2 \overline{q \epsilon^2}$ values at various distances r derived from measurements of other phenomena, such as angular broadening of extra-solar sources and the location, size and timing of solar radio bursts (Kontar et al. 2023). The green and red points show the conversion of individual Δf data points from Figure 4.3, for different values of α , with binned averages and weighted uncertainties on each bin. **Middle:** Parallel and perpendicular velocities v_{\parallel} (blue) and v_{\perp} (black) required to solely explain the frequency broadening measurements in Figure 4.3. The grey dots and stars show a summary of the measured values of the non-thermal velocity standard deviation from the right panel. Also shown is the solar wind speed v_{SW} (Equation (4.28)), the ion-sound speed v_s (Equation (4.27)), and the Alfvén speed from Equation (4.38), obtained using the density and magnetic field models in Kontar et al. (2023), i.e. Equations (1.3,1.2). **Right:** 1σ non-thermal velocities $v_{\rm nth}$ from line-of-sight Doppler broadening of coronal lines. Figures
- 4.5 **Left:** Available power per unit mass, $\epsilon_{\ell_{\perp}}$ (erg g⁻¹ s⁻¹) from Equation (1.4), using perpendicular velocity fluctuations from Figure 4.4. The solid and dashed lines correspond to the range (20-70) km s⁻¹ (black) from frequency broadening measurements, and (20-40) km s⁻¹ for $r < 1.4\,R_{\odot}$ for non-thermal velocities from coronal lines (red). **Right:** Coronal heating rate per unit mass (erg g⁻¹ s⁻¹) from Landau damping of ion-sound waves given by Equation (1.10). As in the right panel of Figure 4.3, the solid and dashed lines show $1 \times \overline{q} \, \overline{\epsilon^2}$ for $\alpha = 0.25$ and $\alpha = 0.4$, respectively, and the grey area corresponds to the range of values $[1/2,2] \times \overline{q} \, \overline{\epsilon^2}$, considering both values of α . Figures made by Daniel L. Clarkson.

106

109

List of Publications

- Kontar, E. P., Azzollini, F., Lyubchyk, O. Advection-nonlinear-diffusion Model of Flare Accelerated Electron Transport in Type III Solar Radio Bursts. Astrophysical Journal, 976(2), 233 (2024). doi:10.3847/1538-4357/ad8560
- Azzollini, F., Emslie, A. G., Clarkson, D. L., Chrysaphi, N., Kontar, E. P. *Plasma Motions and Compressive Wave Energetics in the Solar Corona and Solar Wind from Radio Wave Scattering Observations*.
 - Astrophysical Journal, 968(2), 72 (2024). doi:10.3847/1538-4357/ad4154
- Chen, X., Kontar, E. P., Chrysaphi, N., Zhang, P., Krupar, V., Musset, S., Maksimovic, M., Jeffrey, N. L. S., Azzollini, F., Vecchio, A. Source positions of an interplanetary type III radio burst and anisotropic radio-wave scattering. Astronomy & Astrophysics, 680, A1 (2023). doi:10.1051/0004-6361/202347185
- Kontar, E. P., Emslie, A. G., Clarkson, D. L., Chen, X., Chrysaphi, N., Azzollini,
 F., Jeffrey, N. L. S., Gordovskyy, M. An Anisotropic Density Turbulence Model from the Sun to 1 au Derived from Radio Observations. Astrophysical Journal, 956(2), 112 (2023). doi:10.3847/1538-4357/acf6c1
- Azzollini, F., Kontar, E. P. A Multi-spacecraft Analysis and Modelling of Type III Radio Burst Exciter Deceleration in Inhomogeneous Heliospheric Plasma. The Astrophysical Journal (2025). doi:10.3847/1538-4357/adee22

Acknowledgements

I would like to start by expressing my gratitude to my supervisor, Professor Eduard P. Kontar. Your expert guidance and support over the past four have been truly invaluable.

Thank you to the Science and Technology Facilities Council (STFC) for their funding that allowed me to embark on this journey.

A special thanks goes to the whole family of 604, and in particular to Dr. Daniel L. Clarkson, who somehow managed to stand four long years of me pestering him with questions. Thanks for always being there for me, I look forward to our next coffee together.

I would like to thank my family for always believing in me, even when I could not believe in myself. Thanks to my dog Leon for always being such a good boy. I would also like to thank the many true friends, both Scottish and Italian, who have supported me throughout these four years of madness, shaping my time in Glasgow into an experience I will never forget.

Last but not least, a big thank you goes to Sophia for keeping me sane throughout this past year. You've been the sun shining through even in the cloudier Glasgow day. Ti amo.

Declaration

I declare that, except where explicit reference is made to the contribution of others
that this dissertation is the result of my own work and has not been submitted for
any other degree at the University of Glasgow or any other institution
Francesco Azzollini

Chapter 1

Solar Activity: An Overview

Introduction

This thesis seeks to investigate the dynamics of solar flare-accelerated electron beams and their interactions with the surrounding plasma. Particular attention will be given to the mechanisms responsible for energy dissipation and diffusion-advection in beam-plasma structures. The investigation also includes the impact of compressive waves in the turbulent solar atmosphere on spacecraft radio signal propagation, providing a more detailed understanding of the energy transfer mechanisms responsible for coronal heating. This introductory chapter reviews the fundamental concepts of solar physics and outlines the practical motivations behind continuing research on space weather. After a general overview, the chapter discusses the underlying physics of electron transport, with particular focus on Langmuir wave general

tion, followed by a description of the properties of type III solar radio bursts, placing particular emphasis on the importance of scattering on observed burst characteristics. The Section ends with an overview of the instruments and spacecraft utilized throughout this work.

1.1 To the Photosphere and Beyond

The best place to start this journey throughout the solar atmosphere is by defining its five constituent layers. These are characterized in terms of varying temperature and density (McLean and Labrum 1985), beginning from the *photosphere*. At $1R_{\odot}$ (i.e. 1 solar radius $\approx 6.96 \times 10^5$ km) from the solar center, this layer is visible to the human eye and is commonly perceived to be the "surface" of the Sun. Here temperatures are generally considered to be around ~ 5780 K, depending on heliocentric distance. Moving outwards from this innermost layer, temperature and density decrease with increasing distance until, at the height of ~ 2000 km above the solar surface, temperature reaches a local minimum. This marks the starting point for the net layer, the 'chromosphere'. In this layer temperature begins gradually rising again, increasing more steeply towards the outer chromospheric edge, where it reaches ~ 25000 K (McLean and Labrum 1985). In a \sim 100 km wide region at the very end of the chromosphere, generally referred to as the transition region, temperatures can reach orders of magnitude of $\sim 10^6$ K (McLean and Labrum 1985), while density keeps dropping, decreasing by two orders of magnitude (Aschwanden 2004). This region and what lies beyond it have been subject of intense investigation in solar physics for over 80 years. In fact, as the journey continues past the transition region and into the 'corona', the largest layer of the Sun, density keeps decreasing, while temperature defies all expectations and keeps increasing with heliocentric distance, reaching 1-2 $\times 10^6$ K (Aschwanden 2004). This puzzling phenomenon is commonly referred to as the "coronal heating problem". The corona pervades all interplanetary space as the solar wind, a constant stream of charged particles (protons, electrons, α particles, and heavy ions) originating by two different coronal environments: the open corona, from which the fast solar wind (800 km s^{-1}) originates, is associated with coronal holes and open magnetic field lines, while the closed corona, where the slow solar wind (500 km s^{-1}) originates, is associated with loops and streamers (McLean and Labrum 1985). The solar wind has been the reason behind many solar missions, seeking to study its properties in-situ. A few notable mentions are the Wind spacecraft (Section 1.8.5), the STEREO mission, comprising of spacecraft STEREO-A and STEREO-B (Section 1.8.3), as well as the more recently launched Solar Orbiter (SolO) (Section 1.8.2) and Parker Solar Probe (PSP) (Section 1.8.4).

1.2 The Active Sun

This Section offers an overview of the practical reasons as to why many have ventured into the study of the coronal environment, where a wide variety of events can significantly impact Earth and near-Earth environment. Collectively, these events are commonly referred to as 'space weather', encompassing a multitude of factors. Solar energetic particles (SEPs), coronal mass ejections (CMEs) (Section 1.2.3), solar flares (Section 1.2.2), and excessive radio noise, to name just a few. These can lead to geomagnetic storms and ionospheric disturbances, putting power grids and communication infrastructure at risk and leading to substantial financial damage (Gary and Keller 2004).

1.2.1 Active Regions

The dynamic nature of the Sun is largely dictated by changes in its magnetic field. The latter is believed to originating from the solar dynamo (Parker 1955a), a phenomenon driven by plasma flows and differential rotation, particularly near the tachocline (region at base of the convection zone, where hot plasma rises and cooler plasma sinks) (Dikpati 2004). Magnetic buoyancy causes the magnetic field lines to rise, emerging from the photosphere, while the Sun's differential rotation causes the field to wrap around the Sun (Parker 1955b). As the cycle progresses, these magnetic fields become increasingly twisted by differential rotation and convective flow, leading to a slow reconfiguration and an eventual "flip" in polarity, determining periods of maximum and minimum solar activity, respectively referred to as "solar maximum" and "solar minimum". Over this 22 year long solar cycle (two 11-year cycles for magnetic polarity to return to its original orientation) areas of intense solar activity are formed, called 'active regions'. They appear at roughly $\pm 30^{\circ}$ from the solar equator, emerging further north and south early in the cycle and progressively moving closer to the equator, and can last for weeks, reaching maximum activity $\sim 10-15$ days after their formation (Priest 2014). In general, active regions are characterized by enhanced coronal densities and temperatures, believed to be caused by increased magnetic field strength (McLean and Labrum 1985), and present a bipolar magnetic field structure, with plasma connecting two spots of opposing polarity and forming arching features extending far into the corona. Although the overlying magnetic activity leads to elevated temperatures and densities, the concentrated magnetic field in their center suppresses heat transfer by convection, causing the appearance of darkened regions. These same regions, commonly known as "sunspots" have been subject of study since the very first telescopes. They comprise a darker inner area called "umbra" and a lighter outermost boundary called "penumbra" (McLean and Labrum 1985). Magnetic fields near-horizontal to the solar surface can support clouds of gas

cooler than the ambient coronal plasma, known as *filaments* (McLean and Labrum 1985). Another common feature of active regions, these are characterized by lengths of the order of 10 Mm, densities greater than 10^{11} cm⁻³ and relatively stronger magnetic fields. When they extend above the limb they are referred to as prominences, instead (McLean and Labrum 1985; Priest 2014).

1.2.2 Solar Flares

As formulated by Parker (1957) and Sweet (1958), magnetic reconnection provides an efficient mechanism for releasing stored magnetic energy by reconfiguring the field into a lower-energy state. This violent energy release is known as a *solar flare* and is the most energetic phenomenon in the solar system, accompanied by a sudden brightening near the active region, visible from decameter radio wavelengths to gamma-rays (Benz 2017). Lasting from minutes to tens of minutes, this phenomenon is a proficient particle accelerator, releasing approximately 10^{32} ergs of energy and 10^{36} of electrons per second, with a non-thermal accelerated electrons component (energies ranging between tens and hundreds of keV) being one of the primary features in solar flares (Emslie et al. 2005, 2012). Solar flares are classified based on their peak X-ray flux in the 1-8 Å band, as measured by the GOES spacecraft. and divided into five categories: A, B, C, M, and X. Each class is further subdivided into levels from 1 to 9 (Fletcher et al. 2011).

1.2.3 CMEs

Coronal mass ejections (CMEs) are another result of magnetic field reconfiguration, i.e. magnetic reconnection. These spectacular eruptions are regarded to be the largest-scale eruptive phenomenon in the solar system, with a release of energy comparable to that of solar flares and projected velocities ranging between 20 and 2000 km $\rm s^{-1}$ (Yashiro et al. 2004; Emslie et al. 2004). These impressive events start from coronal-loop-sized scales and propagate far into the heliosphere and into interplanetary space, reaching angular widths from a few degrees up to 1200 (Chen 2011; Schwenn 2006). However, such observed angular widths can be significantly affected by projection effects and instrumental artifacts, e.g. "halo" CMEs of 360° angular width are due to the CME propagating along the Sun-Earth line, hiding the true angular width in coronagraph observations (Yashiro et al. 2004; Chen 2011). One of the most debated topics in solar physics is the association between solar flares and CMEs. The debate on correlation between solar flares and CMEs is ongoing and spans several decades of scientific debate, with works from Harrison (1995) and Andrews (2003) finding an increased association between CMEs and solar flares surpassing typical peak flux, total flux, and event duration thresholds. On the other hand, Andrews (2003) found class-M flares to be associated to CMEs only in 40% of cases. Yashiro et al. (2006) found an increasing CME association rate with flare peak flux, fluence, and duration, with nearly all X-class and long-duration (≥180 min) flares having CMEs. Large scale shock fronts, consisting of a dense leading edge and a region of depleted density preceding the CME, are a common byproduct of CMEs, locally accelerating electrons and exciting in situ plasma emissions (see type II radio bursts 1.6) (Wild and McCready 1950).

1.2.4 Jets

Resulting from magnetic reconnection (Shibata et al. 1992; Shibata et al. 1994; Kundu et al. 1998), solar *jets* are narrow, beam-like plasma ejections that propagate along straight (or oblique) magnetic field lines. These events can arise in various solar environments, including active regions, coronal holes, and quiet-Sun areas (Shen 2021), and are often linked to type III radio bursts (Section 1.7). They are often simultaneously visible across multiple wavelength ranges, i.e. $H\alpha$, extreme ultraviolet (EUV), and X-ray, and their widths can range from a few hundred to several hundred thousand kilometers (Shen 2021; Chen et al. 2013; Mulay et al. 2016; Kundu et al. 1995). Analyzing SDO observations of EUV active region jets, Mulay et al. (2016) found velocities and lifetimes ranging between 87-532 km s⁻¹ and 5-39 min. In particular, type III burst centroids are often found to be aligned with soft X-ray (Kundu et al. 1995) and EUV jets (Chen et al. 2013), suggesting that particle acceleration can occur during a coronal jet event.

1.2.5 The Coronal Magnetic Field

In the corona, the magnetic pressure $P_B = \frac{B^2}{8\pi}$, with magnetic field B, dominates over the gas pressure, largely shaping the coronal environment. Relative dominance of magnetic or plasma pressure in a given region is described by the plasma beta parameter:

$$\beta = \frac{P_{\text{GAS}}}{P_B} = \frac{n \, k_B T_e}{B^2 / 8\pi},\tag{1.1}$$

where T_e is the electron temperature and n is the total particle number density. When $\beta < 1$, the magnetic pressure dominates, confining the plasma to local magnetic field structures. In the solar corona, β ranges between 10^{-1} and 10^{-4} (McLean and Labrum 1985), hence the appearance of coronal loops and other magnetic structures.

From values > 1 in the photosphere, β falls to a minimum ($\beta << 1$) in the mid-corona and gradually rises up again in the upper corona. Here, regions of comparable magnetic and gas pressure are of particular interest, resulting in complex interactions that may play a role in coronal heating (see Chapter 4) (Alfvén 1947).

Strength and structure of the magnetic field can only be studied through indirect methods, one of the most important being the Zeeman effect. This method relies on the splitting of spectral lines into multiple components in the presence of a magnetic field, and is routinely used to infer magnetic field strength in the photosphere (Gary 2001). Indirect coronal magnetic field measurements have been carried out using a variety of techniques, including coronal loop seismology (De Moortel et al. 2016) and long-duration observations of waves in the solar corona (Tomczyk and McIntosh 2008). A recent work by Landi et al. (2020) exploits magnetic field driven mixing of pseudo-degenerate energy states in Fe X, to obtain an estimate of the coronal magnetic field. Radio observations of gyrosynchrotron emission from non-thermal electrons in coronal loops offer a different perspective due to the emission mechanism being intrinsically dependent on the magnetic field strength (Nindos et al. 2000; White et al. 2002).

This work makes extensive use of a model for the magnetic field above a sunspot umbra presented by Gary (2001), with parameters selected to match both observations and extrapolations in different coronal regions. The model takes analytical form

$$B(r) = \frac{2500 \,\mathrm{G}}{(1 + r/0.0007R_{\odot})^3} + \frac{50 \,\mathrm{G}}{(1 + r/0.1R_{\odot})^3} + \frac{1 \,\mathrm{G}}{(1 + r/1R_{\odot})^3}$$
(1.2)

where r represents the height above the umbra, extending to a height of approximately $14 R_{\odot}$.

1.2.6 Coronal Density Profile

A reliable electron density model can play a fundamental role in interpreting solar and heliospheric observations, especially when dealing with radio emission. Initial coronal density measurements relied on white-light observations, analyzed under the assumption that polarized white light is proportional to the line-of-sight integrated coronal electron density. (van de Hulst 1950). This technique defined three main coronal emission components: the continuous emission of the K-corona, due to photospheric light scattering off free electrons (this dominates close to the Sun), the L-corona, consisting of spectral line emission from highly ionized atoms (dominates until 0.5 R_{\odot} above the solar surface), and the F-corona, a result of light being scattered by interplanetary dust particles. Because this is scattered photospheric emission, the F-coronal spectrum retains the photospheric Fraunhofer absorption lines. Another method to infer coronal densities from ground-based observations relies on analyzing the frequency of radio bursts as they propagate through the corona, under the assumption that the emission frequency corresponds to either the fundamental or harmonic plasma frequency, directly related to the electron density through $f_{\rm pe} \simeq 8.9 \sqrt{n_e}$ [kHz] (Leblanc et al. 1998). A more recent approach employs space-based observations in the extreme ultraviolet (EUV) and soft X-ray

wavelengths to obtain coronal density measurements based on emission measure, a quantity proportional to the squared density integrated along the column depth (Aschwanden 2004). Different coronal density profiles have been deduced, depending on whether density measurements were conducted for quiet Sun or above an active region, or at different latitudes. Newkirk (1961) provides one of the most commonly used density models to date, derived from observations of the upper corona $(<3R_{\odot})$ during solar maximum. Density can also depend on latitude, with increased densities found near the solar equator and lower densities close to the poles (van de Hulst 1950). Particle density in the corona is observed to range widely, with values of $<10^6-10^7~{\rm cm^{-3}}$ in the upper corona $(1~R_{\odot})$ and $(1-2)\times10^8~{\rm cm^{-3}}$ at the base (2500) km) of the quiet corona, climbing up to $(3-5)\times 10^8~{\rm cm}^{-3}$ in coronal streamers and $2 \times 10^8 - 2 \times 10^9$ cm⁻³ in active regions (Aschwanden 2004). The following chapters make extensive use of a spherically symmetric, isothermal density model based on Parker's solar wind solution (Parker 1960) with parameters defined by satellite density measurements at 1 AU (Mann et al. 1999) and temperature set to 1 MK. A simple analytical form of this model is found in Kontar et al. (2019) by fitting three power law functions

$$n_e(r) = 4.8 \times 10^9 \left(\frac{R_{\odot}}{r}\right)^{14} + 3 \times 10^8 \left(\frac{R_{\odot}}{r}\right)^6 + 1.4 \times 10^6 \left(\frac{R_{\odot}}{r}\right)^{2.3} \text{ [cm}^{-3]}, (1.3)$$

where r is the heliocentric distance and n_e has units of cm⁻³, and unlike Newkirk (1961), is valid both close to the Sun and at near-Earth heliocentric distances.

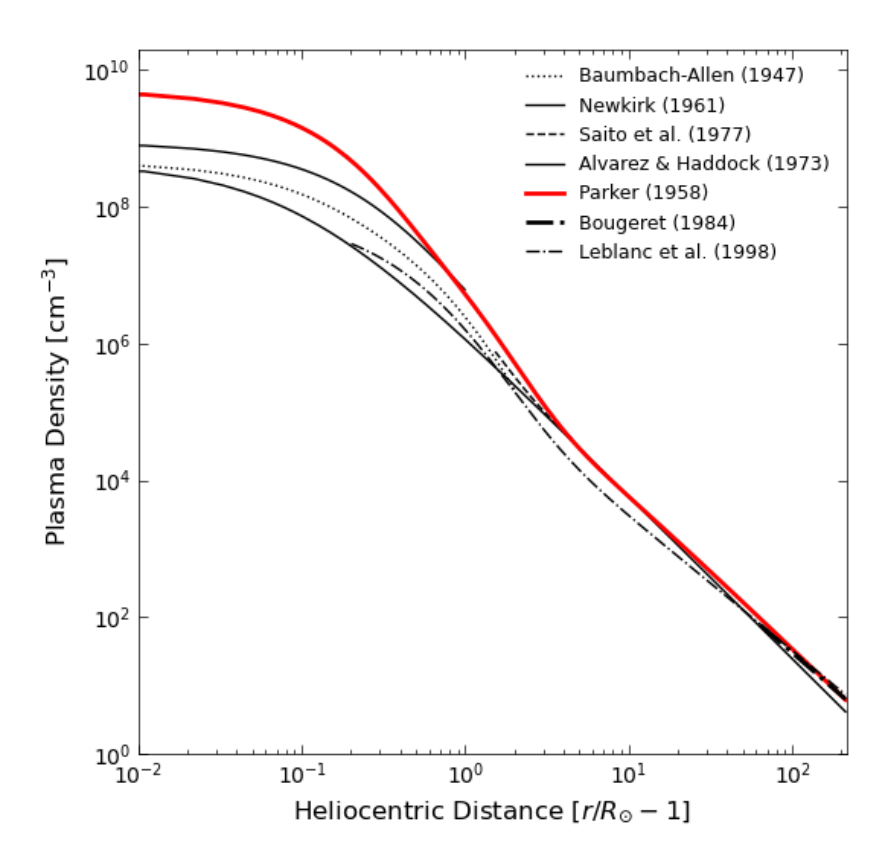


Figure 1.1: Coronal density models from Allen (1947), Saito et al. (1977), Alvarez and Haddock (1973b), Bougeret et al. (1984) and Leblanc et al. (1998). The red curve represents the power law fit to the numerical solution to the Parker model as shown in Kontar et al. (2019).

1.3 Density Inhomogeneities

Despite the smooth picture painted by Figure 1.1, density inhomogeneities in the corona and solar wind occur across a wide range of scales and are often observed in-situ by spacecraft, providing the magnitude of their fluctuation. They can be remotely detected through the radiation pattern of non-solar radio waves emitted from radio sources (~ 1 arcsec), scattered by small-scale (10^1 - 10^3 km) electron-density fluctuations in the solar wind plasma. This phenomenon is known as interplanetary scintillation (Mejia-Ambriz et al. 2015) and has often been studied in connection to small-scale plasma density fluctuations and frequency broadening of spacecraft signals (e.g. Woo and Armstrong 1979). From the phase shift of radio signals trans-

mitted between two spacecraft in near-Earth orbit, Celnikier et al. (1983) inferred average density fluctuations of 10% ($\delta n_e/n_e$) over a three-hour period. Closer to the Sun, the level of density inhomogeneity can only be studied through remote-sensing techniques. For instance, Sasikumar Raja et al. (2017) used the anisotropic angular broadening of radio observations of the Crab nebula to infer an increased level of electron density fluctuations, ranging approximately from 0.19% to 0.77% within the 9-20 R_{\odot} region.

1.4 Waves in plasma

In order to talk about plasma motions in the corona, this section very broadly introduces the three propagating normal modes in ideal, homogeneous magnetohydrodynamics (MHD), as well as two processes that might be responsible for energy cascading from large-scales to smaller-scales, where it is eventually dissipated.

Shear *Alfvén waves*, described by Alfvén (1942), are non-compressive waves, meaning they do not directly affect the density of the plasma, propagating along the magnetic field lines, with the ions and the magnetic field oscillating perpendicular to the background field direction (transverse). In these waves, magnetic tension acts as the restoring force and wave propagation is confined to a direction along the magnetic field (Aschwanden 2004). Many models for coronal heating propose Alfvén waves as a driver for heating the solar atmosphere. However, more recent works have provided evidence suggesting that irregularities in the solar wind consist both of waves and turbulence (Hollweg 1990; Verscharen et al. 2018).

The other two modes are known as *slow and fast magneto-sonic waves* and they are both compressive waves, though the degree of compressibility depends on the plasma β and their angle of propagation relative to the magnetic field. The former can often be described as sound waves guided by a nearly rigid magnetic field (in low- β plasmas) (Hollweg 1990). These generally propagate at slower speeds than the other two MHD wave modes in low- β conditions, preferentially along the magnetic field direction. Fast magneto-sonic waves are the fastest MHD modes considered here. They can propagate at any angle relative to the magnetic field and could be described as a combination of plasma density and magnetic field perturbations. Contrary to slow magneto-sonic waves, fast magneto-sonic waves behave predominantly as acoustic in high- β conditions and magnetic in low- β conditions (Aschwanden 2004).

1.4.1 Nonlinear Alfvénic Interactions and Turbulent Cascade

Alfvén parametric decay is a nonlinear process in which Alfvén waves can interact with density fluctuations and other compressive disturbances in the plasma, producing a range of magnetoacoustic and Alfvén waves moving both towards and opposite to the original direction of propagation. Eventually, this can lead to an energy cascade towards smaller scales. Originally, Sagdeev and Galeev (1969) showed that Alfvén waves of finite-amplitude can undergo parametric decay into a backward-propagating Alfvén wave and a compressive perturbation driven by the ponderomotive force of the parent wave. Later, Del Zanna et al. (2001) suggested that Alfvén waves play a crucial role in the heating and acceleration processes in the corona. Their work demonstrated that Alfvén parametric decay could facilitate the transfer of energy from large, high-frequency Alfvén waves to smaller scales, contributing to the dissipation of energy and the heating of the solar wind.

Turbulence plays a crucial role in heating the solar corona and accelerating the solar wind. It enables energy injected at large scales through processes such as convection, magnetic reconnection, or large-scale flows to cascade down to smaller scales, where it can be dissipated as heat or transferred to non-thermal particle populations. Energy injected at large scales (the driving range) is transferred to intermediate scales, known as the *inertial range*, where the cascade process occurs. Eventually, energy reaches small enough scales, known as the dissipation range, where kinetic processes (e.g., wave-particle interactions, reconnection, or viscous and resistive effects) convert turbulent energy into heat or accelerate particles. This process is anisotropic (e.g. Goldreich and Sridhar 1995), with energy cascading more efficiently across the magnetic field lines than along them. They also introduced the concept of critical balance, according to which the characteristic time of nonlinear interaction time between counterpropagating Alfvén wave packets is comparable to the Alfvén wave propagation time along the magnetic field at all scales of the turbulence. The role of compressible fluctuations in the turbulence cascade was addressed by Bian et al. (2010), who showed that plasma heating and electron acceleration could be a result of Landau resonance with fluctuating parallel electric fields produced by Alfvénic turbulence. These findings suggest that initially linear, large-scale Alfvén waves can interact nonlinearly with each other or with compressive perturbations in plasma, leading to an energy cascade from large scales to progressively smaller scales, where turbulent energy is dissipated.

1.4.2 Velocity fluctuations and Alfvén wave cascade

Velocity fluctuations (non-thermal velocities of emitting ions) along of line of sight are often interpreted as manifestations of velocities perpendicular to magnetic field (e.g., Doyle et al. 1998) and (as we have seen above) cause frequency broadening of radio signals. Such motions are commonly interpreted as Alfvén waves (e.g., Holl-

weg 1978; Leer et al. 1982; Goldstein et al. 1995; Tu and Marsch 1995), which can undergo turbulent cascade to smaller scales. The power per unit mass (erg g^{-1} s⁻¹) available to be deposited through such a Kolmogorov cascade in strong MHD turbulence (Goldreich and Sridhar 1995) is estimated to be

$$\epsilon_{\ell_{\perp}} \simeq \frac{v_{\perp}^2}{\tau} \simeq \frac{v_{\perp}^3}{\ell_{\perp}} \ ,$$
 (1.4)

where the characteristic cascade time is $\tau = \ell_{\perp}/v_{\perp}$, with ℓ_{\perp} being a measure of the transverse correlation length at outer scales (Hollweg 1986). Although ℓ_{\perp} is not measurable directly in the corona, one can assume it to be comparable to the transverse size of a flux tube (Hollweg 1986, from considerations on the mean flux tube spacing):

$$\ell_{\perp} = \frac{7.5 \times 10^8}{\sqrt{B}} \text{ cm} , \qquad (1.5)$$

where B is in Gauss. This is also similar to the estimate used in MHD simulations (Cranmer and van Ballegooijen 2005).

1.4.3 Damping of ion-sound waves

On much smaller scales, energy could be supplied to the corona and solar wind via absorption of the energy contained in ion-sound or slow magneto-sonic waves (e.g., Kellogg 2020), that are often observed in the corona (e.g., DeForest and Gurman 1998; Wang et al. 2009; Gupta et al. 2012) and solar wind close to the Sun (Zank et al. 2024). For $q \lambda_{De} \ll 1$ (where λ_{De} is the Debye length), the spectral energy density of parallel propagating ion-sound waves W_q (erg cm⁻³ [cm⁻¹]⁻³) is related to the spectrum of density fluctuations S(q) ([cm⁻¹]⁻³]) by (Lyubchyk et al. 2017)

$$\frac{W_q^s}{n_e k_B T_e} \simeq \frac{\left|\delta n_e\right|_q^2 (q)}{n_e^2} \equiv S(q) , \qquad (1.6)$$

where k_B is Boltzmann's constant, q is the wavenumber of density fluctuations and T_e is the electron temperature. In Maxwellian plasmas, parallel propagating ion-sound waves are strongly damped, especially in a plasma with $T_i \simeq T_e$. Assuming a Maxwellian velocity distribution, the Landau damping rate γ_q^s (s⁻¹) of ion-sound waves with $v_s \simeq 2\sqrt{k_BT_e/m_i}$ is proportional to the wave frequency $\Omega_q^s = v_s \, q_\parallel$ (e.g., Krall and Trivelpiece 1973; Pécseli 2012):

$$\gamma_q^s = \sqrt{\frac{\pi}{8}} \,\Omega_q^s \left\{ \sqrt{\frac{m_e}{m_i}} + \left(\frac{T_e}{T_i}\right)^{3/2} \exp\left[-\left(\frac{T_e}{2T_i}\right)\right] \right\} , \qquad (1.7)$$

where T_i is the ion temperature and q_{\parallel} is the wavenumber of density fluctuations along the magnetic field. The first term on the right-hand-side of Equation (1.7) is the electron contribution, while the second term is from protons. For $T_e \simeq T_i$ ionsound waves are subject to very strong damping, with a damping rate becoming

$$\gamma_q^s \simeq \sqrt{\frac{\pi}{8 e}} \, v_s \, q_{\parallel} \simeq 0.4 \, v_s \, q_{\parallel} \tag{1.8}$$

that is a substantial fraction of the wave frequency. This strong damping of the energy associated with ion-sound waves results in a volumetric energy deposition rate (erg cm $^{-3}$ s $^{-1}$)

$$\frac{dE}{dt} = \int 2\,\gamma_q^s W_q^s \,d^3q \ , \tag{1.9}$$

or, equivalently, a coronal heating rate per unit mass (erg $g^{-1} s^{-1}$)

$$\epsilon_i = \frac{1}{\rho} \frac{dE}{dt} = \frac{2}{m_i n} \int \gamma_q^s W_q^s d^3 q \simeq 0.8 v_s^3 \int |q_{\parallel}| S(\mathbf{q}) \frac{d^3 q}{(2\pi)^3} = 0.8 \,\alpha \, v_s^3 \, \overline{q \, \epsilon^2} \,\,,$$
 (1.10)

where $\overline{q\,\epsilon^2}=\int qS(q)\frac{d^3q}{(2\pi)^3}$ is the spectrum-weighted mean wavenumber (as defined in Kontar et al. (2023)) and the third equality follows from the fact that the ion-sound waves propagate along the (radial) magnetic field.

1.5 Plasma Emission Mechanisms

A large part of this work revolves around radiation emitted by plasma and the mechanisms that excite it. If electrons in a distribution radiate independently from one another, contributing to the total emission in a non-constructive manner, the resulting plasma emission can is classified as 'incoherent'. An example of incoherent emission is synchrotron radiation from highly relativistic electrons in a magnetic field (Melrose 2017). If the opposite is true, plasma emission is referred to as 'coherent'. This is characterized by higher brightness temperatures than those produced by incoherent processes can produce, and is the result of particles emitting in phase with each other (Melrose 2017). A relevant example is the three wave process converting the energy of non-thermal electrons into electromagnetic waves and longitudinal electron oscillations, known as Langmuir waves. This is explored in depth in the following Subsection.

1.5.1 Stages in Plasma Emission

Electron beams can interact with the surrounding plasma, generating Langmuir waves, which in turn produce intense radio bursts known as type III solar radio bursts (Wild 1950; Fainberg and Stone 1970; Lin 1974, 1985; Holman et al. 2011; Benz 2017).

Solar flares often accelerate electron beams into the solar corona that can escape into interplanetary space following magnetic field lines. Spacecraft observations show that solar flare energetic electrons are often accompanied by type III solar radio bursts (Lin 1970; Fainberg and Stone 1970). The acceleration of an electron cloud to non-thermal velocities represents the initial stage of the plasma emission mech-

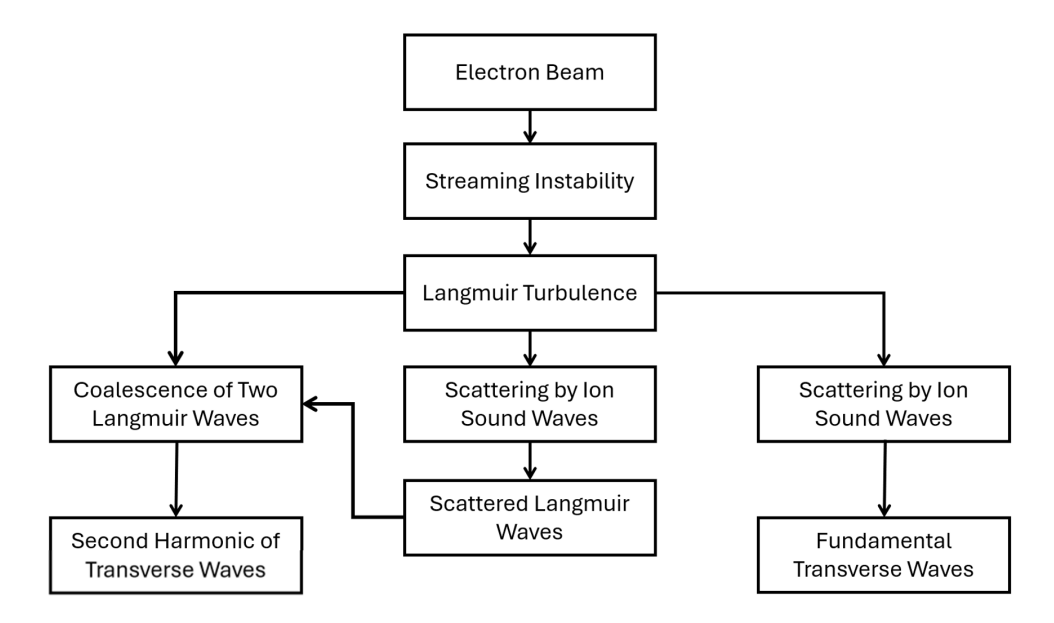


Figure 1.2: Flowchart showing the different stages of plasma emission. Figure adapted from Melrose (2017)

anism, as described in Melrose (2017), eventually leading to the generation of Langmuir waves. These are electrostatic waves (i.e. longitudinal) due to oscillations of electrons with respect to the ions in the plasma, with wavevector parallel to the magnetic field (McLean and Labrum 1985). Their dispersion relation in an unmagnetised plasma (as well as magnetised, in the case of k_{\parallel}) can be written as

$$\omega_{\rm L}^2(k) = \omega_{\rm pe}^2 + 3k_L^2 v_{\rm Te}^2 \tag{1.11}$$

where ω_L is the Langmuir wave angular frequency $v_{\rm Te}=\sqrt{k_BT_e/m_e}$ is the electron thermal velocity, k_L is the wavenumber and $\omega_{pe}=2\pi f_{pe}=\sqrt{\frac{4\pi e^2}{m_e}n_e(r)}$ is the plasma frequency. Equation 1.11 can also be rearranged as

$$k_{\rm L} = \left(\frac{m_e \left(\omega_{\rm L}^2 - \omega_{\rm pe}^2\right)}{3k_B T_e}\right)^{1/2},$$

revealing the cut-off frequency $\omega_{\rm L}=\omega_{\rm pe}$. This suggests that $\omega_L\geq\omega_{\rm pe}$, i.e. Langmuir waves are produced at (or above) the local plasma frequency. These waves can then interact with ion-sound waves (i.e. ion density fluctuations), with dispersion relation

$$\omega_S(k) = k v_S \,, \tag{1.12}$$

where where ω_S is the ion-sound wave angular frequency, k is the wavenumber, $v_s \approx \sqrt{k_B T_e/m_i} \approx v_{\rm Te}/43$ is the ion sound speed, as well as transverse EM waves, with dispersion relation

$$\omega_{\rm T}^2(k) = \omega_{\rm pe}^2 + k^2 c^2 ,$$
 (1.13)

where ω_T is the EM wave angular frequency and k_T is the wavenumber. leading to EM emission. Energy and momentum conservation throughout the three wave interaction lead to the conditions

$$\omega_1 + \omega_2 = \omega_3$$

$$\mathbf{k}_1 + \mathbf{k}_2 = \mathbf{k}_3,$$
(1.14)

where the numbers 1 and 2 refer to the input waves, while index 3 refers to the output wave. These indices can be assigned to Langmuir waves (L), EM waves (T) and ion sound waves (S), to summarize the main three-wave processes responsible for type III radio emission at fundamental and harmonic frequencies.

$$L + S \to L' \tag{1.15a}$$

$$L + S \to T \tag{1.15b}$$

$$L \to T + S \tag{1.15c}$$

$$T + S \to T \tag{1.15d}$$

$$L + L' \rightarrow T$$
, (1.15e)

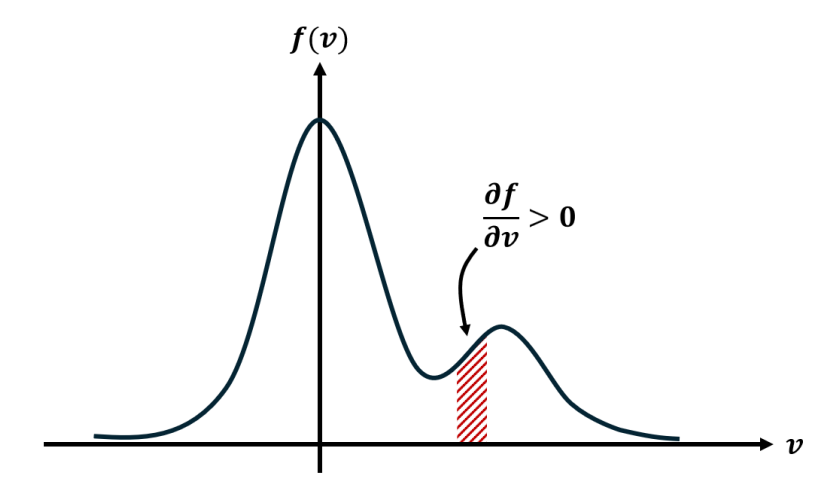


Figure 1.3: One-dimensional representation of a bump-in-tail electron distribution function. Electrons with sufficiently high energies can form a "bump" on the high-velocity end of the distribution, referred to as an electron beam. The positive slope in the beam distribution leads to instability and the production of Langmuir waves.

where, L and L' denote Langmuir waves and back-scattered Langmuir waves, respectively, while S is an ion-sound wave, and T is a transverse EM wave. The processes responsible for fundamental emission (at frequency $f_T \approx f_{\rm pe}$) are summarized by Equation (1.15b) and Equation (1.15c), while the process outlined in Equation (1.15a) produces back-scattered Langmuir waves, which, in turn, can coalesce with other Langmuir waves and give origin to emission at the second harmonic $(f_T \approx 2 \, f_{\rm pe})$.

1.5.2 Bump-in-Tail Instability

As the solar flare electrons propagate along open magnetic field lines, if the non-thermal component of the electron velocity distribution is sufficiently faster than the Maxwellian component (moving at thermal velocity $v_{\rm Te}$), an unstable positive gradient region $(\partial f/\partial v>0)$ forms in the electron velocity distribution function f(v). This is commonly known as a *beam* distribution (Aschwanden 2004). Electrons satisfying

the resonance condition $\omega_L \approx k_L v$, where v is the speed of the electron beam and ω_L and k_L are the Langmuir wave frequency and wavenumber, can trigger a bump-intail instability, interacting resonantly with the Langmuir waves, with slightly faster electrons losing energy to the wave and leading to Langmuir wave generation. As the beam loses energy to the plasma, a plateau is formed in the electron distribution function (Vedenov et al. 1961) over characteristic relaxation time $\tau_{\rm q} \approx n_e/(n_b\omega_{pe})$, where n_b and n_e are the electron densities of beam and plasma, respectively. The gas-dynamic theory describing this phenomenon was proposed by Mel'nik (1995), with the electrons moving through plasma and forming a beam-plasma structure of fast electrons and Langmuir waves. Extensive work has been done on modeling the beam-plasma interaction, both following analytical and numerical approaches. In particular, the rate of the relaxation process at different points in space is discussed in more detail in Chapter 2, and has deep implications on beam propagation. Simulations of electron beam propagation in a plasma with variations in density indicate that the distribution of Langmuir waves is shaped by plasma density fluctuations (Kontar 2001b), leading to diminished Langmuir wave growth in regions of increased density, and the appearance of fine structures in resulting plasma emissions (Section 1.7.1).

1.5.3 Sturrock's dilemma

As originally noted by Sturrock (1964), fast quasilinear relaxation produces fast beam deceleration over distances significantly shorter than those across which Type III radio bursts are observed (Kaplan and Tsytovich 1973; Muschietti 1990; Karlicky 1997; Yoon et al. 2012; Timofeev et al. 2015; Akbari et al. 2021; Krafft and Savoini 2023). This inconsistency between theory and observation has become known as Sturrock's dilemma. Many mechanisms have been proposed to resolve this dilemma. Papadopoulos et al. (1974), Bardwell and Goldman (1976) and Sauer et al. (2019) attrib-

uted its solution to nonlinear effects introduced by the oscillating two-stream instability. This instability transfers Langmuir wave energy to higher wavenumbers, where the waves no longer interact resonantly with the electron beam, limiting further wave growth. Another approach attributes beam stabilization to plasma density inhomogeneities, e.g. Goldman and Dubois (1982) and Muschietti et al. (1985) showed that spatial variations in the background plasma density can disrupt the coherent buildup of Langmuir waves, thereby inhibiting quasilinear relaxation. A third explanation, suggested by Che et al. (2017), involves a process called cyclic Langmuir collapse, first described by Zakharov (1972). This causes Langmuir waves to break into localized, high-intensity wave packets, periodically regenerating the beam-plasma system, and allowing the beam to propagate over larger distances than predicted from classical quasilinear theory alone. One more interpretation highlights that an electron cloud is spatially nonuniform, with Langmuir waves being preferentially generated at the front of the cloud and absorbed at the back, allowing the beam to propagate further (e.g. Zheleznyakov and Zaitsev 1970; Zaitsev et al. 1972; Mel'nik 1995; Mel'nik and Kontar 2000). Numerical solutions of kinetic equations (Takakura and Shibahashi 1976; Magelssen and Smith 1977; Grognard 1982; Takakura 1982; Kontar 2001b; Hannah et al. 2009; Li et al. 2008; Reid and Kontar 2013; Ratcliffe et al. 2014) broadly support the latter option, showing that even though quasilinear relaxation flattens the electron distribution, a spatially inhomogeneous electron cloud allows electrons to cover large distances. The spatially inhomogeneous cloud picture is well supported and widely used in modern kinetic simulations and is well supported, but observations and theory indicate a joint contribution from multiple effects.

1.6 Solar Radio Bursts

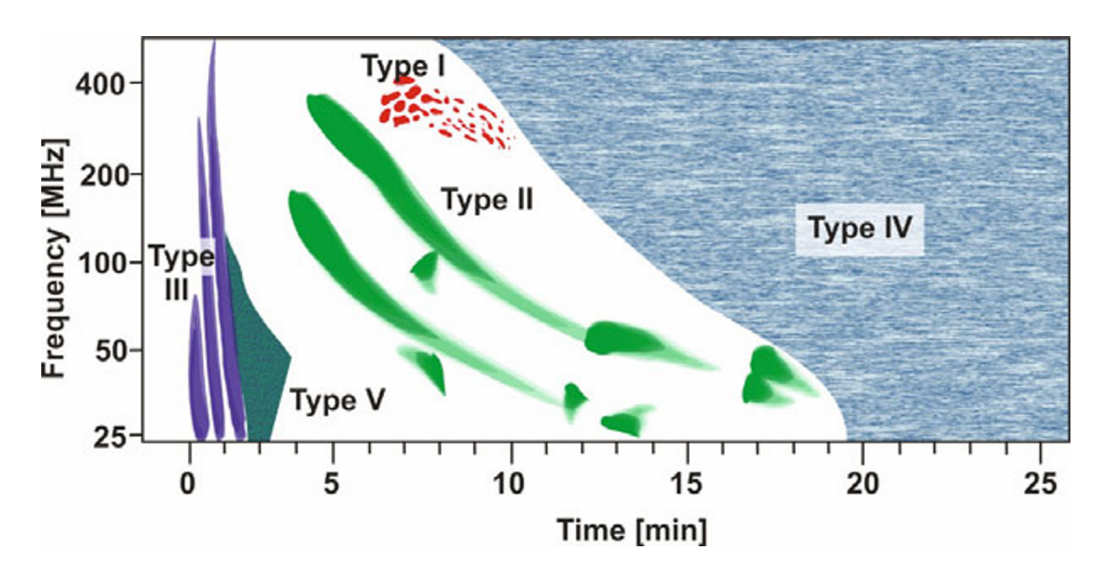


Figure 1.4: Artistic representation showing the five types of solar radio burst dynamic spectra. Image taken from Dąbrowski et al. (2016) and reproduced under CC BY 4.0.

Plasma emission results in the appearance of a variety of structures in the dynamic spectra. Among these are radio bursts, intense emissions of radio waves from the Sun. These can be classified into five types based on their spectral characteristics and physical origins.

Type I bursts, also referred to as 'noise storms', can last from a few hours up to several days and consist of many short lived, meter-decameter wavelength, narrowband emissions superimposed to a slowly varying continuum (Wild and McCready 1950; McLean and Labrum 1985).

Type II bursts can last several minutes and are characterised by a slow frequency drift ($\sim 0.1-1\,\mathrm{MHz\,s^{-1}}$). They are associated with shock waves driven by fast CMEs propagating through the corona, with exciter speeds of the order of $10^3\,\mathrm{km\,s^{-1}}$. Type II bursts often present two sub-bands, one at the local plasma frequency f_{pe} and the other at its harmonic (2 f_{pe}), which can also split into thinner lanes (possibly)

due to multiple disturbances propagating through the corona or a single disturbance interacting with coronal structures. In some instances, a Herringbone structure of rapidly drifting bursts, with both positive or negative drift rates, sprouts from the sub-bands (Wild and McCready 1950; McLean and Labrum 1985).

Type IV bursts are broadband emissions lasting from ~30 min to a few hours. They can be divided between stationary type IV and moving type IV (Takakura and Kai 1961; Kundu and Spencer 1963), depending on whether they show a non-zero drift in frequency. These bursts are generally believed to be associated to gyrosynchrotron processes from energetic electrons trapped in post-flare loops (Takakura 1961; Kundu and Spencer 1963; Dulk and Altschuler 1971; Schmahl 1972).

1.7 Type III

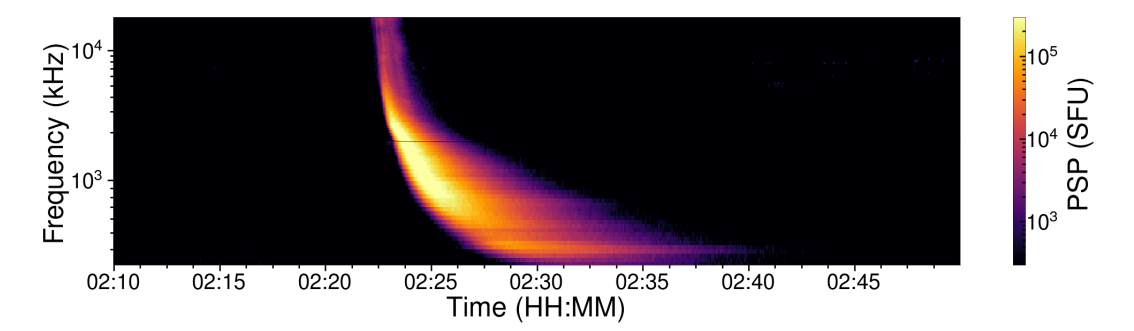


Figure 1.5: Dynamic spectra of the 07 July 2020 02:30 UT type III radio burst observed by PSP (see Section 1.8.4).

Possibly one of the most studied forms of radio emission in astrophysics, Type III radio bursts are characterised by high frequency drift rates, originating at high frequencies and drifting toward lower frequencies over time. Their duration, frequency range, and drift rate can vary from one burst to another, while their size and intensity also change depending on the observed frequency. The first to describe type III

burst properties was Wild (1950), proposing high velocity electrons (0.3c) as the exciters to account for the high frequency drift rates. A statistical survey by Alvarez and Haddock (1973a) found a frequency drift rate of

$$\frac{\mathrm{d}f}{\mathrm{d}t} = -0.01 f^{-1.84} \mathrm{MHz} \, \mathrm{s}^{-1}$$

from 75 kHz to 550 MHz, while Aschwanden et al. (1995) derive a relation of |df/dt| = $0.1 f^{1.4} \mathrm{MHzs^{-1}}$ between $200 - 3000 \mathrm{MHz}$. Extensive work has been made on observationally estimating the velocity of type III burst exciters. Using two electron density models, one obtained from radio observations and one obtained from the minimum distance from the Sun permitted by the measured arrival direction of the radio signal, Fainberg et al. (1972) find the exciter to decelerate by a factor of about 2 over distances from $10R_{\odot}$ out to 1 au. Interestingly, Dulk et al. (1987) have studied 28 type III burst events in the 30-1980 kHz range, associated with detections of Langmuir waves and fast electrons. They determine the onset and peak times for each frequency and derive the speeds of electrons exciting type III bursts finding no significant difference between exciting electron speeds near and far from the Sun in 12 of the bursts they studied (43% of events), concluding that there is no strong case in favor of exciter deceleration. Poquérusse et al. (1996) find that the beam energy, inferred by type III burst radio flux observations, decreases by a factor of ≈ 3 from the corona to the interplanetary medium (0.03 au) and then remains about constant afterwards. More recently, Krupar et al. (2015) performed a statistical survey over 29 simple and isolated IP type III bursts observed by the STEREO spacecraft over the 0.1-1 MHz frequency range and found that median values of the exciter speeds decrease from 0.09c to 0.04c and from 0.16c to 0.09c, with a median deceleration of -7 km $\rm s^{-2}$ and -12 km $\rm s^{-2}$, for density distributions corresponding to the fundamental (F) and harmonic (H) component, respectively.

Observations suggest that type III burst flux also varies with frequency, peaking around 1-2 MHz (Weber 1978; Krupar et al. 2014; Sasikumar Raja et al. 2022), and, while Sasikumar Raja et al. (2022) suggested that this may be related to the solar wind becoming super-Alfvénic near 1 MHz. In this regime, plasma flows can dominate over magnetic processes, which may affect wave-particle interactions or the escape conditions for radio emission. However, a clear explanation for this phenomenon has yet to be established.

Type III burst durations are observed to be inversely proportional to frequency, with a full-width at half-maximum (FWHM) ranging from a few seconds up to around 10 seconds at 30 MHz (Reid and Kontar 2018). A statistical analysis performed by Kontar et al. (2019) on multiple previously well recorded bursts, found their decay time (τ) to follow the power-law dependence

$$\tau(f) = (72.23 \pm 0.05) f^{-0.97 \pm 0.03} \,\mathrm{s} \,,$$
 (1.16)

where f is in MHz, over the 0.1-300 MHz range. Similarly, the apparent source size (S) of Type III bursts, obtained either via Gaussian fits to NRH/LOFAR images or via spacecraft goniopolarimetry (see Section 1.8.1), follows

$$S(f) = (11.78 \pm 0.06) f^{-0.98 \pm 0.05}$$
 degrees (1.17)

over the 0.5-500 MHz range (Kontar et al. 2019). Type III bursts can also be observed in two additional flavors, known as Type U and J bursts. They are the result of electron beams traveling along coronal loops, propagating through both ascending and descending regions of local plasma density, and their name refers to their shapes

in the dynamic spectra (e.g. Leblanc and Hoyos (1985); Kontar et al. (2017)). Such bursts are, however, less commonly observed due to the combined effect of the positive density gradient, hindering Langmuir wave generation, and higher densities (increased damping from collisions) (Reid et al. 2014).

1.7.1 Fine structures

Type IIIb

As discussed in Section 1.5.2, plasma inhomogeneities can locally inhibit Langmuir wave growth, determining the morphology of fine structures in type III bursts by modulating the associated radio emission. This is supported by simulations of electron beam propagation in an inhomogeneous plasma, e.g. Kontar (2001b) show that the distribution of Langmuir waves excited by the beam is fully determined by plasma density fluctuations, with Langmuir wave growth being suppressed in regions of higher plasma density.

This mechanism is responsible for the formation of narrowband structures (a few tens to 100 kHz (de La Noe and Boischot 1972; de La Noe 1975; Melnik et al. 2010; Sharykin et al. 2018)) within the smoothly drifting type III radio burst, commonly referred to as 'striae'. These fine spectral structures show stationary or quasi-stationary frequencies and have been observed over a wide frequency range, from as low as 20 MHz (Baselian et al. 1974; Melnik et al. 2010; Kontar et al. 2017) up to nearly 200 MHz

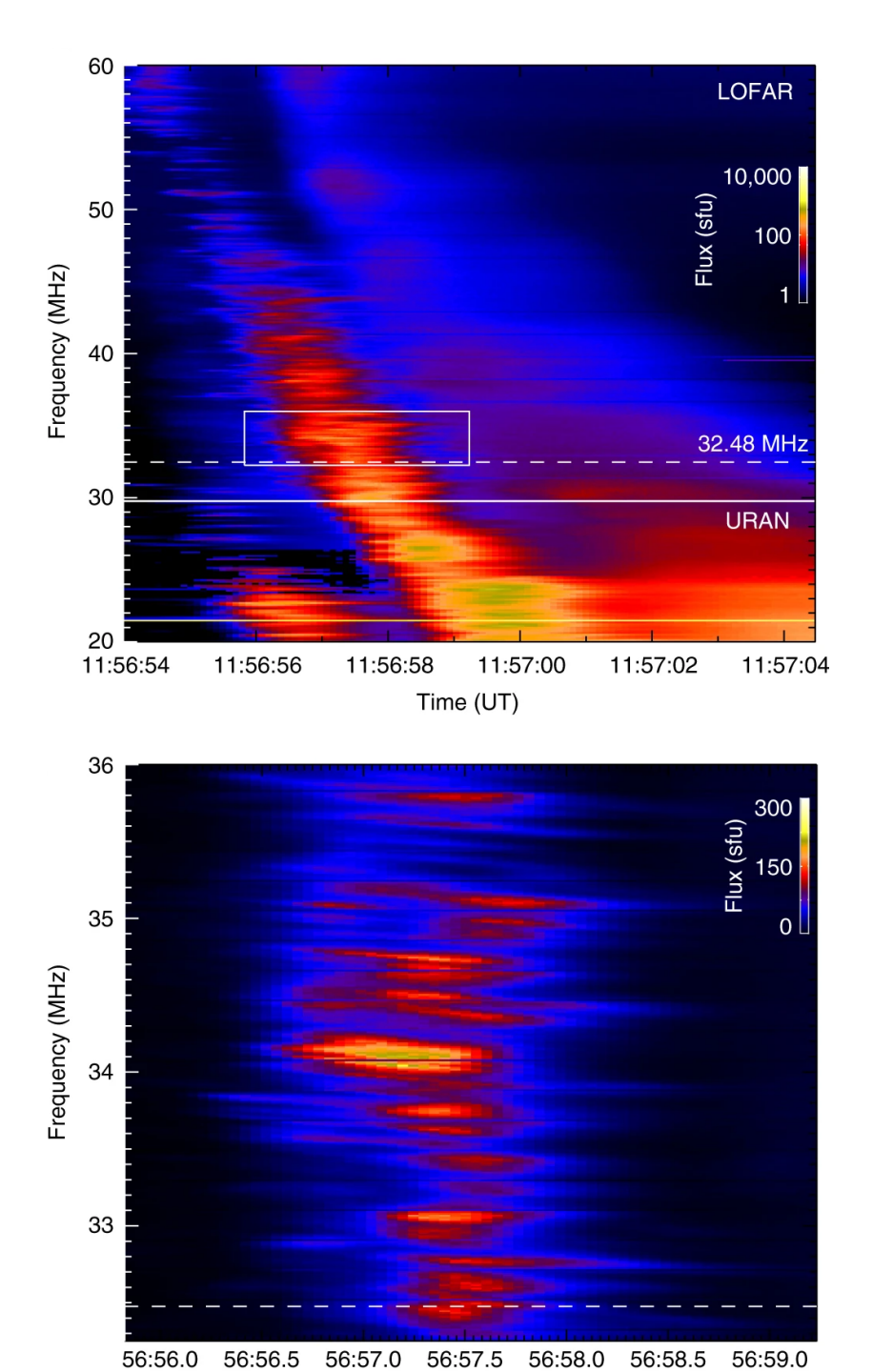


Figure 1.6: Dynamic spectrum of a type IIIb burst on the 16 April 2015 captured by both the LOw Frequency ARray (LOFAR, van Haarlem et al. (2013)) and the Ukrainian Radio interferometer of National Academy of Sciences (URAN-2, Konovalenko et al. (2016)). A 3 s expanded view between 32-36 MHz is shown at the bottom. Image taken from Kontar et al. (2017) and reproduced under CC BY 4.0.

Time (UT)

(Stewart 1975). Type III bursts with these visible fine structures are referred to as type IIIb bursts (de La Noe and Boischot 1972). Figure 1.6 shows a well-documented instance of type IIIb burst, detected by LOFAR in the 30-70 MHz range, analysed and shown in Kontar et al. (2017).

Drift-Pairs

Type III bursts are sometimes observed to be followed by an echo approximately 12 seconds after the initial structure. Both structures propagate in the same direction and have similar bandwidths, durations and sizes (typically 100-300 arcmin²) (Suzuki and Gary 1979; McLean and Melrose 1985; Kuznetsov and Kontar 2019). Together, they are known as drift pairs (Roberts 1958), and occur in the 10-100 MHz range (e.g. Ellis (1969), Melnik et al. (2005) and Kuznetsov and Kontar (2019)), typically covering a few MHz in bandwidth. Originally, their appearance was attributed to either the presence of multiple sources, or to emission from a single source reflecting off higher density plasma lower in the corona. Roberts (1958) later observed the sources to be co-spatial, favoring the latter explanation. This interpretation was contrasted by Riddle (1974), noting that the reflected component would present different spectral characteristics due to the longer time of propagation and exposure to scattering. A breakthrough was brought on by the advent of radio-wave scattering simulations showing that, accounting for anisotropic turbulence (Section 1.7.3), the focusing effect that anisotropic scattering has on radiation can provide near exact echoes after reflection, explaining the observed motion, size, source speed, and echo delay of drift pair bursts (Kuznetsov et al. 2020).

1.7.2 Type V

Type V bursts, which are relatively short-lived ($\approx 10 \text{ s}$ to a few minutes), usually appear as continuum emission following Type III bursts and are believed to be their byproduct (McLean and Labrum 1985; Aschwanden 2004), possibly due to electrons oscillating in a magnetic trap (Weiss and Stewart 1965; Zheleznyakov and Zaitsev 1968).

1.7.3 Anisotropic Density Turbulence

The combined effect of radiation scattering off both large-scale and small-scale density inhomogeneities can significantly impact the aforementioned source characteristics, leading to broadened time profiles and source sizes, while observed source location can appear shifted away from the true emission site. In an unmagnetized plasma, the scattering mean free path is proportional to $(\omega^2 - \omega_{ne}^2)^2$. Evidently, radio waves closer to the ambient electron plasma frequency are subjected to stronger scattering effects, which then decrease as the radiation moves away from the emission site. Extrasolar sources (including spacecraft), typically observed at frequencies ω significantly higher than the plasma frequency ω_{pe} of the solar medium, experience a scattering mean free path that is much larger than the distance traveled by the radio waves in the turbulent plasma. As a result, they are subject to much weaker scattering than solar radio burst emission. Nevertheless, several studies have dealt with angular broadening of extra-solar sources; e.g. Machin and Smith (1952) showed that the radiation from an extra-solar source might be cut off by refraction in the solar corona, even when the Sun-source angular separation is several times the angular radius of the visible disk. From considerations on the decreasing amplitude and elongated appearance of the Crab nebula, Hewish (1958) and Blesing and

Dennison (1972) deduced that the source behavior was consistent with a scattering process increasing the the source diameter. Moreover, they argued that scattering was more pronounced in a direction parallel to the solar axis. Anantharamaiah et al. (1994) present angular radio observations using the Very Large Array (VLA), finding the angular size of the major source axis to decrease as $\propto r^{-1.6}$. All their images show anisotropy, with a minor/major axis ratio ranging between 2 and 16, which, in turn, implies anisotropy of the scattering inhomogeneities, stretched along the magnetic field lines. From broadening observations of the Crab nebula, Dennison and Blesing (1972) and Armstrong et al. (1990) find axial ratios ranging between 0.2-0.5 and 0.1-0.4, respectively. The properties of solar and extrasolar sources are affected by the same density turbulence, with recent studies showing that the propagation of solar and extrasolar radio emission in both strong and weak scattering regimes can be modeled using the same kinetic approach (Kontar et al. 2023). Under the assumption of isotropic scattering by small-scale density fluctuations, many more or less recent ray-tracing simulations have been conducted in an attempt to explain observed type III source characteristics, (e.g., Steinberg et al. (1971); Thejappa et al. (2007); Krupar et al. (2018)). However, none of these models were able to fully account for all observations, with some studies resorting to the presence of large-scale structures as a possible explanation. A major breakthrough was achieved by Kontar et al. (2017), from quantitative considerations on the observed time and frequency characteristics of solar radio burst fine structures. With a temporal FWHM $\Delta t \simeq 1.1\,\mathrm{s}$ at ~ 35 MHz, the fine structures limited the apparent source size along the line of sight to about $\Delta tc \simeq 8 \, \mathrm{arcmin}$. The larger source size perpendicular to the line of sight (20 arcmin on the plane of the sky) serves as strong evidence in favor of anisotropic scattering, with a dominant component perpendicular to the radial direction. This idea was further explored by Kontar et al. (2019), including anisotropy in radio wave scattering simulations. In their model, density fluctuations were assumed to be axially symmetric with respect to a radial magnetic field, with a spectrum of density

fluctuations S parameterized as

$$S(\mathbf{q}) = S\left(\left[q_{\perp}^2 + \alpha^{-2}q_{\parallel}^2\right]^{1/2}\right) ,$$
 (1.18)

where q is the wavevector of electron density fluctuations, and

$$\alpha = h_{\perp}/h_{\parallel} \tag{1.19}$$

is the anisotropy factor, where h_{\parallel} and h_{\perp} are the parallel and perpendicular correlation lengths, respectively. Comparison between simulation results and observed radio burst characteristics showed that an anisotropy factor of 0.3 was required to reproduce both decay times and source sizes near 30 MHz, outperforming the isotropic case. In particular, higher anisotropy factors were shown to have a focusing effect on radiation, shortening observed decay times. Observed source positions were also affected, with sources injected at $1.75R_{\odot}$ appearing shifted by $0.6R_{\odot}$ from the emission site. This effect is strongly dependent on the source-observer angle, with sources propagating along the LOS showing no displacement. Simulations by Chen et al. (2020) successfully replicated the positional and dimensional properties of striae, as previously observed by Kontar et al. (2017), for both fundamental and harmonic emission components. Using the same simulation employed by Kontar et al. (2019), Kuznetsov et al. (2020) show that the source size diminishes for anisotropy parameter $\alpha \leq 0.2$. The study also finds that pronounced anisotropy leads to brief temporal profiles accompanied by a discernible radio echo, a characteristic feature of drift-pair bursts. A longstanding problem in the interpretation of fundamentalharmonic burst pairs is that the frequency ratio is often to be below the expected value of 2, with some observations reporting ratios as low as 1.6. Chen et al. (2023) offer a solution by demonstrating that anisotropic scattering can lead to a time delay in the fundamental component relative to the harmonic, showing that a scattering anisotropy of approximately $\alpha \sim 0.25$ reproduces the observed frequency ratios.

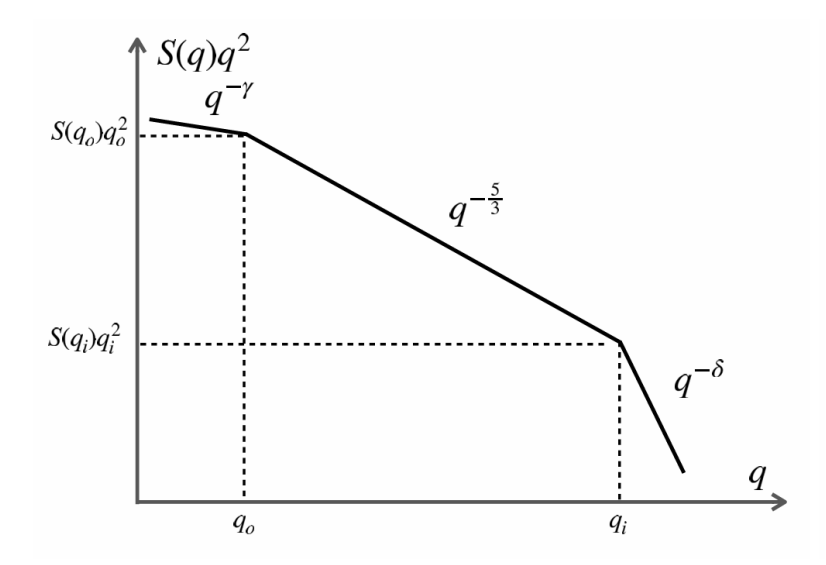


Figure 1.7: q-space spectrum $q^2S(q)$ from Kontar et al. (2023): flat at energy-containing scales; $q^{-5/3}$ in the inertial range between the outer scale $\ell_o = 2\pi/q_o$ and the inner scale $\ell_i = 2\pi/q_i$; and $q^{-\delta}$ ($\delta > 2$) in the dissipation range. Image taken from Kontar et al. (2023) and reproduced under CC BY 4.0.

1.7.4 Inner and Outer Scales

Solar wind density fluctuations are observed to follow a Kolmogorov-like power spectra scaling, with $P(f) \propto f^{-5/3}$ within the inertial range, between the outer and inner scales (Alexandrova et al. 2013). This behavior suggests an energy cascade from large-scales, down to smaller scales. At smaller scales, the inner scale $l_i = 2\pi/q_i$ marks the spatial scale where the slope transitions from 5/3 to around 2.5. According to Coles and Harmon (1989), this inner scale varies with solar distance as $l_i(r) \approx r/R_{\odot}$ [km] within the range of 2-70 R_{\odot} . Alexandrova et al. (2012), Ingale et al. (2015) and Tasnim et al. (2022) express the inner scale in terms of the electron gyro-radius, with l_i given by $l_i = \frac{2.38}{B\sqrt{T_e}}$ cm, where T_e is the electron temperature in eV. Below the inner scale, at the ion gyroscale, fluctuations are generally believed to dissipate (Šafránková et al. 2015). The outer scale, defined as $l_o = 2\pi/q_o$, corresponds to the spatial scale where the spectral slope transitions from approximately 1 to 5/3, with q_o denoting the relative wavenumber of the density fluctuations. Supported by space-

craft measurements, Wohlmuth et al. (2001) reported the outer scale to vary with heliocentric distance r as $l_o(r) = (0.23 \pm 0.11) r^{0.82 \pm 0.13}$, where r is expressed in solar radii. Later works by Bruno and Carbone (2013) show a dependence of the break frequency $f_b \sim (r/R_\odot)^{-1.5}$ in the ecliptic solar wind power spectrum. This is in contrast to the $f_b \sim (r/R_\odot)^{-1.1}$ dependence found by Horbury et al. (1996) in the polar region, indicating slower turbulence evolution in the polar wind than in the ecliptic.

1.8 Instrument Overview

1.8.1 Goniopolarimetric Techniques

Before delving into a description of the instruments used in this investigation, it is important to first present some basic principles of antenna theory and the methods used for determining the locations of radio sources. A conventional radio telescope has angular resolution λ/D , where λ is the observed wavelength and D represents the telescope aperture (Cecconi et al. 2008; Cecconi 2014). This equation implies that achieving a resolution of $\lambda/D \ll 1$ would require a $\sim 1-10^4$ km aperture size, which is rather challenging to equip onto a spacecraft. Many space missions solve this dilemma by employing simple electric dipole antennae, with lengths ranging from a few to several tens of meters (Cecconi et al. 2008; Cecconi 2014). This does lead to inherently low angular resolution, an issue overcome through the use of goniopolarimetric (GP) techniques (or direction-finding techniques in the literature) developed to retrieve flux, polarization state, and direction of arrival of the signals detected. Instrument calibration requires determining the antenna's beaming pattern, a process often carried out by observing known radio sources, sometimes aided by other calibrated spacecraft observing the same event. For instance, Vecchio

et al. (2021) compare simultaneous Solar Orbiter and Wind detections, using the intense radio emission from a type III burst as a reference to cross-calibrate the Radio and Plasma Waves (RPW) antenna system on the Solar Orbiter spacecraft. Currents on the antenna are determined by the length and shape of the antenna, as well as the detected wavelength, with short, straight antennas $(L/\lambda < 1/10)$ radiating almost homogeneously in all directions perpendicular to the antenna's axis (Cecconi et al. 2008; Cecconi 2014). The voltage difference can be measured either between the antenna and the body of the spacecraft or between the two poles of the antenna, leading to the distinction between monopole and dipole antennas, respectively. The measured differential voltages are then converted into physical parameters by a 'receiver'. Receivers can be either single-channel, only measuring the power received by the connected antenna, or multi-channel, capable of simultaneously measuring the signal recorded by multiple antennas. To provide apparent source positions of the incoming emission, GP receivers compute the correlation values between voltages measured on the antennas, estimating the direction of the local wave-vector. This technique can be carried out both on a spinning spacecraft (spin demodulation GP) or on a three-axis stabilized spacecraft (instantaneous GP). The first method requires wave-parameters to be fixed over the spacecraft spin period (Cecconi et al. 2008; Cecconi 2014), while the second method requires several antennas and multi-channel receivers to obtain instantaneous measurements (Cecconi et al. 2008).

If the same event is observed simultaneously by multiple spacecraft, another option is to analyze the peak flux observed at each viewing location to extrapolate the direction of maximum directivity, i.e. the direction of propagation of the radio source. Recently, this method was used by Musset et al. (2021), Chen et al. (2023) and Clarkson et al. (2025) to determine the Heliocentric Earth Ecliptic (HEE) longitude (Thompson 2006) of radio burst sources by analyzing the peak flux observed at each viewing location of the PSP (Section 1.8.4), STEREO-A (Section 1.8.3), Solar Orbiter (SolO) (Section 1.8.2), and Wind (Section 1.8.5) spacecraft. The recorded type III

solar radio burst flux, proportional to r^{-2} was scaled to 1 AU. The direction of maximum directivity was found by assuming that the directivity follows an exponential shape

$$I_{\text{s/c}} = I_0 \exp\left(\frac{\cos\left(\theta_{\text{s/c}} - \theta_0\right) - 1}{\Delta\mu}\right), \tag{1.20}$$

where $\theta_{\rm s/c}$ and θ_0 are the angles of the spacecraft and the type III source, $I_{\rm s/c}$ is the peak flux measured by the spacecraft, and $\Delta\mu$ is the parameter controlling the shape of the radio emission directivity pattern, which depends on the anisotropy factor α .

1.8.2 SolO and RPW

The Solar Orbiter (SolO) mission is a collaboration between the European Space Agency (ESA) and NASA. Launched in February 2020, it carries 10 instruments (6 remote sensing and 4 for in situ measurements) (Müller et al. 2020).

The Radio and Plasma Waves (RPW) instrument on Solar Orbiter consists of three 6.5m antenna units deployed in the plane perpendicular to the spacecraft-Sun direction, allowing for several sensor configurations. Monopole modes (V1, V2 and V3) measure the potential difference between an antenna and the spacecraft ground, while dipole modes (V1-V2, V2-V3, V3-V1) measure the potential difference between two antennas (Maksimovic et al. 2020; Vecchio et al. 2021). A search-coil magnetometer is mounted on the spacecraft boom. RPW provides crucial in-situ measurements of density fluctuations that influence radio wave propagation (Maksimovic et al. 2020; Müller et al. 2020). Three subsystems, namely the Low Frequency Receiver (LFR), Thermal Noise and High Frequency Receiver (THR or TNR-HFR) and Time Domain Sampler (TDS), produce daily independent data.

The main data product of TDS are electric and magnetic field waveform snapshots (Maksimovic et al. 2020).

LFR comprises three frequency channels, covering frequencies between 6.5 Hz and 10 kHz (Maksimovic et al. 2020). Temporal and spectral resolution heavily depend on the mode and the antenna in use, with monopole configurations V1, V2 and V3 having resolutions $\Delta f = 8,128,768$ Hz and $\Delta t = 4,20,1$ s, respectively, and dipole configurations having $\Delta f = 4,46,384$ Hz and $\Delta t \sim$ 1-20s (Maksimovic et al. 2020).

THR measures plasma waves and radio emissions in the interplanetary medium, and includes two high-frequency receivers: the Thermal Noise Receiver (TNR) and the High Frequency Receiver (HFR). TNR detects both electric and magnetic power spectral densities over the 4 kHz to 1 MHz frequency range, while HFR provides electric power spectral densities from 375 kHz to 16 MHz (Maksimovic et al. 2020). Moreover, TNR can be setup to combine simultaneous measurements (dipoles or monopole, or both) and compute autocorrelations and cross-correlations, while HFR only acts as a sweeping receiver, providing the measured electric power spectral density for dipole antennas. TNR spectral and time resolution are $\Delta f = 4.3\% f$ and $\Delta t = 1.13 - 12$ s, while HFR spectral and time resolution amount to $\Delta f = 50$ or 100kHz and $\Delta t = 2 - 22$ s (Maksimovic et al. 2020).

1.8.3 STEREO-A and S/WAVES

The Solar Terrestrial Relations Observatory (STEREO) mission, launched by NASA to study the structure of solar storms and CMEs, consists of two nearly identical spacecraft following Earth's orbit, with STEREO-A moving ahead of Earth and STEREO-B lagging behind it, offering stereoscopic solar observations (Kaiser et al. 2008).

A major issue followed a planned STEREO-B reset in 2014, resulting in the total loss of communication with the spacecraft. Meanwhile, STEREO A remains active and still plays a fundamental role in investigating the origin and morphology of CMEs.

Aboard the STEREO spacecraft, the S/WAVES instrument utilizes three monopole antennas to measure electric field fluctuations (Bougeret et al. 2008; Bale et al. 2008). It includes two main receivers: the Low Frequency Receiver (LFR), operating between 10 kHz and 160 kHz across 32 logarithmically spaced frequency channels, and the High Frequency Receiver (HFR), covering 125 kHz to 16.025 MHz with 319 linearly spaced frequency channels. Both receivers have a time resolution of 38s (Bougeret et al. 2008).

1.8.4 PSP and PSP/FIELDS(RFS)

The Parker Solar Probe (PSP), launched by NASA in August 2018 (Bale et al. 2016; Thapa and Yan 2024), has the primary scientific objective to determine the structure and dynamics of the Suns coronal magnetic field, shed light on the mechanisms behind coronal heating, investigate how the solar wind is accelerated, how energetic particles are generated and how their distribution evolves (Fox et al. 2016).

Aboard the Parker Solar Probe (PSP), the FIELDS experiment includes V1-V5 antennas and 3 magnetic sensors. Part of this instrument is the Radio Frequency Spectrometer (RFS), covering frequencies between 10.5 kHz and 19.2 MHz. This frequency range is subdivided into the Low-Frequency Receiver (LFR), featuring 64 logarithmically spaced frequency bands from 10.5 kHz to 1.7 MHz, and the High-Frequency Receiver (HFR) covering 64 logarithmically spaced frequency bands from 1.3 to 19.2 MHz (Bale et al. 2016; Thapa and Yan 2024). The FIELDS instrument is active during

PSPs close approaches, when the spacecraft is within 0.25 AU of the Sun, collecting HFR and LFR spectra with a 7s time resolution. During the remainder of the mission, time resolution is reduced, with RFS recording one spectrum every 56s (Bale et al. 2016; Thapa and Yan 2024).

1.8.5 Wind and Wind/WAVES

The Wind spacecraft was launched by NASA in November 1994 to study the properties of the interplanetary medium as well as the disturbances within it, such as shocks and waves. It was finally placed into Lagrangian point 1 (L1) orbit in 2004, where it remains operational to this day, far outlasting its mission timeline and becoming one of the longest-running space physics missions (Wilson et al. 2021). It contributed to a vast amount of studies both on large scale solar wind structures and turbulence, and on small scales, becoming one of the first spacecraft to fully resolve Langmuir waves in time series electric field data (e.g., Kellogg et al. (1996)).

Wind is a spin stabilized spacecraft, with a spin period of ~ 3 s, meaning it can employ spin demodulation GP techniques (see Section 1.8.1 to track shocks and energetic particle streams from about 3-4 R_{\odot} from the center of the Sun to about 1 AU, allowing the determination of sizes, polarization and direction of the source centroid (Manning and Fainberg 1980; Fainberg et al. 1985). The spacecraft is equipped with the WAVES instrument, providing measurements of radio and plasma wave phenomena for electric field frequencies ranging from a few Hz to 14 MHz. WAVES comprises three electric dipole antennas: two coplanar and orthogonal in the spin plane, and the third along the spin axis. It also boasts three orthogonally mounted magnetic search coils (Bougeret et al. 1995). WAVES includes multiple components. WAVES TDS (Time Domain Sampler) covers frequencies from a few Hz to ~ 100 kHz, with

et al. 1995). WAVES FFT allows to analyse the spectrum of magnetic field fluctuations over a 0.3 Hz - 2 kHz range (Bougeret et al. 1995). The Thermal Noise Receiver (TNR) operates in a frequency range from 4 kHz to 256 kHz, covering low-frequency plasma waves and thermal noise generated by electron plasma oscillations in the solar wind (Bougeret et al. 1995). Finally, dynamic spectra of radio bursts are provided by RAD1 and RAD2 receivers, covering 20-1040 kHz and 1.075-13.825 MHz, with 4 kHz and 50 kHz spectral resolutions and time resolutions of 192s and 36s (Bougeret et al. 1995).

Chapter 2

Nonlinear Diffusion with Advection of Flare Accelerated Electrons

Introduction

This chapter is based on the work by Kontar et al. (2024), with the author of this thesis as second author. The author of this thesis' main contributions consist in part of section 2.2, section 2.3.1 and part of section 2.4.1, as well as Figures 2.4 and 2.5.

While time-consuming numerical simulations provide important insights, analytic theory is essential to relate observable properties of type III bursts and electron beam properties. One major simplification for the challenge is to utilize the smallness of quasilinear time (i.e. characteristic time of beam relaxation) in comparison to the characteristic time of beam propagation and to seek the hydrodynamic description at the timescales larger than the quasilinear relaxation (Ryutov and Sagdeev 1970; Mel'nik 1995). This is a good assumption due to the smallness of the characteristic

time of beam-plasma interaction (the quasilinear time, $\tau_{\rm q} \sim n_p/(\omega_{pe}n_b)$, where $\omega_{\rm pe}$ is the local plasma frequency, n_p is the background plasma electron number density and n_b is the number density of beam electrons) compared to the characteristic time of the beam t, $\tau_{\rm q} \ll t$. However, due to the finite size of the electron cloud, the quasilinear time being inversely proportional to the beam density should change from small (high beam density near cloud center) to large (small beam density away from the cloud center) values. Furthermore, the parameter $\tau_{\rm q}/t$ becomes a function of space and time through dependency on the beam density. This chapter addresses the theoretical challenge by noting that the quasilinear time has to be explicitly treated as a function of time and space depending on the electron number density of the electron cloud. Thus, the relaxation process is not going to be taking place at the same rate in all points of space. This non-linear description of fast diffusion naturally leads to a more realistic analytical solutions, comparable to the results of the numerical simulations shown in the literature.

2.1 Kinetic description of electrons and Langmuir waves

Quasilinear theory takes its name from the Langmuir waves driven by the beam being treated linearly, while their weakly nonlinear reaction on the electron distribution is included as an averaged resonant diffusion. It describes the propagation of electrons along magnetic field lines in a weakly magnetized plasma (electron gyromotion is neglected), and the resonant interaction of the electrons with Langmuir waves e.g. $\omega=kv$, where ω is the wave frequency ($\sim \omega_{\rm pe}$), k is the wave number and v is the velocity. For simplicity, the resonant condition is applied, denoting both the phase velocity of the wave and the electron beam velocity by v. The quasilinear equations (Vedenov and Velikhov 1963; Drummond and Pines 1964), provide a kinetic description for electrons and Langmuir waves in type III solar radio bursts.

As the electrons follow the magnetic field lines, the reduced field-aligned electron distribution function $f(v,x,t)=\int f(\mathbf{v})d\mathbf{v}_{\perp}$ and the spectral energy density of Langmuir waves $W(k,x,t)=\int W(\mathbf{k})d\mathbf{k}_{\perp}$ evolve following the non-linearly coupled kinetic equations:

$$\frac{\partial f}{\partial t} + v \frac{\partial f}{\partial x} = \frac{4\pi^2 e^2}{m^2} \frac{\partial}{\partial v} \frac{W}{v} \frac{\partial f}{\partial v} = \frac{\partial}{\partial v} D \frac{\partial f}{\partial v}, \qquad (2.1)$$

$$\frac{\partial W}{\partial t} = \frac{\pi \omega_{pe}}{n_p} v^2 W \frac{\partial f}{\partial v} \,, \tag{2.2}$$

where $\int W dk = U$ and $\int f dv = n_b$ are the energy density of Langmuir waves and the number density of the electron beam, and $D \equiv D(v, x, t)$ is the diffusion coefficient in velocity space. Similarly to Mel'nik (1995), Kontar et al. (1998), Mel'nik et al. (1999) and Kontar (2001b), the spontaneous terms are not taken into account in the kinetic model (equations 2.1,2.2), since the beam-driven level of Langmuir waves is much higher than the spontaneous/thermal one, with $W_{\rm LW}/W_{\rm th} \approx 10^7-10^8$ at 1.1 R_{\odot} (Lyubchyk et al. 2017). Moreover, Equation (2.2) does not include the spatial transfer of the energy by Langmuir waves, since the group velocity of Langmuir waves is small ($v_{gr} \ll v$, where v_{T_e} is the electron thermal velocity). The kinetic equations (2.1-2.2), in general, do not admit closed-form analytical solutions, and additional assumptions are required to solve this system of equations. Equations (2.1,2.2) are coupled to nonlinear processes responsible for decay/coalescence of Langmuir waves. The wave-wave interactions are normally treated numerically, e.g. the large-scale simulations by Ratcliffe et al. (2014), simulating electron injection in the solar corona, and the subsequent wave production which leads to radio emission. For simplicity, electron collisional Coulomb losses, as well as the collisional damping of plasma waves and the Landau damping of plasma waves by background plasma, are assumed to be negligible (see Reid and Kontar 2010, for full description).

2.2 Hydrodynamic description

The characteristic time of beam-plasma interaction is normally small $\tau_{\rm q}\ll t=d/v$, where d is the size of an electron beam. The smallness of quasilinear time allows the use of a hydrodynamic description for beam electrons and Langmuir waves (Ryutov and Sagdeev 1970; Mel'nik 1995; Mel'nik et al. 1999; Ryutov 2018), so the electron distribution function f(v,x,t) in the kinetic equations (2.1,2.2) is the series in small parameter $\tau_{\rm q}v/d$

$$f = f^0 + f^1 + \dots {2.3}$$

Substituting the expansion (2.3) into kinetic equations (2.1,2.2), in 0^{th} -order (or the fastest terms when $\tau_q v/d \to 0$):

$$0 = \frac{4\pi^2 e^2}{m^2} \frac{\partial}{\partial v} \frac{W^0}{v} \frac{\partial f^0}{\partial v} \propto \tau_q^{-1}, \tag{2.4}$$

$$0 = \frac{\pi \omega_{pe}}{n_p} v^2 W^0 \frac{\partial f^0}{\partial v} \propto \tau_{\mathbf{q}}^{-1}. \tag{2.5}$$

and hence dominant for $d/v \gg \tau_{\rm q}$. This leads to a well-known result that the $0^{\rm th}$ -order solution is a plateau in velocity space since $\partial f^0/\partial v = 0$ (e.g. Vedenov et al. 1967)

$$f^{0}(v, x, t) = \begin{cases} p(x, t), & 0 < v < u(x, t) \\ 0, & v \ge u(x, t), \end{cases}$$
 (2.6)

where $p\left(x,t\right)$ is the plateau height and u(x,t) is the maximum electron velocity, and an enhanced level of Langmuir waves, so that the spectral energy density of Langmuir waves becomes

$$W^{0}(v, x, t) = \begin{cases} W_{0}(v, x, t), & 0 < v < u(x, t) \\ 0, & v \ge u(x, t) \end{cases}$$
 (2.7)

where zero-order terms f^0 and W^0 turn the right-hand sides of kinetic equations (2.1, 2.2) to zero. In other words, any initially unstable electron distribution function relaxes to a plateau and Langmuir waves are generated within quasilinear time $\sim \tau_{\rm q}$. The number density of electrons in the beam is, assuming a plateau is formed at all times,

$$n(x,t) = \int_{0}^{u(x,t)} p(x,t) \, dv = p(x,t) \, u(x,t).$$
 (2.8)

Note that in a realistic scenario the particle number in the plateau need not be conserved, as particles from other velocities can enter and leave the plateau. Following (Mel'nik et al. 1999), one can find the equations for p(x,t), u(x,t) and $W_0(v,x,t)$. Integrating equation (2.1) over v from v=0 to v=u(x,t), one obtains the equation for electron number density n(x,t)=p(x,t)u(x,t)

$$\frac{\partial pu}{\partial t} + \frac{1}{2} \frac{\partial pu^2}{\partial x} = \frac{\partial n}{\partial t} + \frac{1}{2} \frac{\partial nu}{\partial x} = 0, \tag{2.9}$$

which is the hydrodynamic continuity equation or conservation of electrons. Integrating equation (2.1) over v between $u - \xi$ and $v = u + \xi$, with $\xi \to 0$, gives

$$\frac{\partial u}{\partial t} + u \frac{\partial u}{\partial x} = 0, \tag{2.10}$$

while combining equations (2.1,2.2) one obtains

$$\frac{\partial p}{\partial t} + v \frac{\partial p}{\partial x} = \frac{\omega_{pe}}{m} \frac{\partial}{\partial v} \frac{1}{v^3} \frac{\partial W_0}{\partial t}, \qquad (2.11)$$

which is the equation for the plateau height. Equation (2.11) can be integrated to find a solution for a initial value problem. Following Mel'nik (1995) and Mel'nik et al. (1999), the equations for p(x,t), u(x,t) and W(v,x,t) can be integrated for given initial conditions. For Maxwellian initial condition (Mel'nik et al. 2000)

$$f(v, x, t = 0) = n_b \exp(-x^2/d^2)g(v), \tag{2.12}$$

where n_b is the electron beam density at x = 0, and $g(v) = 2v/v_0^2$ for $v < v_0$, the solution of equations (2.9, 2.10,2.11) gives (see (e.g. Kontar 2001c))

$$u(x,t) = v_0, (2.13)$$

$$p(x,t) = \frac{n_b}{v_0} \exp(-(x - v_0 t/2)^2/d^2), \qquad (2.14)$$

$$W_0(v, x, t) = \frac{m}{\omega_{pe}} v^4 \left(1 - \frac{v}{v_0} \right) p(x, t), \qquad (2.15)$$

where v refers to the resonance speed. The solution (2.13-2.15) suggests a beam-Langmuir-wave structure, i.e. electron beam and Langmuir waves propagate with speed $v_0/2$ preserving the initial size d. The equations assume that the relaxation proceeds at the same rate for all x and t, which is evidently not true due to finite spatial size of the electron beam d. The electron number density is higher near the peak of the beam-plasma structure and decreases away. Therefore, the relaxation of electrons should proceed at different rate $\tau_q^{-1} \propto n(x,t)$ in various spatial locations and one should take into account the spatial variation of τ_q due to variation of electron number density n(x,t) of the beam.

2.3 Hydrodynamics with non-linear diffusion

To address the inhomogeneity of quasilinear time, the f^1 term is retained in the expansion of f and substituting (2.3) into (2.1), one finds

$$\frac{\partial (f^0 + f^1)}{\partial t} + v \frac{\partial (f^0 + f^1)}{\partial x} = \frac{\partial p}{\partial t} + v \frac{\partial p}{\partial x} + \frac{\partial f^1}{\partial t} + v \frac{\partial f^1}{\partial x} = \frac{\partial}{\partial v} D \frac{\partial f^1}{\partial v}, \qquad (2.16)$$

where the first order terms are retained. Further, integrating this equation over velocity from 0 to ∞ gives

$$\frac{\partial}{\partial t} \int_{0}^{v_0} \left(f^0 + f^1 \right) dv + \frac{\partial}{\partial x} \int_{0}^{v_0} v \left(f^0 + f^1 \right) dv = D \frac{\partial f^1}{\partial v} \bigg|_{0}^{v_0}, \qquad (2.17)$$

where due to the quasilinear relaxation at $t \gg \tau_q$, a plateau is considered to be established in the electron distribution function i.e. $f^0(v, x, t) = p(x, t)$ for $v < v_0$. Hence, equation (2.17) becomes

$$\frac{\partial p v_0}{\partial t} + \frac{1}{2} \frac{\partial p v_0^2}{\partial x} + \frac{\partial}{\partial t} \int_0^{v_0} f^1 dv + \frac{\partial}{\partial x} \int_0^{v_0} v f^1 dv = 0, \qquad (2.18)$$

where $\int_{0}^{v_0} f^1 dv = 0$ because $\int_{0}^{v_0} (f^0 + f^1) dv = n(x, t)$. Writing the electron number density as $n(x, t) = p(x, t)v_0$, equation (2.18) can be written as

$$\frac{\partial n}{\partial t} + \frac{v_0}{2} \frac{\partial n}{\partial x} + \frac{\partial}{\partial x} \int_0^{v_0} v f^1 dv = 0, \qquad (2.19)$$

where $f^1(v, x, t)$ is to be found. The procedure to find f^1 is similar to the derivation of a spatial diffusion coefficient from pitch-angle scattering diffusion coefficient (Jokipii 1966; Hasselmann and Wibberenz 1970; Schlickeiser 1989). Multiplying equation (2.16) by v_0 and subtracting equation (2.19) one finds

$$\left(v - \frac{v_0}{2}\right)\frac{\partial n}{\partial x} + v_0\frac{\partial f^1}{\partial t} + v_0v\frac{\partial f^1}{\partial x} - \frac{\partial}{\partial x}\int_0^{v_0} vf^1dV = v_0\frac{\partial}{\partial v}D\frac{\partial f^1}{\partial v},$$
(2.20)

and retaining only zero order terms, one finds equation for $f^1(v, x, t)$

$$\frac{1}{v_0} \left(v - \frac{v_0}{2} \right) \frac{\partial n}{\partial x} = \frac{\partial}{\partial v} D \frac{\partial f^1}{\partial v} , \qquad (2.21)$$

where the right-hand side is zero order due to fast plateau formation (equation 2.4). The resonant interaction is strongest for electrons with velocities close to the phase velocity of the waves, and becomes progressively less effective for electrons further from this velocity. Kontar and Pécseli (2002) show plateau formation to occur between \sim 3-4 $v_{\rm Te}$ and \sim 10-20 $v_{\rm Te}$ in a plasma with Maxwellian thermal component. In the present model, quasilinear relaxation is taken to operate between $0 < v < v_0$. Thus, velocity diffusion coefficient $D = \pi \omega_{pe}^2/(mn_p)(W/v)$ should be zero at the boundary velocities, i.e.:

$$D|_{v=0} = D|_{v=v_0} = 0. (2.22)$$

These boundary conditions allow us to integrate equation (2.21) over v and obtain

$$D\frac{\partial f^{1}}{\partial v} = \frac{1}{v_{0}} \frac{\partial n}{\partial x} \int_{0}^{v} \left(v' - \frac{v_{0}}{2}\right) dv' = \frac{1}{v_{0}} \frac{\partial n}{\partial x} \frac{1}{2} v \left(v - v_{0}\right) + C_{1}, \qquad (2.23)$$

where $C_1 = 0$ due to $D|_0 = D|_{v_0} = 0$, yielding

$$\frac{\partial f^1}{\partial v} = \frac{v(v - v_0)}{2v_0 D} \frac{\partial n}{\partial x}.$$
 (2.24)

Further, integrating equation (2.24) over v, yields an expression for f^1

$$f^{1} = \frac{1}{2v_{0}} \frac{\partial n}{\partial x} \int_{0}^{v} \frac{v^{2} - v_{0}v^{'}}{D} dv^{'} + C_{2}.$$
 (2.25)

To determine the constant of integration C_2 , note that $\int_0^{v_0} f^1 dv = 0$, i.e.

$$\int_0^{v_0} f^1 dv = 0 = \left[v f^1 \right] \Big|_0^{v_0} - \int_0^{v_0} v \frac{\partial f^1}{\partial v} dv \,,$$

yielding

$$C_2 = -\frac{1}{2v_0^2} \frac{\partial n}{\partial x} \int_0^{v_0} (v_0 - v') \frac{v'^2 - v_0 v'}{D} dv'.$$
 (2.26)

Substituting C_2 into equation (2.25), and taking into account that

$$\int_0^{v_0} v f^1 dv = 0 = \left[\frac{v^2}{2} f^1 \right]_0^{v_0} - \int_0^{v_0} \frac{v^2}{2} \frac{\partial f^1}{\partial v} dv \,,$$

one finds that

$$\int_{0}^{v_0} v f^1 dv = -\frac{1}{4v_0} \frac{\partial n}{\partial x} \int_{0}^{v_0} \frac{v^2 (v_0 - v)^2}{D} dv.$$
 (2.27)

Hence, the transport equation for electron number density (equation 2.19) takes the form

$$\frac{\partial n}{\partial t} + \frac{v_0}{2} \frac{\partial n}{\partial x} = -\frac{\partial}{\partial x} \int_0^{v_0} v f^1 dv = \frac{\partial}{\partial x} \frac{1}{4v_0} \frac{\partial n}{\partial x} \int_0^{v_0} \frac{v^2 (v_0 - v)^2}{D} dv, \qquad (2.28)$$

which is the modified equation of particle diffusion-advection (compare to equation 2.9).

2.3.1 Advection and non-linear diffusion

The velocity diffusion coefficient $D \propto W$ is determined by the level of Langmuir waves. Taking the spectral energy density of Langmuir waves W^0 given by equation (2.15), one can write for D:

$$D = \pi \frac{\omega_{pe}}{v_0} \frac{n(x,t)}{n_p} v^3 \left(1 - \frac{v}{v_0} \right) = D_0 v^3 \left(1 - \frac{v}{v_0} \right) , \qquad (2.29)$$

where $D_0 = \pi \frac{\omega_{pe}}{v_0} \frac{n(x,t)}{n_p}$. Finally substituting (2.29) into (2.28) and integrating from v_{\min} (instead of 0 as in equation 2.28) leads us to advection diffusion equation

$$\frac{\partial n}{\partial t} + \frac{v_0}{2} \frac{\partial n}{\partial x} - \frac{\partial}{\partial x} D_{xx} \frac{\partial n}{\partial x} = 0, \tag{2.30}$$

with the non-linear spatial diffusion coefficient given by

$$D_{xx} = \frac{1}{4v_0} \int_{v_{\text{min}}}^{v_0} \frac{v^2 (v_0 - v)^2}{D} dv = \frac{v_0^2 n_p}{4\pi \omega_{pe} n(x, t)} \left(\ln \frac{v_0}{v_{\text{min}}} - 1 \right) \propto \frac{v_0^2}{4} \tau_q.$$
 (2.31)

The spatial diffusion coefficient (2.31) is dependent on the beam density and is smaller for smaller quasilinear time. In other words, the stronger the beam (larger n_b), the slower the diffusion term (smaller D_{xx}). A diffusion coefficient with $\propto 1/n(x,t)$ is often named *fast diffusion* i.e. diffusion is fast in regions where the density of particles is low (Juan R. Esteban and Vázquez 1988; Vázquez 2017).

An important peculiarity of the solution (2.31) is that integration was carried out from v_{\min} and when $v_{\min} \to 0$, $D_{xx} \to \infty$. The divergence has a physical reason: the plateau down to zero velocity is formed at $t \to \infty$, so the diffusion coefficient is infinite when $v_{\min} \to 0$. While the plateau is quickly formed over a broad range of velocities (over quasilinear time τ_q), the growth rate of the Langmuir waves is actually zero at v=0, as one can see from equation (2.2). Indeed, numerical simulations (e.g. Kontar et al. 1998; Kontar 2001c) show that the relaxation proceeds down to a small but finite velocity. In plasma with a Maxwellian distribution of thermal particles, the plateau is also formed between maximum beam velocity and thermal distribution, so that $v_{\min} \simeq 3 - 4v_{T_e}$ (Kontar and Pécseli 2002; Ziebell et al. 2008, 2011; Sauer et al. 2019).

Therefore, in order to compare the analytical model to the results of the numerical simulations or observations, a constant lower bound v_{\min} is included to the plateau in velocity, resulting in the new electron distribution function

$$f^{0}(v, x, t) = \begin{cases} p(x, t), & v_{\min} < v < u(x, t) \\ 0, & v \le v_{\min}, v \ge u(x, t) \end{cases}$$
 (2.32)

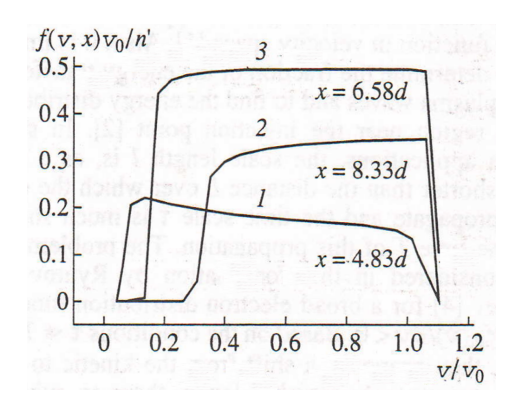


Figure 2.1: Figure 1 from Kontar et al. (1998) showing the result of the numerical simulations for the spreading of a monoenergetic electron beam in the weak turbulence approximation. Here $v_0 \sim 10^{10}$ cm s⁻¹, with $v_{\rm min}$ of the beam shown to be non-zero. The distribution function f(v,x) here is plotted at t=3s at different distances from the injection point.

and the spectral energy density of Langmuir waves

$$W^{0}(v, x, t) = \begin{cases} W_{0}(v, x, t), & v_{\min} < v < u(x, t) \\ 0, & v \leq v_{\min}, v \geq u(x, t) \end{cases}$$
 (2.33)

where the solution for u(x,t), p(x,t), and $W_0(x,v,t)$ can be found following Kontar et al. (1998) to be

$$u(x,t) = v_0, (2.34)$$

$$p(x,t) = \frac{n_b}{v_0 - v_{\min}} \exp\left[-\frac{(x - (v_0 + v_{\min})t/2)^2}{d^2}\right],$$
 (2.35)

$$W_0(v, x, t) = \frac{m}{\omega_{pe}} v^3(v - v_{\min}) \left(1 - \frac{v + v_{\min}}{v_0 + v_{\min}} \right) p(x, t), \tag{2.36}$$

The obvious difference from the solution (2.13-2.15) is that the solution (2.34-2.36) accounts for the minimum velocity of a plateau. This provides a more realistic description of the beam-plasma interaction, as v=0 electrons cannot interact resonantly with the wave. Another consequence of v_{\min} is that electron density is now given by

$$n(x,t) = \int_{v_{\min}}^{v_0} p(x,t) \, dv = p(x,t) (v_0 - v_{\min}) , \qquad (2.37)$$

with a new diffusion equation

$$\frac{\partial n}{\partial t} + \frac{v_0 + v_{\min}}{2} \frac{\partial n}{\partial x} + \frac{\partial}{\partial x} \int_{v_{\min}}^{v_0} v f^1 dv = 0.$$
 (2.38)

Integrating equation (2.16) over velocity from v_{\min} to ∞ , one obtains

$$\frac{\partial n}{\partial t} + \frac{v_0 + v_{\min}}{2} \frac{\partial n}{\partial x} + \frac{\partial}{\partial x} \int_{v_{\min}}^{v_0} v f^1 dv = 0.$$
 (2.39)

Multiplying equation (2.16) by $v_0 - v_{\min}$ and subtracting by equation (2.39) one finds, at zeroth order

$$\frac{1}{v_0 - v_{\min}} \left(v - \frac{v_0 + v_{\min}}{2} \right) \frac{\partial n}{\partial x} = \frac{\partial}{\partial v} D \frac{\partial f^1}{\partial v}, \qquad (2.40)$$

which is the equation for f^1 . Integrating equation (2.40) over v, one obtains

$$D\frac{\partial f^{1}}{\partial v} = \frac{1}{v_{0} - v_{\min}} \frac{\partial n}{\partial x} \int_{v_{\min}}^{v} \left(v' - \frac{v_{0} + v_{\min}}{2}\right) dv'$$

$$= \frac{1}{v_{0} - v_{\min}} \frac{\partial n}{\partial x} \frac{1}{2} \left(v - v_{\min}\right) \left(v - v_{0}\right) + C_{1}.$$
(2.41)

Since quasilinear relaxation operates now on $v_{\min} < v < v_0$, the boundary conditions on D are $D|_{v=v_{\min}} = D|_{v=v_0} = 0$. As before, $C_1 = 0$, yielding

$$\frac{\partial f^1}{\partial v} = \frac{(v - v_{\min})(v - v_0)}{2(v_0 - v_{\min})D} \frac{\partial n}{\partial x}.$$
 (2.42)

Further integration over v yields the expression for f^1

$$f^{1} = \frac{1}{2(v_{0} - v_{\min})} \frac{\partial n}{\partial x} \int_{v_{0}}^{v_{0}} \frac{(v' - v_{\min})(v' - v_{0})}{D} dv' + C_{2}, \qquad (2.43)$$

where the same method as section (2.3) is used to determine

$$C_{2} = \frac{1}{2(v_{0} - v_{\min})^{2}} \frac{\partial n}{\partial x} \int_{v_{\min}}^{v_{0}} (v_{0} - v')^{2} \frac{(v' - v_{\min})}{D} dv'.$$
 (2.44)

Finding f^1 leads to

$$\int_{v_{\min}}^{v_0} v f^1 dv = -\frac{1}{4(v_0 - v_{\min})} \frac{\partial n}{\partial x} \int_{v_{\min}}^{v_0} \frac{(v - v_{\min})^2 (v_0 - v)^2}{D} dv .$$
 (2.45)

Similarly to the previous subsection, the expression for D can be found from the formula for the spectral energy density $W_0(x,v,t)$ and the plateau height p(x,t). Following Kontar et al. (1998), non-zero v_{\min} leads to

$$D = D_0 v^2 \left(v - v_{\min} \right) \left(1 - \frac{v + v_{\min}}{v_0 + v_{\min}} \right), \tag{2.46}$$

where now $D_0 = \pi \frac{\omega_{pe}}{(v_0 - v_{\min})} \frac{n(x,t)}{n_p}$.

Inserting this D into equation (2.45), yields

$$\int_{v_{\text{min}}}^{v_0} v f_1 dv = -\frac{v_0 + v_{\text{min}}}{4D_0} \left(\frac{v_0 + v_{\text{min}}}{v_0 - v_{\text{min}}} \ln \frac{v_0}{v_{\text{min}}} - 2 \right) \frac{\partial n}{\partial x}, \tag{2.47}$$

and the advection-nonlinear-diffusion becomes

$$\frac{\partial n}{\partial t} + \frac{(v_0 + v_{\min})}{2} \frac{\partial n}{\partial x} - \frac{\partial}{\partial x} D_{xx} \frac{\partial n}{\partial x} = 0, \tag{2.48}$$

where the new diffusion coefficient D_{xx} that includes v_{\min} is now given by

$$D_{xx} = \frac{v_0^2 - v_{\min}^2}{4\pi\omega_{pe}} \frac{n_p}{n(x,t)} \left(\left(\frac{v_0 + v_{\min}}{v_0 - v_{\min}} \right) \ln \frac{v_0}{v_{\min}} - 2 \right) =$$

$$= \frac{v_0^2 - v_{\min}^2}{4\pi} \tau_q \left(\left(\frac{v_0 + v_{\min}}{v_0 - v_{\min}} \right) \ln \frac{v_0}{v_{\min}} - 2 \right).$$
(2.49)

The spatial diffusion coefficient D_{xx} is inversely proportional to electron number density n(x,t), so the spatial diffusion is faster for longer quasilinear time $\tau_q \sim n_p/(\omega_{pe}n(x,t))$. The diffusion coefficient D_{xx} is zero when $v_{\min} = v_0$, i.e. spatial diffusion is not possible without quasilinear relaxation. The electron beam diffusion coefficient (equation 2.49) is also dependent on v_{\min} , so the spatial expansion of electron beam is larger for smaller v_{\min} .

2.4 Asymptotic solution to advection-nonlinear-diffusion equation

Consider the evolution of an electron beam with initial condition

$$n(x,t=0) = n_b \delta(x/d) , \qquad (2.50)$$

where n_b is the electron beam density and d is the characteristic size. The advection-nonlinear diffusion equation (2.48) with n(x,t) normalised with n_b can be rewritten as

$$\frac{\partial n}{\partial t} + \frac{v_0 + v_{min}}{2} \frac{\partial n}{\partial x} - \frac{\partial}{\partial x} D_{xx}^0 \frac{n_b}{n} \frac{\partial n}{\partial x} = 0, \qquad (2.51)$$

where the nonlinear dependency of D_{xx} on n(x,t) is explicitly highlighted by introducing $D_{xx} = D_{xx}^0 \frac{n_b}{n}$. The equation (2.51) can be solved for constant v_0 and v_{\min} to find the asymptotic solution

$$n(x,t) = \left(\frac{(x - (v_0 + v_{\min})t/2)^2}{2D_{xx}^0 n_b t} + \frac{2\pi^2}{n_b d^2} D_{xx}^0 t\right)^{-1} =$$

$$= \frac{n_b}{\pi} \frac{2\pi D_{xx}^0 t/d^2}{(x - (v_0 + v_{\min})t/2)^2/d^2 + 4\pi^2 (D_{xx}^0 t)^2/d^4},$$
(2.52)

which is a Lorentzian

$$L(x') = \frac{1}{\pi} \frac{\gamma}{x'^2 + \gamma^2} \,, \tag{2.53}$$

where $x'=(x-(v_0+v_{\min})t/2)/d$ and $\gamma=2\pi D_{xx}^0t/d^2$. The solution (2.52) describes the expanding electron beam moving with the speed $(v_0+v_{\min})/2$. The electron beam size given by γ is proportional to time t, and for $t\to 0$, $n(x,t)\to n_b d\delta(x)$, which is the initial condition (2.50). n(x,t) given by (2.52) also conserves the number of particles $\int_{-\infty}^{+\infty} n(x,t) \mathrm{d}x = dn_b$ as expected.

The solution (2.52) shows that the electron beam always expands with time or with distance, so the peak of the beam at $x = (v_0 + v_{\min})t/2$ decreases following:

$$n\left(x, t = \frac{2x}{v_0 + v_{\min}}\right) = \frac{n_b d}{\pi} \frac{(v_0 + v_{\min})d}{4\pi x D_{xx}^0} \propto \frac{d}{x},$$
 (2.54)

which is an important result for the theory of type III bursts. The plausible decrease of electron number density with distance 1/x would be preferable to explain the intensity of type III burst with distance (e.g. Krupar et al. 2014; Sasikumar Raja et al. 2022).

Another interesting consequence of the solution (2.52) is that the beam size is growing with time or distance. Full Width at Half Maximum (FWHM) of the electron beam Δx is

$$\Delta x = 2\gamma d = \frac{4\pi}{d} D_{xx}^0 t = \frac{4\pi}{d} D_{xx}^0 \frac{2x}{(v_0 + v_{\min})} \propto \tau_q \frac{x}{d}, \qquad (2.55)$$

or dividing by the average speed of the electron beam $(v_0 + v_{\min})/2$, one obtains the temporal FWHM of the beam

$$\Delta t = \frac{4\gamma d}{v_0 + v_{\min}} = \frac{4\pi}{d} D_{xx}^0 \frac{2t}{(v_0 + v_{\min})} = \frac{4\pi}{d} D_{xx}^0 \frac{4x}{(v_0 + v_{\min})^2} \propto \tau_q \frac{x}{d}, \qquad (2.56)$$

where the spatial expansion of the beam Δx is linearly growing with time $\Delta x \propto t$ or the particles propagate ballistically, which is the special case of super-diffusion. Constant spatial diffusion coefficient leads to $\Delta x \propto t^{1/2}$, but the non-linear diffusion $D_{xx} \propto 1/n(x,t)$ due to Langmuir wave turbulence makes the electron beam expand "faster", i.e. $\Delta x \propto t$ which is so-called super-diffusion (e.g. Okubo et al. 1984; Treumann 1997; Zimbardo et al. 2006). Here, the Langmuir turbulence is self-consistently generated as the electron beam propagates and expands in space. The level of Langmuir turbulence is proportional to the number of particles that gives the nonlinearity of the diffusion coefficient.

2.4.1 Initially finite beam dynamics

For comparison with observations and numerical simulations, consider the initial electron number density function as a Gaussian with characteristic size d, which is similar to the initial condition in Kontar et al. (1998), i.e. the electron distribution function at t=0 is

$$f(v, x, t = 0) = \frac{2n_b}{v_0} \frac{v}{v_0} \exp\left(-\frac{x^2}{d^2}\right), \quad 0 < v < v_0,$$
 (2.57)

hence the number density of beam electrons

$$n(x, t = 0) = n_b \exp(-x^2/d^2)$$
, (2.58)

with the total number of particles $\int_{-\infty}^{+\infty} n(x,t)dx = n_b d\sqrt{\pi}$. Then the solution of advection-nonlinear-diffusion equation (2.51) is the convolution of the initial condition (2.58) and the Lorentzian from equation (2.52) normalised to 1, which is the solution to the Dirac delta function initial condition (the Green's function solution, which is an approximation when D_{xx} is nonlinear, see e.g. Kheifets (1984), Frasca

(2008) and Frank (2009)):

$$n(x,t) = \frac{n_b}{\pi} \int_{-\infty}^{\infty} \frac{2\pi D_{xx}^0 t/de^{-s^2/d^2} ds}{(x - s - \frac{v_0 + v_{\min}}{2} t)^2 + 4\pi^2 (D_{xx}^0 t)^2/d^2} =$$

$$= n_b \frac{\gamma}{\pi} \int_{-\infty}^{\infty} \frac{e^{-y^2} dy}{(\eta - y)^2 + \gamma^2} = n_b V(\gamma(t), \eta(x, t)),$$
(2.59)

where $\eta(x,t) = (x - (v_0 + v_{\min})t/2)/d$, $\gamma(t) = 2\pi D_{xx}^0 t/d^2$, y = s/d, and

$$V(\gamma, \eta) \equiv \frac{\gamma}{\pi} \int_{-\infty}^{\infty} \frac{e^{-y^2} dy}{\gamma^2 + (\eta - y)^2},$$
(2.60)

is the Voigt profile (Abramowitz and Stegun 1970), which is a convolution of Gaussian and Lorentzian, often used to fit spectral lines (e.g. Jeffrey et al. 2016).

In case of the solution (2.59), the width of the electron beam is a combination of Lorentzian FWHM given by equation (2.55) and the FWHM of the Gaussian (2.58), which is $\Delta x_G = 2\sqrt{\ln 2}d \simeq 1.67d$. The Voigt profile can be approximated as (Whiting 1968):

$$\Delta x_{\rm V} \approx \Delta x/2 + \sqrt{\Delta x^2/4 + \Delta x_{\rm G}^2} \sim \sqrt{\Delta x_{\rm G}^2 + \Delta x^2},$$
 (2.61)

which shows that the electron beam of size d is expanding ballistically with time $\Delta x \propto t$, when $\Delta x \gg d$. The speed of the expansion (Equation 2.55) is controlled by the quasilinear time. Smaller/larger quasilinear time leads to slower/faster spatial electron beam expansion.

Figure 2.2 shows the spatial evolution of electron beam for the beam-plasma parameters used in the numerical simulations by Kontar et al. (1998). Unlike the solution assuming constant quasilinear time (Equation (2.14)), Equation (2.59) is much closer in describing the simulated density profile showing both the decrease of the peak density and electron beam expansion (Figure 2 in Kontar et al. 1998).

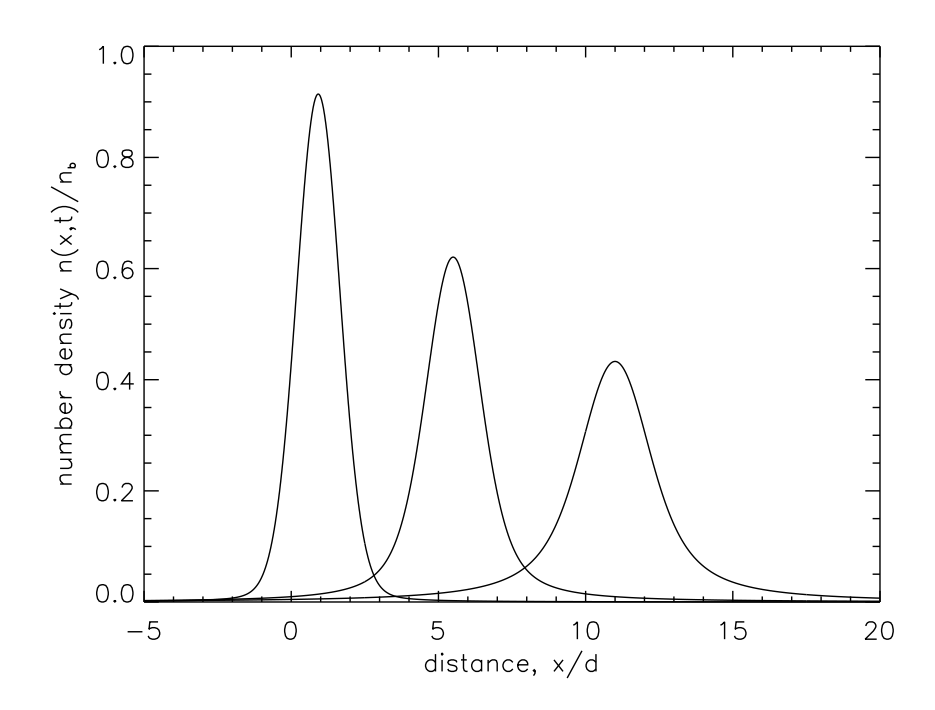


Figure 2.2: Electron number density profile $n(x,t)/n_b$ for the beam-plasma parameters as in the numerical simulations by Kontar et al. (1998): $n_b=12~{\rm cm}^{-3}$, $n_p=6\times 10^8~{\rm cm}^{-3}$ (i.e. $f_{pe}\simeq 220~{\rm MHz}$) and $v_0=10^{10}~{\rm cm/s}$, $v_{\rm min}=0.1v_0$, $d=3\times 10^9~{\rm cm}$. The three curves are the density profiles given by the solution (Equation 2.59) for t=0.5,3,6 seconds. Figure made by Eduard P. Kontar

Using the solution for electron beam spread (Equation (2.59)), the spectral energy density of the Langmuir waves (Equation 2.36) becomes

$$W = n(x,t)\frac{m}{\omega_p}v^3 \frac{v - v_{\min}}{v_0 - v_{\min}} \left(1 - \frac{v + v_{\min}}{v_0 + v_{\min}}\right), \qquad (2.62)$$

so the spectral energy density decreases with distance due to the spatial evolution of n(x,t).

The electron density at the peak $n(x,t=2x/(v_0+v_{\min}))$ decreases with distance following

$$\frac{n\left(x, t = \frac{2x}{v_0 + v_{\min}}\right)}{n_b} = V\left(\gamma\left(t = \frac{2x}{v_0 + v_{\min}}\right), \eta = 0\right),\tag{2.63}$$

where $\gamma(x,t=2x/(v_0+v_{\min}))=4\pi D_{xx}^0x/((v_0+v_{\min})d^2)$. Figure 2.3 shows the peak value (Equation 2.63) as a function of distance.

The width variation, or the time required to pass a specific point in space for a beam, would correspond to type III burst duration at a given frequency. Interestingly, type III observations, similar to the predictions of ballistic expansion (Figure 2.3), also show expansion (Figure 10 in Reid and Kontar 2018). The detailed comparison would require taking into account radio-wave propagation. The rate of expansion is dependent on density and can be a new valuable diagnostic of electron beam density in type III bursts. This is also apparent from Figures 2.4 and 2.5, where the temporal evolution of simulated electron distribution, spectral energy density and electron beam density is shown for $n_b = 12 \text{ cm}^{-3}$ and $n_b = 120 \text{ cm}^{-3}$. The value of v_{\min} was chosen to be the minimum velocity value at half maximum of the electron distribution. It is evident that higher densities correspond to shorter quasilinear times of interaction, resulting in a better fit between simulations and the analytical solution.

2.5 Summary

This chapter develops a quantitative analytical model of the electron transport responsible for type III solar radio bursts. The developed model takes into account the finite size of the electron beam, so the generation of Langmuir waves and quasilinear relaxation proceeds faster in the regions of higher electron number density. In the limit of small quasilinear time, the hydrodynamic approach yields the advection-nonlinear-diffusion equation for electron number density. Since the rate of relaxation of electrons is governed by the beam density at different spatial locations, the non-linear diffusion coefficient is inversely proportional to the beam density $D_{xx} \propto 1/n(x,t)$, process known as fast diffusion. Low electron beam density away from the peak of the electron beam leads to faster spatial diffusion of electrons.

The model has an elegant analytical solution showing that the electron beam propagates at constant speed $(v_0+v_{\min})/2$ but with varying spatial width. The electron beam spatial size grows with the rate dependent on quasilinear time τ_q . The spatial width of the electron beam is proportional to τ_q and to time t at large $x\gg d$. Unlike a linear diffusion case, when the beam size increases as $\propto \sqrt{t}$, the nonlinear diffusion leads to ballistic (super-diffusion) expansion i.e. electron beam size is $\propto t$ at large distances $t\gg t$ (see lower panel in Figure 2.3 and equation 2.55). Although the spatial expansion is linear with time, the rate of the expansion could be small for small quasilinear times $t \approx t \approx t$ at large densities (compare Figures 2.5 and 2.4).

The spatial expansion of the electron beam leads to the decrease of its peak density. For large $x \gg d$, when the expansion is $\propto x$, the maximum beam density decreases as $\propto 1/x$, with the rate dependent on the beam density. The spectral energy density of Langmuir waves is also decreasing as $\propto 1/x$. Moreover, the spatial distribu-

tion of electrons is in quantitative agreement with the numerical solutions of kinetic equations, where both numerical solutions and analytical solutions present Voigtlike profiles (Figure 2.2). Similar to the simulations, the peak electron density in the beam decreases with distance at the rate similar to the numerical solution (Figure 2 in Kontar et al. (1998)). The analytical solution also shows that, on top of advection with constant speed, $(v_0 + u_{\min})/2$, the nonlinear diffusion leads to spatial expansion of the electron beam with time. The FWHM of the electron beam, in the analytical solution is shown to be expanding ballistically, i.e. $\Delta x \propto t$ for $\Delta x \gg d$. The expansion of the electron beam is faster further away from the beam center due to larger local quasilinear time since $D_{xx} \propto 1/n(x,t)$ (Equation 2.55).

In application to type III solar radio bursts, the spectral energy density of plasma emission via Langmuir waves depends on the beam density and would decrease $\propto 1/x$, which is required to explain the radial type III solar burst flux variations (Krupar et al. 2014). The spatial expansion of the beam is also qualitatively a better fit for the time width of type III bursts (Reid and Kontar 2018).

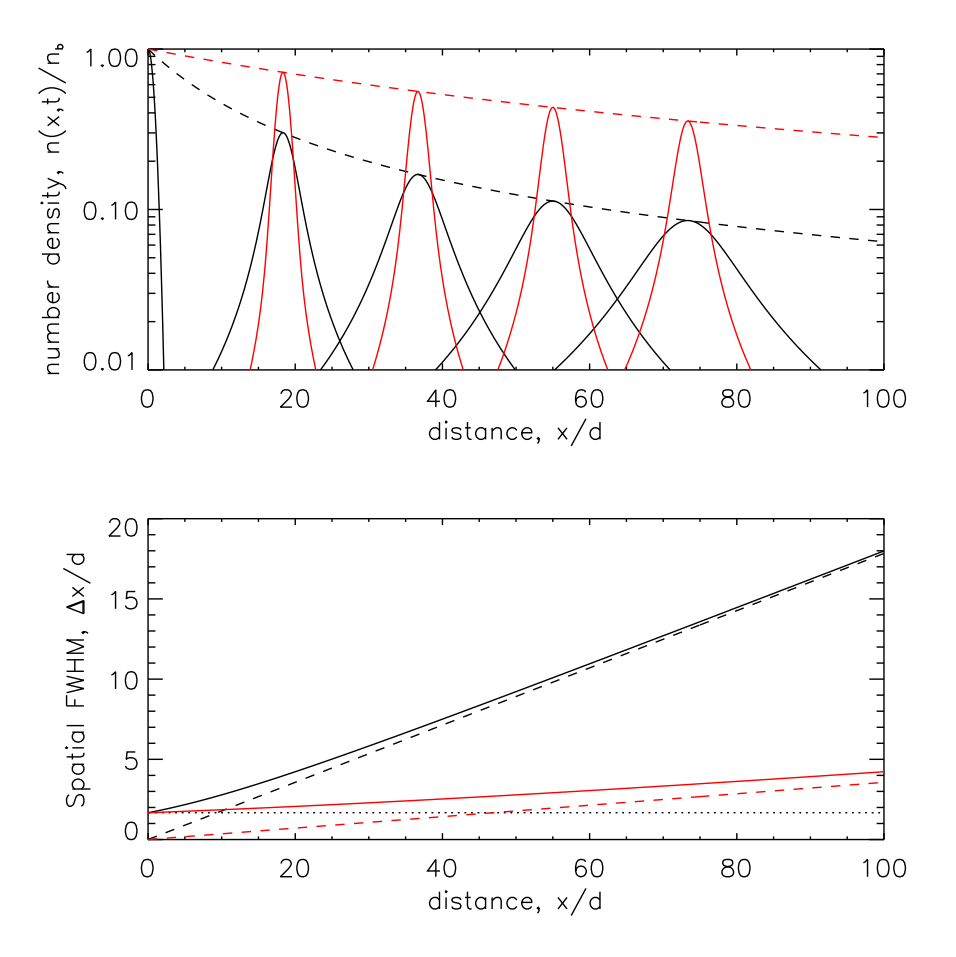


Figure 2.3: Top panel: Electron number density profile $n(x,t)/n_b$ at t=0,20,40,60 seconds for the same beam plasma parameters as in Figure 2.2 $n_b=12~{\rm cm}^{-3}$ in black and $n_b=60~{\rm cm}^{-3}$ in red . Bottom panel: FWHM width of the beam given by equation 2.61 (solid line). The dashed line is the width of Lorentzian (Equation 2.55). The horizontal dashed line is Gaussian FWHM, $\Delta x_G \simeq 1.67d$. Black lines are for $n_b=12~{\rm cm}^{-3}$ and red lines are for $n_b=60~{\rm cm}^{-3}$. Figure made by Eduard P. Kontar

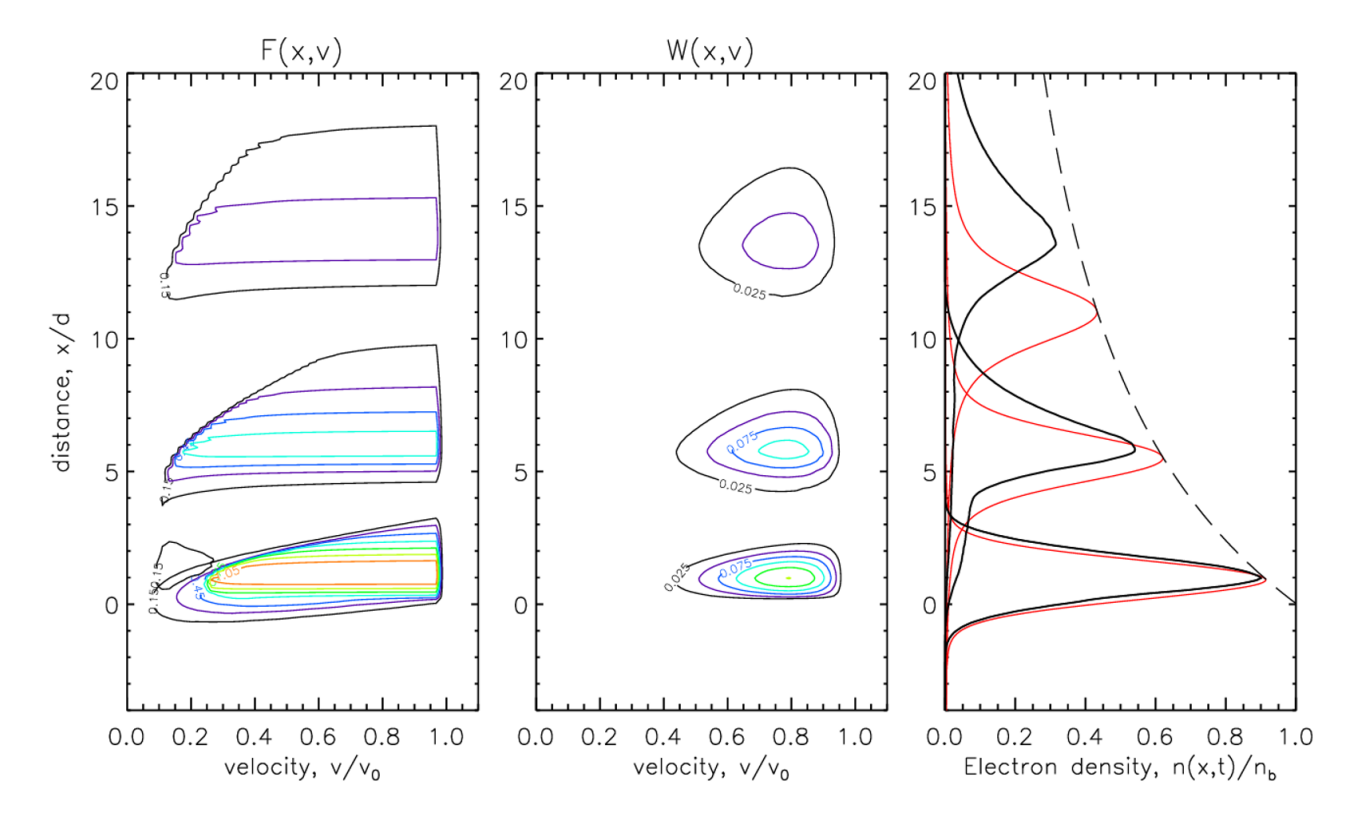


Figure 2.4: Simulated electron distribution f(x,v,t) (left), spectral energy density W(x,v,t) (center), and electron beam density n(x,t) (right) at three time moments t=0.5,3,6 s for the following beam–plasma parameters: $n_b=12~{\rm cm}^{-3}$, $n_p=6\times 10^8~{\rm cm}^{-3}$ (i.e., $f_{pe}\simeq 220~{\rm MHz}$), $v_0=10^{10}~{\rm cm/s}$, $v_{\rm min}=0.1v_0$, and $d=3\times 10^9~{\rm cm}$. The analytical density profile (2.59) is plotted in red, with the black dashed line showing its peak as a function of distance.

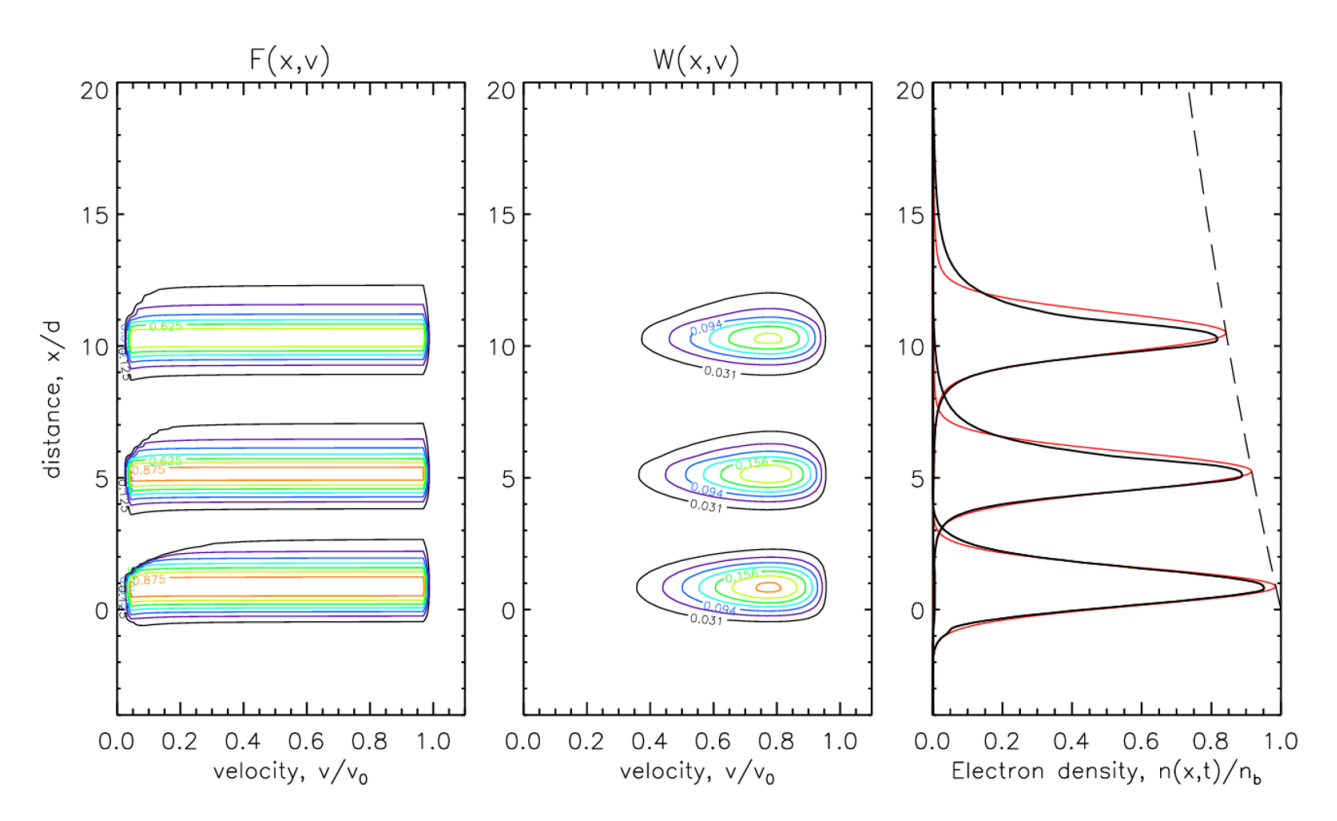


Figure 2.5: The same as Figure 2.4 but for $n_b = 120 \text{ cm}^{-3}$.

Chapter 3

A Multispacecraft Analysis and Modeling of Type III Radio Burst Exciter Deceleration in Inhomogeneous Heliospheric Plasma

3.1 Introduction

This chapter is based on recently submitted work by Azzollini and Kontar (2025), with the author of this thesis as first author. Eduard P. Kontar acts as second author, providing invaluable advice and guidance throughout the project. They contributed majorly to the concepts of section 3.4 and part of section 3.5.

3.1. Introduction 66

Early observations of Type III burst drift rates suggest that high velocity electron beams with speed $\sim 0.3c$, where c is the speed of light, are required as the exciters to account for the high frequency drift rates in the corona (Wild 1950; Ginzburg and Zhelezniakov 1958). The electron beams that generate Langmuir waves are believed to move through the plasma, forming a slowly expanding beam-plasma structure (Kontar et al. 2024). While the speeds of the electrons generating coronal type III burst is ~ 30 keV (e.g. Aschwanden et al. 1995), the electrons exiting Langmuir waves at 1 au are typically below a few keV (Lin 1985), suggesting type III generating electron deceleration from $\sim c/3$ to well below $\sim 0.1c$. However, the exact radial deceleration profile is poorly understood. Simulations by Kontar (2001a) and Reid and Kontar (2013) show that the speed of electrons responsible for Langmuir wave generation decreases with distance. The effect is attributed to the decreasing density. Using the quasilinear approach, Lorfing and Reid (2023) demonstrate that the electron beam velocity of 0.38c at $5R_{\odot}$ decreases as $r^{-0.5}$ to 0.16c at $50R_{\odot}$. To compare with observations, the poorly-known spatial location of the electron source in the solar corona and associated time-delay of the type III source could play an important role in precise velocity/acceleration determinations. Therefore, type III observations with spatial localization of the source are preferable.

Simultaneous multi-spacecraft observations allow to account for source-spacecraft angular separation to derive exciter velocities and accelerations (Section 3.2). The latter are compared to predictions from a kinetic model describing the evolution of an electron plasma structure propagating through ambient plasma with a negative electron density gradient, offering insights into the dynamics of the type III burst exciters. Section 3.4 provides a simple but extremely useful insight into electron beam deceleration due to decreasing density in the inhomogeneous plasma of interplanetary space. The comparison of the observations and the theoretical model provides good agreement.

3.2 Multi-spacecraft observations of type III burst sources

The following analysis uses data recorded by the Low Frequency Receiver (LFR) of the Radio Frequency Spectrometer (RFS) on PSP (64 logarithmically spaced channels ranging from 10 kHz to 1.7 MHz, with 4-7 s time resolution), the S/WAVES High Frequency Receiver (HFR) on STEREO-A (frequency resolution of 25 kHz and a 35-38 s time resolution), the RPW (HFR) instrument on Solar Orbiter (SolO) (time resolution of \sim 17s and 25 kHz spectral resolution) and the Wind/WAVES aboard the Wind spacecraft (time resolution of \sim 60s and 4 kHz spectral resolution). Background levels, calculated using median values over 10 minutes before the event, are subtracted from the data to improve the signal-to-noise ratio.

This work analyses type III radio burst events recorded on 11 July 2020 (Figure 3.1). Frequency drifts are analyzed for frequencies below 1 MHz due to instrument time resolution. The type III burst data have sufficiently high frequency and time resolution, with data points forming a smooth, monotonic relationship between peak time and frequency (see left panel in Figure 3.1).

Simultaneous observations of the same type III burst from different spacecraft allows to determine the peak of type III burst directivity and hence the source angular location (see Figure 3.2). Following the approach by Chen et al. (2023), Musset et al. (2021) and Clarkson et al. (2025), the source-spacecraft angular separations $\phi = \theta_0 - \theta_{s/c}$ are found to be ~94°, ~185° and ~10° for PSP, STEREO-A and SolO respectively (Figure 3.2). Anisotropic emission is modelled after Equation 1.20, us-

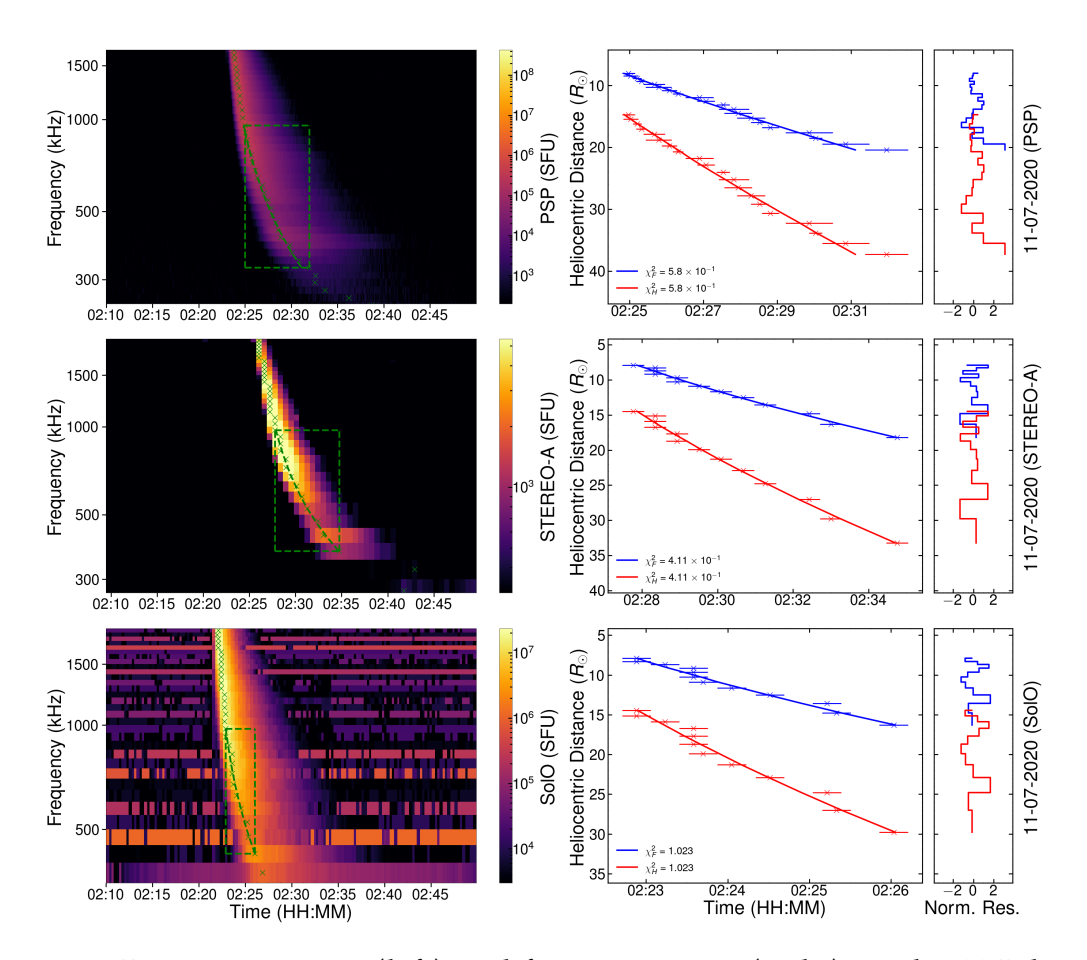


Figure 3.1: Dynamic spectra (left) and frequency-time (right) on the 11 July 2020 by the PSP, STEREO-A and SolO spacecraft (from top to bottom). For each spacecraft, the peak flux frequencies (and the fit) are plotted on the right for the timesfrequencies selected by the green dashed box, containing peak flux points (green "X" symbols), along with their fitted curve (green dashed line), while the χ^2 -fitted positions of the emitter as a function of time, obtained by using the density model from Equation (3.5), and the normalized residuals from the fit are shown on the right. Blue and red lines correspond, respectively, to the fundamental and harmonic components. The steepening of the PSP profile may be attributed to scattering projection effects.

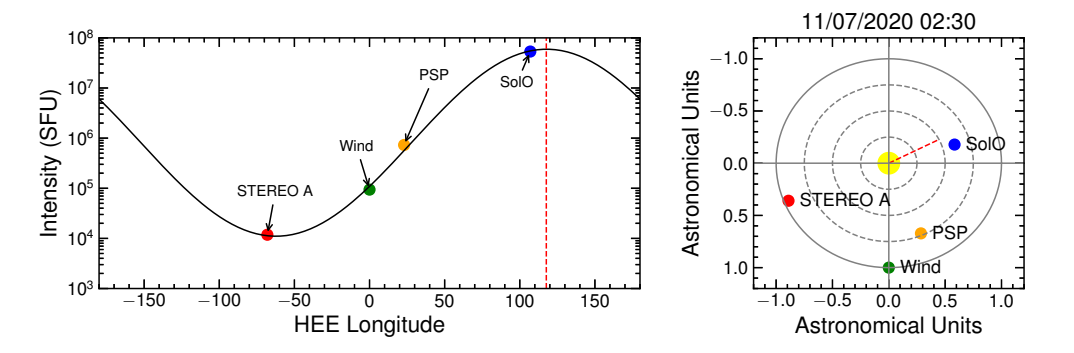


Figure 3.2: Type III burst peak fluxes measured by the four different spacecraft (left), as well as spacecraft positions (right) in HEE coordinates during the 11 July 2020 (2:30 UT) event. The direction of maximum directivity is found by fitting Equation 1.20 for the peak fluxes from STEREO-A, PSP, Wind and SolO at 979 kHz. This frequency was selected on the assumption that for $\gtrsim 1$ MHz, the Sun's magnetic field is approximately radial. In this region, radio waves are subject to anisotropic scattering, with the anisotropy aligned along the heliospheric magnetic field (Clarkson et al. 2025). As a result, the propagation of the waves is preferentially guided along the magnetic field, leading the apparent radio sources to appear shifted in the radial direction. On the left peak fluxes are plotted as a function of HEE Longitude. The red dashed line shows the position of the radio source as revealed by the directivity fit. On the right are the position of Solar Orbiter, Parker Solar Probe, STEREO-A and Wind projected in the plane of the HEE coordinate system.

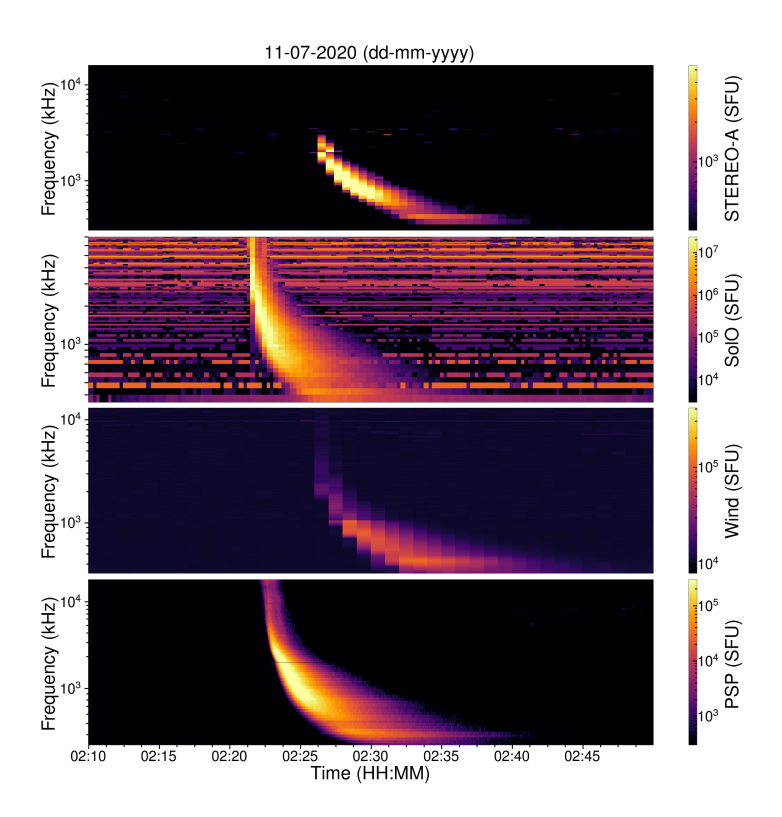


Figure 3.3: Dynamic spectra of the 11 July 2020 02:30 UT type III radio burst observed from STEREO-A, SolO, Wind and PSP.

ing $\Delta\mu=0.22$ from Musset et al. (2021). For the range of frequencies between 2-0.5 MHz considered, the radial motion of electrons is a good approximation since the curvature of the Parker spiral at these distances (order of $10R_{\odot}$, where R_{\odot} is the solar radius) is rather small.

To determine the drift rate of type III burst source, one needs to take into account the direction of exciter motion with respect to the observing spacecraft, e.g. the angular separation $\phi = \theta_0 - \theta_{s/c}$ that affects the drift rate derivation. Similarly to Hughes and Harkness (1963), Ledenev (2000) and Melnik et al. (2011, 2015), if a source is moving radially, with a constant velocity $v_{\rm s}$ at an angle ϕ to the line-of-sight and generating radio-waves at points r_1 and r_2 (Figure 3.4), the time difference between the arrivals of these waves to the observer is

$$\Delta t \approx \frac{\delta r}{v_{\rm s}} \frac{c - v_{\rm s} \cos \phi}{c} \,, \tag{3.1}$$

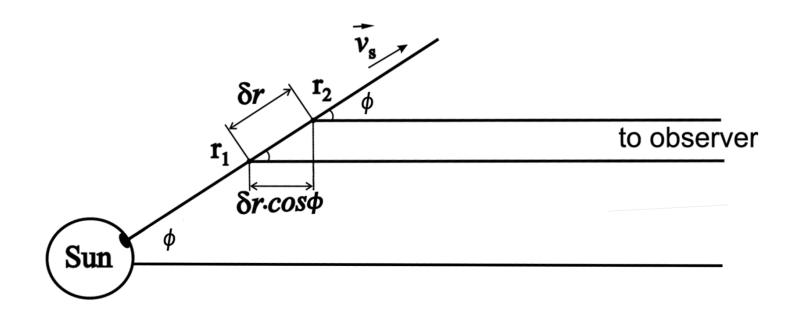


Figure 3.4: Type III exciter propagating from position r_1 to r_2 with constant velocity v_s at an angle ϕ to the line of sight. This simple representation allows to correct for the source-to-spacecraft light travel time (Equation 3.1).

where $\delta r=r_2-r_1$ is the radial distance traveled. Only for nearly perpendicular to the line-of-sight motion $\Delta t \approx \frac{\delta r}{v_{\rm s}}$ is unaffected by the radio-wave propagation.

Using Equation (3.1), the speed over the distance δr can be written

$$\frac{\delta r}{\delta t} = v_s \frac{c}{c - v_s \cos \phi} \,. \tag{3.2}$$

Hence, the drift rate can be written

$$\frac{\delta f}{\delta t} = \frac{df}{dr} \frac{\delta r}{\delta t} = \frac{df}{dr} \frac{cv_s}{c - v_s \cos \phi} \simeq \frac{df}{dt} (1 + v_s/c \cos \phi), \tag{3.3}$$

where f could be either plasma frequency or its harmonic. The second term in Equation 3.3 presents the correction due to the radio-wave travel time with speed c. One can see that the correction is larger for larger exciter speeds v_s . The correction is also zero for $\phi = 90^{\circ}$, i. e. the emission travels the same distance and there is no frequency dependent delay. Note that Krupar et al. (2015) used different angle definition in their appendix, so that their correction is zero for the deviation angle $\Delta \phi$.

Following previous research works (e. g. Krupar et al. 2015), the drift-rate of type III bursts is determined using the flux maximum for each frequency (see Figure 3.1), i.e. fitting the frequency as a function of time using the power-law model

$$f_i = A_i (t_i - t_{0i})^{B_i} , (3.4)$$

where i = F, H depending on whether the observed emission is assumed to produced at the fundamental (F) or the second harmonic (H) of the local plasma frequency, reflecting the underlying radio emission mechanism (see Section 1.5.1). Then, the observed frequency can be related to the spatial location using the density model

$$n(r) = 1.4 \times 10^6 (R_{\odot}/r)^{2.3} \text{ [cm}^{-3]},$$
 (3.5)

which is a power-law fit (see Kontar et al. 2023, for details) to the Parker (1960) model with constant temperature and constants chosen to agree with in-situ density measurements at 1 au adapted by Mann et al. (1999). Frequency as a function of time is also a power-law function

$$f_i = C \left(\frac{r_i}{R_{\odot}}\right)^D \simeq 10.53 \left(\frac{r_i}{R_{\odot}}\right)^D [\text{MHz}],$$
 (3.6)

where $C = 8.9 \sqrt{1.4}$ and D = -2.3/2 can be found using density model. This approximation yields densities within 20% of the density models for the range of frequencies considered here (see Figure 11 by Kontar et al. (2023) for the comparison with different density models).

Given the density model (Equation 3.5), one can find the parameters α_i and β_i for the power-law model from Krupar et al. (2015)

$$v_i = \alpha_i \left(\frac{r_i}{R_\odot}\right)^{\beta_i},\tag{3.7}$$

with $\alpha_i = \frac{B_i}{D} \left(\frac{A_i}{C}\right)^{\frac{1}{B_i}}$ and $\beta_i = 1 - \frac{D}{B_i}$, and v_i normalized in units of $R_{\odot}/$ s; as well as parameters γ_i and δ_i from the exciter acceleration power-law model

$$a_i = \gamma_i \left(\frac{r_i}{R_{\odot}}\right)^{\delta_i} \,, \tag{3.8}$$

with
$$\gamma_i = \frac{B_i}{D} \left(\frac{B_i}{D} - 1 \right) \left(\frac{A_i}{C} \right)^{\frac{2}{B_i}}$$
 and $\delta_i = 1 - \frac{2D}{B_i}$.

3.3 Velocity and Acceleration

The peak-flux frequency versus time can be fitted using power-law models for both velocity and acceleration. The main results, where source location is taken into account, are presented in Figures 3.5, while the fit parameters are presented in Table 3.1.

An additional type III event is observed by the four spacecraft on the 21 July 2020 03:00 UT. Longitude of maximum directivity is estimated to be $\sim 150^{0}$ in the HEE coordinate system, in agreement with Musset et al. (2021). Regrettably, in this time-frame only STEREO-A is capturing spectral data with high enough time resolution to aid in the investigation. Results are shown in Figure 3.6.

Error due to frequency resolution and choice of density model is assumed to be negligible compared to uncertainty due to the temporal resolution of the instrument. Importantly, the density model used here is based on in situ solar wind observations and is treated as exact for simplicity, although in reality it may still introduce systematic and statistical offsets in the absolute values of derived parameters. In the case of PSP data, whenever half the width of the light curve at 90-95% of the peak exceeded instrumental time resolution, the former was taken as instrumental error,

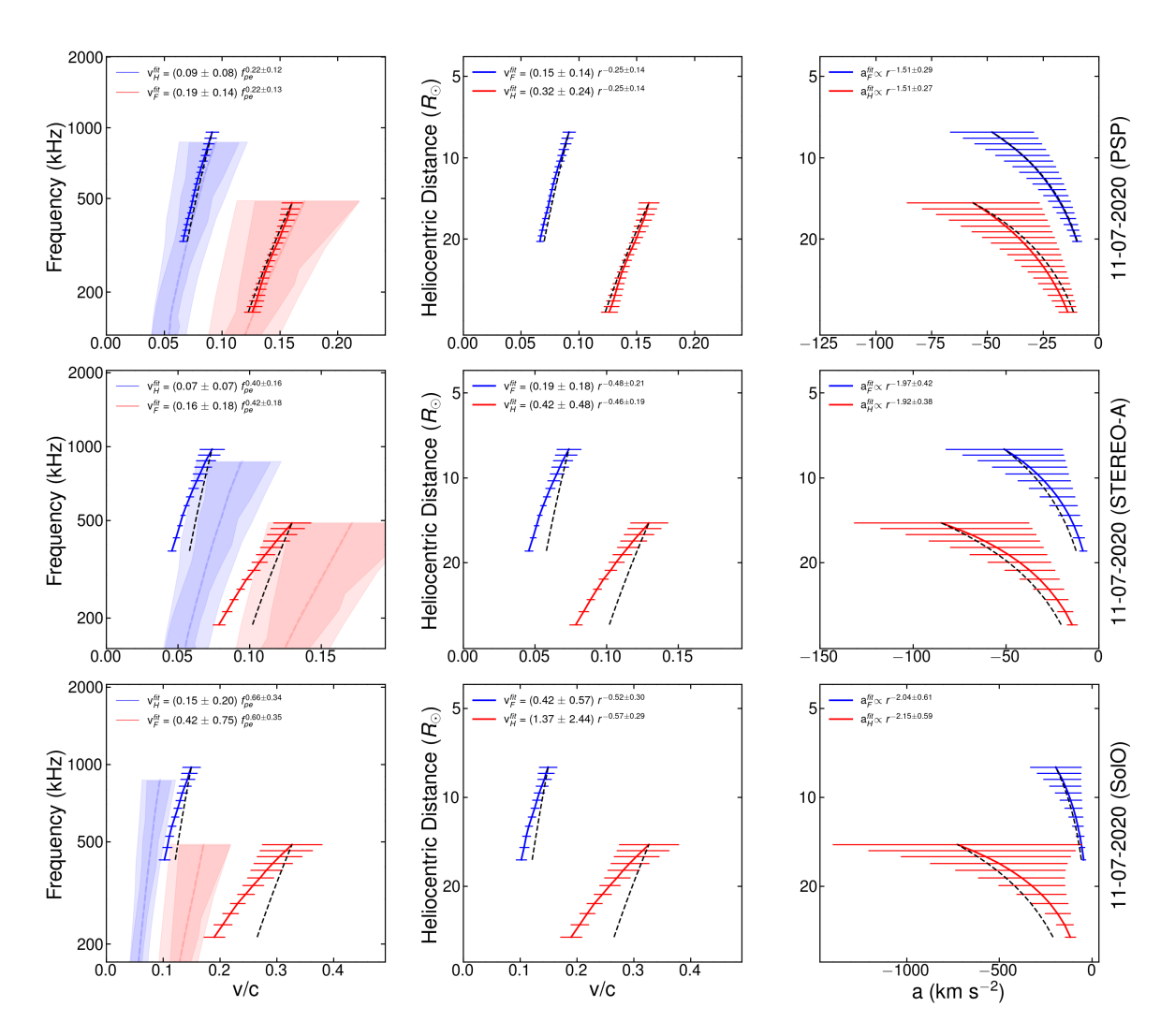


Figure 3.5: Exciter velocities and accelerations from the 11 July 2020 type III burst for the PSP, STEREO-A and SolO spacecraft (from top to bottom). Blue and red lines correspond, respectively, to the fundamental and harmonic components. Velocity as a function of frequency is shown on the left, where the shaded areas show velocities deduced from Krupar et al. (2015) using STEREO-A and STEREO-B data. Median values are shown with transparent solid (STEREO-A) and dashed (STEREO-B) lines. On the centre and right, velocity and acceleration of the exciter are plotted as a function of distance. Black dashed lines correspond to the result from Equation 3.20, where x_0 corresponds to the location where the highest analysed frequency is emitted.

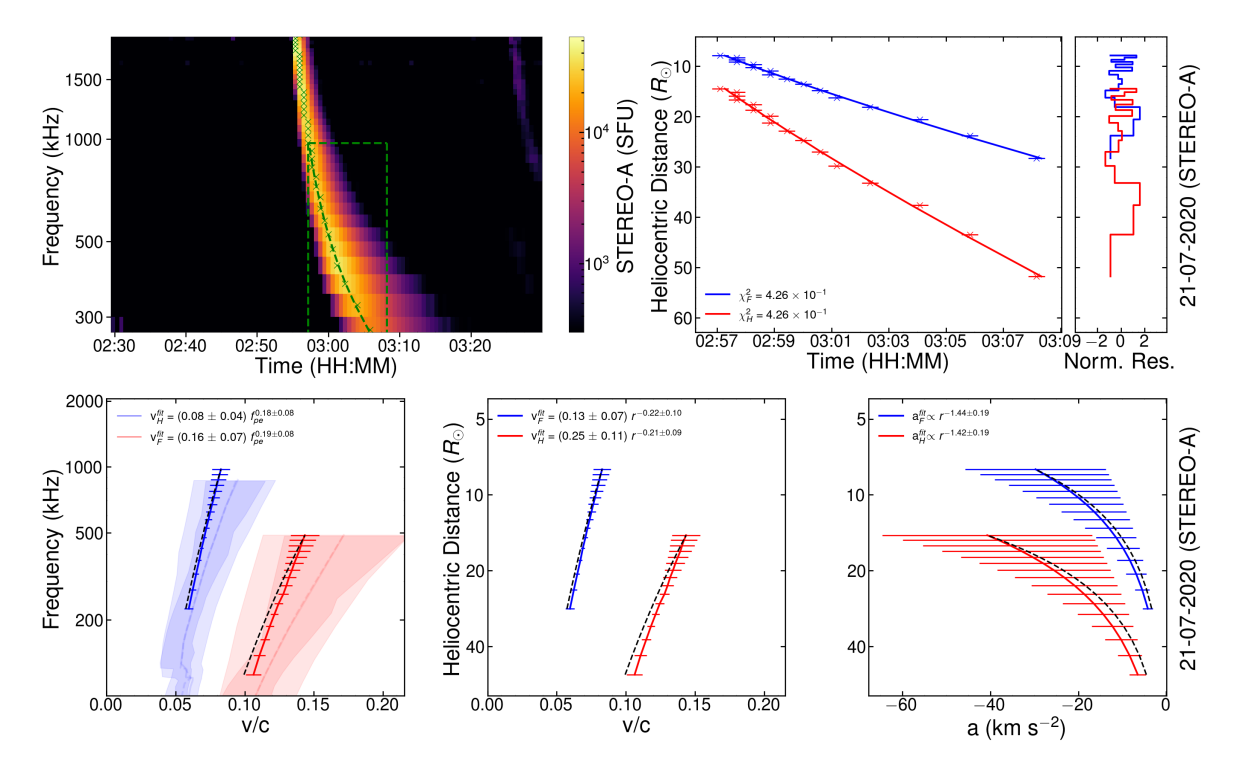


Figure 3.6: The same as Figure 3.1 (top) and Figure 3.5 (bottom), but for the 21 July 2020 event observed by the STEREO-A spacecraft.

allowing the uncertainty on radio flux peak time to be taken into account. Uncertainties in derived parameters were estimated using a Markov Chain Monte Carlo (MCMC) method (Press et al. 1986). The MCMC method consists in generating a number of parameter samples, with each new sample being generated based on the

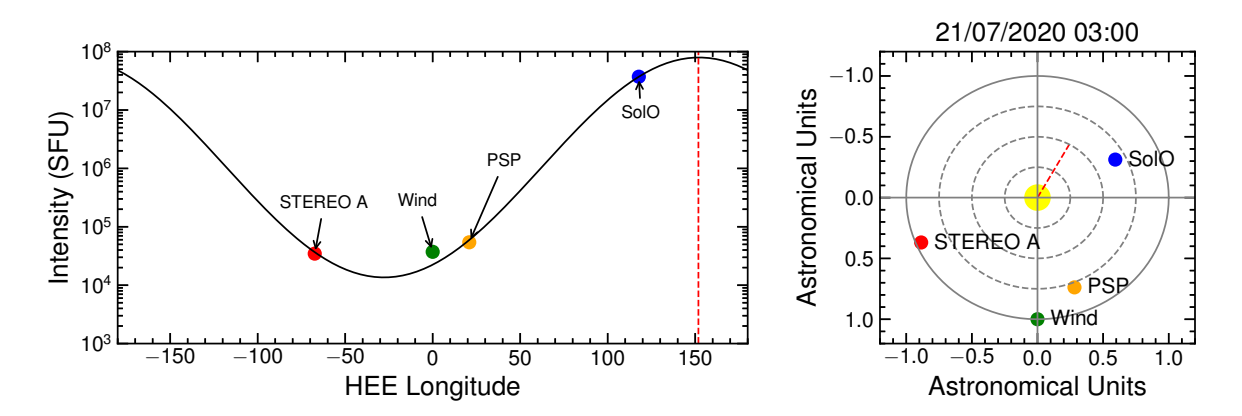


Figure 3.7: The same as Figure 3.2 but for the 21 July 2020 event observed by the STEREO-A spacecraft.

Table 3.1: Parameters A_i [MHz s^{-B}], B_i and t_{0i} [s] from Equation 3.4, where i = F, H depending on whether fundamental or harmonic emission is assumed.

Date	A_F	B_F	t_{0F}	A_H	B_H	t_{0H}	
PSP							
11/07/2020	93.3±59.2	-0.92 ± 0.09	720 ± 31	54.4 ± 54.7	-0.92 ± 0.12	719±36	
		ST	TEREO-A				
11/07/2020	54.4±54.7	-0.77±0.10	910±49	30.2±20.7	-0.78±0.09	897±47	
21/07/2020	133.3±60.1	-0.94 ± 0.08	1463 ± 34	75.7 ± 41.1	-0.95 ± 0.08	$1451{\pm}40$	
SolO							
11/07/2020	27.8±34.7	-0.76±0.14	680±28	11.2±17.7	0.74 ± 0.13	692±28	

previous one, and exploring the range of possible parameter values. A large number of samples produces reliable estimates of parameter uncertainties, with the standard deviation of a parameter calculated from the statistical spread of its sampled values (Figure 3.8).

The estimated velocities range from 0.04c at 375 kHz to 0.14c at 1 MHz, or from 0.10c at 185 kHz to 0.45c at 500 kHz, depending on whether fundamental or harmonic emission is considered, consistent with estimates from previous studies. Similarly, median values for β_i are found to be $\beta_F \sim \beta_H \sim$ -0.37 \pm 0.15, in agreement with $\beta_f \sim \beta_H \sim$ -0.35 from the power law model in Krupar et al. (2015).

Uncertainty in accelerations range between 20-70%, with exciter accelerations varying from -4 km s⁻² at 375 kHz to -194 km s⁻² at 1 MHz for fundamental emission. Accelerations for harmonic emission are up 4 times greater in magnitude, ranging from -6 km s⁻² at 185 kHz up to a minimum of -725 km s⁻² at 500 kHz. These estimates up an order of magnitude greater than values found by Krupar et al. (2015). Exciter accelerations are observed to decrease rapidly, with average values $\delta_F \approx \delta_H \approx -1.71 \pm 0.20$. As shown in Figure 3.9, the larger errors in velocity and accelerations derived using SolO data reflect the instruments slightly lower temporal resolution.

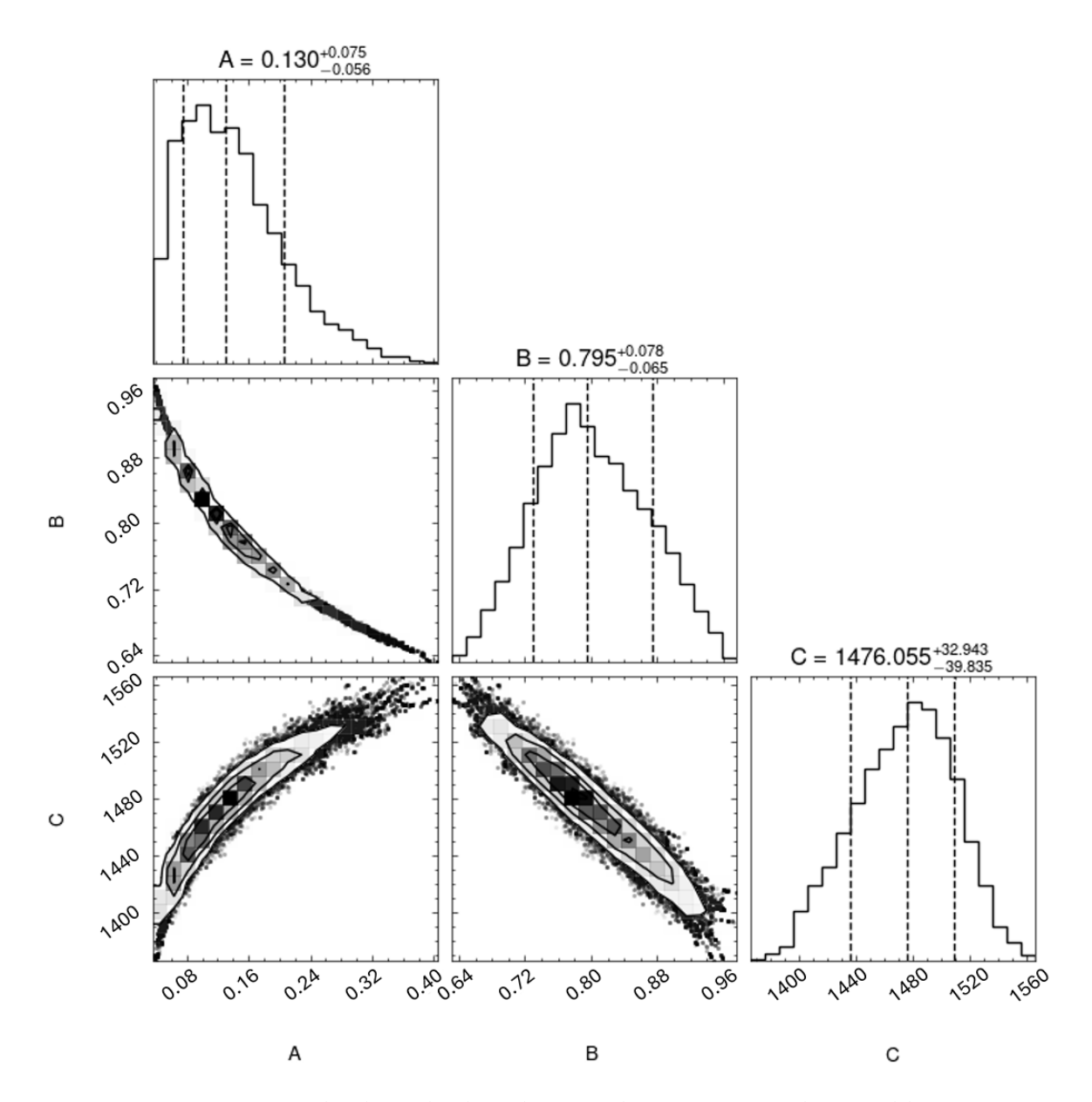


Figure 3.8: MCMC method applied to the 21 July 2020 event observed by STEREO-A. Spread in parameter space provides standard deviation for fitted parameters A, B and C (here denoting parameter t_0).

Table 3.2: Parameters α_i [s⁻¹] and β_i (top) from Equation 3.7, and γ_i [s⁻²] and δ_i (bottom) from Equation 3.8, where i = F, H depending on whether fundamental or harmonic emission is assumed.

Date	α_F	eta_F	α_H	β_H					
Dute	α _F		α_H	<i>Ρ</i> Η					
		PSP							
11/07/2020	0.15 ± 0.11	-0.25 ± 0.13	0.32 ± 0.32	-0.25 ± 0.15					
STEREO-A									
11/07/2020	0.19 ± 0.23	-0.48 ± 0.21	$0.42{\pm}0.46$	-0.46 ± 0.19					
21/07/2020	0.13 ± 0.05	-0.22 ± 0.10	$0.25{\pm}0.12$	-0.21 ± 0.11					
	SolO								
11/07/2020	$0.42{\pm}0.64$	-0.52 ± 0.27	1.37±2.71	-0.57 ± 0.33					
Date	$\gamma_F/10^4$	δ_F	$\gamma_H/10^4$	δ_H					
Date	$\gamma_F/10^4$	δ_F PSP	$\gamma_H/10^4$	δ_H					
Date 11/07/2020	$\gamma_F/10^4$ -0.07 ± 0.13		$\gamma_H/10^4$ -0.32 ± 0.78	δ_H -1.51 ± 0.31					
		PSP	-0.32 ± 0.78						
		PSP -1.51±0.26	-0.32 ± 0.78						
11/07/2020	-0.07 ± 0.13	PSP -1.51±0.26 STEREO-A	-0.32 ± 0.78	-1.51±0.31					
11/07/2020	-0.07 ± 0.13 -0.22 ± 0.58	PSP -1.51±0.26 STEREO-A -1.97±0.42	-0.32 ± 0.78 -1.02 ± 2.51	-1.51 ± 0.31 -1.92 ± 0.38					
11/07/2020	-0.07 ± 0.13 -0.22 ± 0.58	PSP -1.51±0.26 STEREO-A -1.97±0.42 -1.44±0.20	-0.32 ± 0.78 -1.02 ± 2.51	-1.51 ± 0.31 -1.92 ± 0.38					

3.4 Inhomogeneous Plasma and Electron Beam Deceleration

The Langmuir waves driven by an electron beam are strongly affected by density inhomogeneity. The solar corona and solar wind plasma is inhomogeneous due to the large scale density decrease with distance, and to smaller scale density fluctuations. Inhomogeneities at both scales will affect the Langmuir wave evolution via refraction and angular scattering. While angular scattering of Langmuir waves changes the direction of the wave-vector, refraction changes the wave-vector magnitude and hence the phase-speed. When the wavelength of a Langmuir wave λ is compared to the size of the plasma inhomogeneity (Vedenov et al. 1967; Coste et al. 1975), i.e.

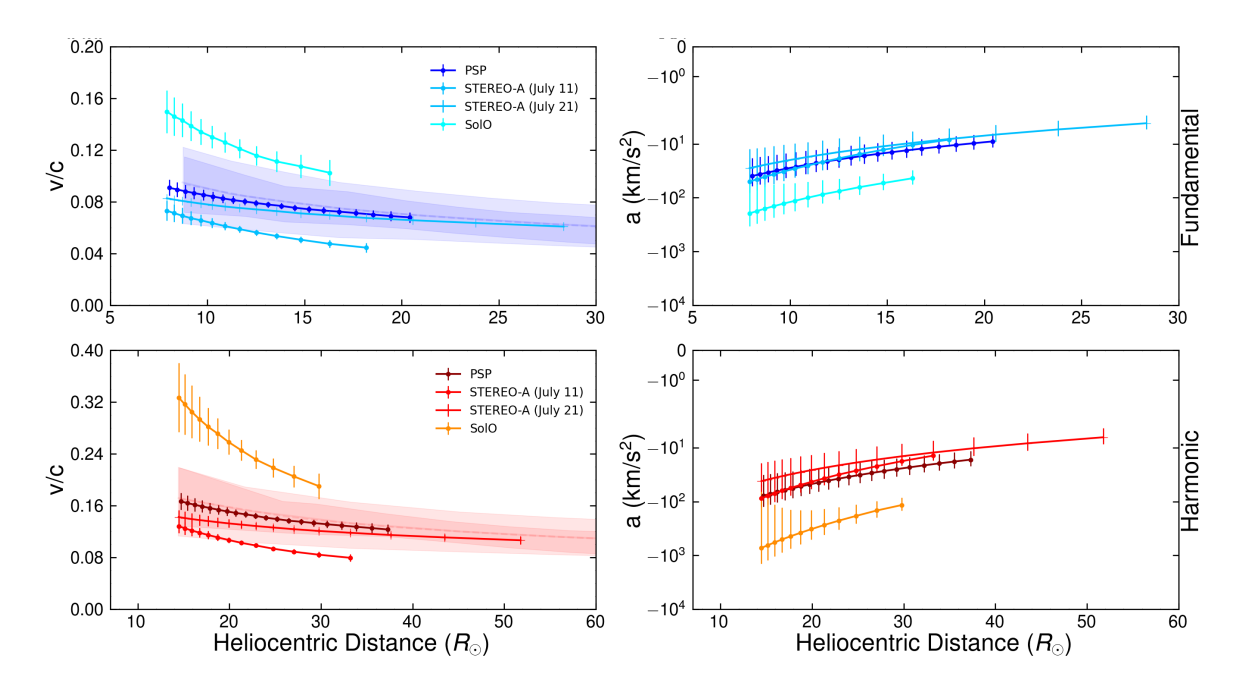


Figure 3.9: Velocities and accelerations deduced from PSP, STEREO-A and SolO data are represented by lines different color shades, with darker to lighter shades being associated to PSP, STEREO-A and SolO, respectively. Blue and red shades are associated to fundamental and harmonic emission, respectively. The top row displays fundamental emission, while the bottom row represents the harmonic component. The events of July 11, 2020, and July 21, 2020, are distinguished using dots and crosses as markers, respectively. Shaded regions represent the results from the Krupar et al. (2015) analysis, with median values showcased by the transparent solid (STEREO-A) and dashed (STEREO-B) lines.

 $\lambda \ll L$, where

$$L \equiv \left(\frac{1}{\omega_{pe}} \frac{\partial \omega_{pe}}{\partial x}\right)^{-1} = \left(\frac{\partial \ln \omega_{pe}}{\partial x}\right)^{-1},\tag{3.9}$$

is the scale of ambient plasma density fluctuations, the resonant interaction between the electron distribution function f(v,x,t) and the spectral energy density of Langmuir waves W(v,x,t) can be described through a system of kinetic equations (e.g. Ryutov 1969; Kontar 2001b; Ratcliffe et al. 2014)

$$\frac{\partial f}{\partial t} + v \frac{\partial f}{\partial x} = \frac{4\pi^2 e^2}{m^2} \frac{\partial}{\partial v} \frac{W}{v} \frac{\partial f}{\partial v} = \frac{\partial}{\partial v} D \frac{\partial f}{\partial v}$$
(3.10)

$$\frac{\partial W}{\partial t} + v_{gr} \frac{\partial W}{\partial x} - \frac{v^2}{L} \frac{\partial W}{\partial v} = \frac{\pi \omega_{pe}}{n_e} v^2 W \frac{\partial f}{\partial v}.$$
 (3.11)

Similarly to section 2.1, $\int W dk = U$ and $\int f dv = n_b$ are the energy density of Langmuir waves and the number density of the electron beam, while spontaneous thermal level Langmuir wave terms are disregarded. The last two terms on the left hand side of Equation (3.11) describe the propagation of Langmuir waves with group velocity $v_{\rm gr} << v$ and refraction of wavenumber k. The wave-number increases (phase speed decreases) when Langmuir waves propagate into a region of decreasing plasma density (Vedenov et al. 1967; Ryutov 1969). The right hand side terms of Equations (3.10,3.11) describe the dominant resonant interaction $\omega_{pe} \sim kv$ between electrons with speed v and plasma waves with wavenumber k. The $0^{\rm th}$ -order solution is well known to be a plateau in the velocity space (see Equations (2.6),(2.7) from Section 2.1).

From Equations (2.13-2.15), the momentum density of the electron beam is the integral of the electron distribution function over velocity

$$P_{b}(x,t) = \int_{0}^{u(x,t)} m_{e}vp(x,t) \, dv = m_{e}n(x,t) \frac{u(x,t)}{2}, \qquad (3.12)$$

and the momentum density of the Langmuir waves is the integral of the spectral energy density of Langmuir waves multiplied by $k\sim \omega_{pe}/v$ over velocity

$$P_{\mathbf{w}}(x,t) = \omega_{pe} \int_{0}^{u(x,t)} \frac{W_{0}(v,x,t)}{v^{3}} dv = m_{e} \frac{n(x,t)}{u(x,t)} \int_{0}^{u(x,t)} v\left(1 - \frac{v}{u(x,t)}\right) dv =$$

$$= m_{e} n(x,t) \frac{u(x,t)}{6},$$
(3.13)

where Equation (2.15) for $W_0(v, x, t)$ was used. The total momentum density of electrons and Langmuir waves is the sum of Equations (3.12) and (3.13):

$$P_{\text{tot}}(x,t) = P_{\text{b}}(x,t) + P_{\text{w}}(x,t) = m_{e}n(x,t)\frac{u(x,t)}{2} + m_{e}n(x,t)\frac{u(x,t)}{6} =$$

$$= m_{e}n(x,t)\frac{2u(x,t)}{3} = 4P_{\text{w}}.$$
(3.14)

In a homogeneous plasma, the total momentum density $P_{\text{tot}} = P_b + P_w$ is conserved (Mel'nik et al. 1999). In an inhomogeneous plasma, the situation is more complicated. The numerical simulations by Kontar (2001b), Reid and Kontar (2013) and Ratcliffe et al. (2014) show that, as the Langmuir waves propagate through a region of decreasing background plasma density, they experience a negative shift in velocity space towards smaller thermal speeds. This results in wave-absorption (Landau damping) by the Maxwellian component of the plasma and a decrease in the total energy of the beam-wave structure. At the same time, the total momentum of the plateau P_b is constant over the timescale of the shift in wave velocity, i.e. $\frac{\partial}{\partial t}P_b=0$ over the timescale of refraction. The time evolution of the electron distribution and Langmuir waves can be seen in the Figure 1 by Kontar (2001b).

Since the group speed of Langmuir waves $v_{gr} \ll v_{T_e}$, where v_{T_e} is the electron thermal velocity, the spatial motion of Langmuir waves can be ignored. Considering only the effect of the refraction and assuming electrons have a plateau distribution, i.e. $\partial f/\partial v = 0$, Equation (3.11) can be simplified as

$$\frac{\partial W}{\partial t} - \frac{v^2}{L} \frac{\partial W}{\partial v} = 0, \qquad (3.15)$$

where L is the scale of ambient plasma density fluctuations defined by Equation (3.9). Multiplying Equation (3.15) by ω_{pe}/v^3 and integrating over velocity from 0 to u yields

$$\frac{\partial}{\partial t} \int_0^u \frac{\omega_{pe}}{v^3} W(v) dv - \int_0^u \frac{v^2 \omega_{pe}}{L v^3} \frac{\partial}{\partial v} W(v) dv = 0, \qquad (3.16)$$

which reduces to

$$\frac{\partial}{\partial t}P_W = \frac{m_e n u^2}{12L} = \frac{u}{2L}P_W. \tag{3.17}$$

The equation shows that the momentum density of Langmuir waves decreases due to the interaction with density inhomogeneities in the background plasma, when L < 0, i.e. decreasing density. For L > 0, i.e. increasing density, the Langmuir waves increase velocity and can accelerate electrons (see Figure 2 by Kontar (2001b)).

The total momentum of the electron beam can be taken to be constant over the timescale of the shift in wave velocity, i.e. $\frac{\partial}{\partial t}P_b=0$. Thus, the total momentum density of electrons and Langmuir waves changes as

$$\frac{\partial}{\partial t}P_{\text{tot}} = \frac{\partial}{\partial t}P_W + \frac{\partial}{\partial t}P_b = \frac{u}{2L}P_W + 0 = \frac{u}{2L}\frac{P_{\text{tot}}}{4}.$$
 (3.18)

i.e. the total momentum decreases due to the decrease in Langmuir wave momentum density. Recalling the expression for the total momentum density $P_{\text{tot}} = m_e n \frac{2u}{3}$, for constant n moving with slowly changing speed u, Equation (3.18) can be simplified as

$$\frac{\partial u}{\partial t} \simeq u \frac{\partial u}{\partial x} = \frac{u}{4L} \,, \tag{3.19}$$

which can be integrated with $L = \left(\frac{1}{\omega_{pe}} \frac{\partial \omega_{pe}}{\partial x}\right)^{-1}$ to give the solution for the velocity of the beam plateau as a function of distance.

$$\frac{u(x)}{u(x=x_0)} = \left(\frac{\omega_{pe}(x)}{\omega_{pe}(x=x_0)}\right)^{1/4} = \left(\frac{f_{pe}(x)}{f_{pe}(x=x_0)}\right)^{1/4}.$$
 (3.20)

While simple and approximate, Equation (3.20) provides important insight into the decrease of the electron speed due to decreasing density. It shows that the decrease is faster for a steeper negative plasma density gradient. In solar wind with density $n(r) \propto r^{-2.3}$, the velocity decreases as $u(r) \propto r^{-0.29}$ and acceleration changes as $a(r) \propto r^{-1.58}$. Importantly, the model yields the proportionality $u \propto f^{0.25}$, which is independent of the density model. Interestingly, the acceleration a(r) is a rather steep function of r, $a(r) \propto r^{-1.58}$, so the measured acceleration could differ by an order of magnitude for different frequencies and is, in general, more sensitive to the density model. The velocity decrease is similar to the numerical simulations (Kontar 2001a; Reid and Kontar 2013; Lorfing and Reid 2023) of beam transport.

The comparison to velocity and acceleration estimations from type III events analyzed in the previous section can be seen in Figure 3.5, where Equation (3.20) is over plotted on the observational results as a dashed black curve. Note the spread of the initial speed and accelerations, with similar r dependency. While the beam deceleration model is in good agreement with the observations, with predicted velocities and accelerations falling within the margins of uncertainty for the observed $v \propto f_{pe}^{0.32\pm0.12}$

and $a(r) \propto r^{-1.71\pm0.20}$, note the differences in values of speed/acceleration obtained by different spacecraft. The discrepancy may arise from assumptions on the electron density model, as well as additional collisional losses for both electrons and plasma waves. It's also important to note that scattering strongly depends on the plasma conditions along the line of sight, which may vary significantly between spacecraft. The uncertainties comparable to the differences do not allow firm conclusion, but it is tempting to suggest that the delay δt is influenced by the scattering effects (Kontar et al. 2023), so the radio-waves are propagating slower than c.

3.5 Summary

The chapter examines the drift rates of four type III radio bursts originating from flares, taking angular positions of the bursts into account. For the first time, simultaneous four-spacecraft observation allow inferred velocities and accelerations of type III emitters to be corrected for source-spacecraft angle. Exciter velocities are found to increase with frequency as $u(f) \propto f^{0.32\pm0.12}$, regardless of whether harmonic or fundamental emission is assumed; this is within the uncertainties to the case of a beam deceleration propagating through background plasma of decreasing density that gives speed $u(f) \propto f^{0.25}$.

Assuming the density model in Equation 3.5, velocities are found to decrease with distance for all 4 events analyzed, with median $\beta_H \sim \beta_F \sim -0.37 \pm 0.15$, values consistent with previous results published by Krupar et al. (2015). Furthermore, exciter accelerations are predicted to decrease faster with heliocentric distance as $a(r) \propto r^{-1.58}$, in quite remarkable agreement with the observed $a(r) \propto r^{-1.71\pm0.20}$.

This result provides strong evidence for the interaction between beam-plasma structure and density inhomogeneity being being the primary driver of Type III solar radio burst exciter deceleration. It also lays a solid foundation for future work, which will likely involve statistical analysis to reduce the uncertainties.

Note that there are intriguing differences in the drift-rate of the same type III bursts observed by different spacecraft. The drift-rate analysis for the 11 July 2020 event using dynamic spectra from PSP, STEREO-A and SolO spacecraft show difference in velocities recorded by different spacecraft (Figure 3.9). Although the differences are only slightly exceed the uncertainties, this discrepancy, not attributed to properties intrinsic to the exciter, could be the result of radio waves scattering off density inhomogeneities in the ambient plasma and affecting the type III burst observed time characteristics (Kontar et al. 2023).

Chapter 4

Plasma motions and compressive wave energetics in the solar corona

4.1 Introduction

This chapter is based on the work by Azzollini et al. (2024), with the author of this thesis as first author. Section 4.2 was jointly written by Eduard P. Kontar and the author of this thesis. The author of this thesis' main contributions consist in section 4.3.1-4.3.3, as well as Appendices A and B. Figures and frequency broadening observations, as well as Section 4.5 are the work of Daniel L. Clarkson. Section 4.4 results from the collaboration (both in concepts and writing up) of Gordon A. Emslie and Eduard P. Kontar. Section 4.6 was a late addition, from the brilliant input of Eduard P. Kontar.

4.1. Introduction 87

As discussed in section 1.7.3, extrasolar sources are also affected by density turbulence and the same kinetic approach can be employed to model the propagation of both solar and extrasolar radio emission. Since the phase speed of density fluctuations are much less than the speed of radio waves, scattering is often treated as elastic, resulting primarily in angular broadening of extra-solar point sources (Machin and Smith 1952; Hewish 1958; Blesing and Dennison 1972; Anantharamaiah et al. 1994; Ingale et al. 2015).

However, as explored in this chapter, collective Compton scattering from electron density fluctuations (e.g., Akhiezer et al. 1958; Dougherty and Farley 1960) that are moving or oscillating perpendicular to the direction of wave propagation can lead to an *inelastic* change in the wavenumber and hence frequency broadening (that is normally a small fraction of the observed frequency). Doppler broadening of radio waves from spacecraft has been extensively studied to diagnose expansion of the solar wind (e.g., Woo 1978), and moving density irregularities have also been analyzed via observations of interplanetary scintillations. Woo and Gazis (1993) report the detection of solar wind structure between 0.08 and 0.53 AU, Woo (1996) report the first measurements of fine-scale structure within coronal streamers, as well as evidence for structure in solar wind speed in the inner corona, Mejia-Ambriz et al. (2015) use interplanetary scintillation observations to probe solar wind speeds in the inner heliosphere. They determine wind speed to vary between ~100-700 km/s, with the variations driven by transient events.

The spectral width of the radio-wave signal, or the strength of scintillation, is proportional to the speed of the density irregularity weighted by the amplitude of the density fluctuation. Using multiple receivers to observe interplanetary scintillation, Ekers and Little (1971) found a random velocity component of $v \simeq (100\text{-}200) \text{ km s}^{-1}$ at $(5\text{-}10) R_{\odot}$ and less than 50 km s^{-1} at $40 R_{\odot}$. Somewhat lower fractional velocities

4.1. Introduction 88

 $\delta v/v \simeq 0.25$ of the solar wind speed were deduced by Armstrong and Coles (1972). Armstrong et al. (1986) reported a random velocity component at $< 12\,R_\odot$ that was comparable to the bulk flow speed. Assuming a density model of the corona and the fractional amplitude of density fluctuations, Wexler et al. (2020) used spacecraft carrier frequency fluctuations to infer the flow velocity profile in the middle corona (West et al. 2023).

This chapter employs a recently-developed anisotropic density turbulence model (Kontar et al. 2023) to analyze a large observational dataset of Doppler broadening of spacecraft carrier frequencies and thus determine the speeds of density fluctuations in the space between the Sun and 1 au. The spectral broadening is discussed in terms of solar wind flows, compressive waves, and random plasma motions. By matching observations, we determine the characteristic velocities of density fluctuations and we show how the wavevector anisotropy, $\alpha = q_{\parallel}/q_{\perp}$, associated with density fluctuations along versus perpendicular to the solar radius vector, affects these results. The average frequency broadening at >10 R_{\odot} is found, in line with the previous works, to be determined mostly by the radial solar wind speed, while closer to the Sun (<10 R_{\odot}), both transverse and radial motions could contribute. Due to the wavenumber anisotropy in the density fluctuations, which are typically elongated along the radial direction (α < 1), smaller perpendicular velocities are needed to explain a given amount of frequency broadening. For example, if $\alpha = 0.25$, either radial speeds $\simeq 160 \ \mathrm{km \ s^{-1}}$ or transverse speeds $\simeq 40 \ \mathrm{km \ s^{-1}}$ are consistent with the observed amount of frequency broadening.

4.2 Static density fluctuations and angular broadening

Density fluctuations with wavevector \mathbf{q} are characterized by their three-dimensional wavevector spectrum $S(\mathbf{q})$, typically normalized (see, e.g., Kontar et al. 2023) by the rms level of fluctuations in the local density n (cm⁻³):

$$\int S(\mathbf{q}) \frac{d^3 q}{(2\pi)^3} = \frac{\langle \delta n^2 \rangle}{n^2} \equiv \epsilon^2 . \tag{4.1}$$

Following previous studies (e.g., Arzner and Magun 1999; Bian et al. 2019; Kontar et al. 2019), the diffusion tensor describing elastic scattering of radio waves with wavevector $\mathbf{k}(\mathbf{v}_g,\omega)$ in a medium containing static density fluctuations can be written as

$$D_{ij} = \frac{\pi \omega_{pe}^4}{4 \omega^2} \int q_i q_j S(\mathbf{q}) \, \delta\left(\mathbf{q} \cdot \mathbf{v}_g\right) \, \frac{d^3 q}{(2\pi)^3} , \qquad (4.2)$$

where q_i,q_j (cm⁻¹) are the components of the density fluctuation wavevector in the directions labeled by the suffixes i,j, the wave group velocity $\mathbf{v}_g = \partial \omega/\partial \mathbf{k}$ and $\omega(\mathbf{k}) = (\omega_{pe}^2 + c^2 \, k^2)^{1/2}$ is the angular frequency of electromagnetic waves with wavevector \mathbf{k} in a plasma with local plasma frequency $\omega_{pe}(\mathbf{r})$.

Similar to Kontar et al. (2023), we take the spectrum of density turbulence to be anisotropic with a constant anisotropy factor α , so that

$$S(\mathbf{q}) = S(\tilde{q}), \text{ where } \tilde{q} = \sqrt{\frac{q_{\parallel}^2}{\alpha^2} + q_{\perp_2}^2 + q_{\perp_1}^2},$$
 (4.3)

which has axial symmetry around the \parallel direction, i.e., along the magnetic field **B** (see Figure 4.1), and is isotropic with respect to the $\tilde{\bf q}$ basis, i.e. the coordinate system is isotropic in $\tilde{\bf q}$ space. In matrix form, $\tilde{\bf q}={\bf A}{\bf q}=(\alpha^{-1}q_{\parallel},q_{\perp_2},q_{\perp_1})$, where ${\bf A}$ is the anisotropy matrix

$$\mathbf{A} = \begin{pmatrix} \alpha^{-1} & 0 & 0 \\ 0 & 1 & 0 \\ 0 & 0 & 1 \end{pmatrix} . \tag{4.4}$$

The quantity α appearing in Equations (4.3) and (4.4) quantifies the degree of anisotropy in the turbulence distribution: $\alpha < 1$ corresponds to density fluctuations elongated along the magnetic field $(q_{\parallel}^{-1} > q_{\perp}^{-1}$, i.e., $q_{\parallel} < q_{\perp})$, as is often observed in the solar wind (e.g., Celnikier et al. 1987; Musset et al. 2021).

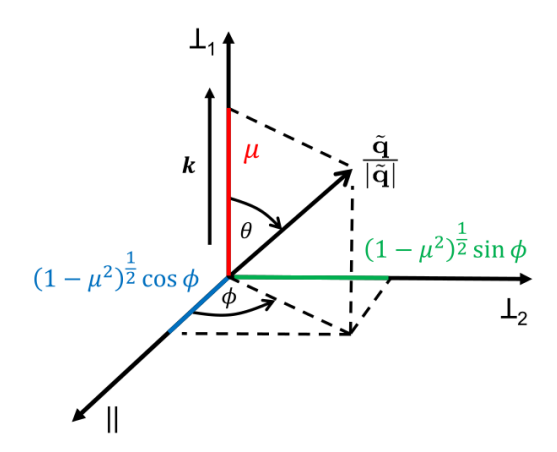


Figure 4.1: Wavevector coordinate system used in our analysis; the radio wave, with wavevector \mathbf{k} , is propagating along the \perp_1 direction.

Figure 4.1 shows the wavevector coordinate system used for our analysis; it is a polar system in $\tilde{\bf q}$ space (in which the density fluctuation spectrum $S(\tilde{\bf q})$ is isotropic: $S(\tilde{\bf q})\equiv S(q)$). The polar axis is aligned with the \bot_1 direction, which is along the direction of ${\bf k}$ and ${\bf v}_g$ (Figure 4.1). The direction cosine $\mu=\cos\theta$, where θ is the polar angle from the \bot_1 axis, while the azimuthal angle ϕ measures the angle from the \parallel direction in the $(\tilde{q}_{\parallel},\tilde{q}_{\perp 2})$ plane. Thus $\tilde{q}_{\perp 1}=\tilde{q}\,\mu$, $\tilde{q}_{\perp 2}=\tilde{q}\,(1-\mu^2)^{1/2}\sin\phi$ and $\tilde{q}_{\parallel}=\tilde{q}\,(1-\mu^2)^{1/2}\cos\phi$. Changing variables from ${\bf q}=(q_{\parallel},q_{\perp 2},q_{\perp 1})$ to $\tilde{\bf q}={\bf A}\,{\bf q}=$

 $(\alpha^{-1}q_{\parallel},q_{\perp_2},q_{\perp_1})$, Equation (4.2) can be written as

$$D_{ij} = \frac{\pi \omega_{pe}^{4}}{4 \omega^{2}} \int q_{i} q_{j} S(\mathbf{q}) \, \delta\left(\mathbf{q} \cdot \mathbf{v}_{g}\right) \, \frac{d^{3}q}{(2\pi)^{3}} =$$

$$= \frac{\pi \omega_{pe}^{4}}{4 \omega^{2}} \, \alpha \, A_{i\alpha}^{-1} A_{j\beta}^{-1} \int \tilde{q}_{\alpha} \, \tilde{q}_{\beta} \, S(\tilde{\mathbf{q}}) \, \delta\left(\tilde{\mathbf{q}} \cdot \tilde{\mathbf{v}}_{\mathbf{g}}\right) \, \frac{d^{3}\tilde{q}}{(2\pi)^{3}} , \qquad (4.5)$$

where $\tilde{\mathbf{v}} = (\alpha v_{\parallel}, v_{\perp_2}, v_{\perp_1})$ and we have used the determinant of the Jacobian $\det(\mathbf{J}) = \det(\mathbf{A}^{-1}) = \alpha$.

For elastic scattering and a radio wave propagating along the \perp_1 direction, Equation (4.5) can be used to find the components of the diffusion tensor

$$\mathbf{D} = \frac{\pi \omega_{pe}^4}{16 \,\omega^2 \,c} \overline{q \,\epsilon^2} \begin{pmatrix} \alpha^2 & 0 & 0 \\ 0 & 1 & 0 \\ 0 & 0 & 0 \end{pmatrix} \equiv \frac{\pi \omega_{pe}^4}{16 \,\omega^2 \,c} \, \overline{q \,\epsilon^2} \, \operatorname{diag} \left(\alpha^2, 1, 0\right) , \qquad (4.6)$$

where we have introduced the spectrum-weighted mean wavenumber $\overline{q} \, \epsilon^2$ (defined as in Kontar et al. 2023),

$$\overline{q \, \epsilon^2} = \int q \, S(q) \, \frac{d^3 q}{(2\pi)^3} = \alpha \int \tilde{q} \, S(\tilde{q}) \, \frac{d^3 \tilde{q}}{(2\pi)^3} = \alpha \, \frac{4\pi}{(2\pi)^3} \, \int \tilde{q}^3 \, S(\tilde{q}) \, d\tilde{q} \quad , \tag{4.7}$$

so that there are only two non-zero elements, neither of which contributes to frequency broadening. These results recover the expressions obtained by Kontar et al. (2019).

For a radio wave propagating with $\mathbf{v}_g \simeq c \, \mathbf{k}/|\mathbf{k}|$ along the \perp_1 -direction (see Figure 4.1), we can find the components of the diffusion tensor elements, viz. (Equation (4.6))

$$\mathbf{D} = \frac{\pi \omega_{pe}^4}{16 \,\omega^2 c} \, \overline{q \,\epsilon^2} \left(\begin{array}{ccc} \alpha^2 & 0 & 0 \\ 0 & 1 & 0 \\ 0 & 0 & 0 \end{array} \right) \ , \tag{4.8}$$

where in the second equality, we have transformed from the q basis to the \tilde{q} basis, in which the wavenumber spectrum is isotropic.

The diffusion tensor D given by Equation (4.8) has two non-zero elements that determine the scattering rates $d\langle\Delta k_{\parallel}^2\rangle/dt$ and $d\langle\Delta k_{\perp_2}^2\rangle/dt$. The \perp_2 and \parallel directions are perpendicular to the wave propagation vector \mathbf{k} (see Figure 4.1). For $\Delta\mathbf{k}\perp\mathbf{k}$, the scattering corresponding to terms $d\langle\Delta k_{\parallel}^2\rangle/dt$ and $d\langle\Delta k_{\perp_2}^2\rangle/dt$ is elastic: $|\mathbf{k}+\Delta\mathbf{k}|^2\simeq |\mathbf{k}|^2+2\mathbf{k}\cdot\Delta\mathbf{k}=|\mathbf{k}|^2$, i.e., $|\mathbf{k}|$ is a constant. To change the absolute value of $|\mathbf{k}|$, or equivalently the wave frequency $\omega(\mathbf{k})\simeq c|\mathbf{k}|$, we must have non-zero $\mathbf{k}\cdot\Delta\mathbf{k}$, i.e. $d\langle\Delta k_{\perp_1}^2\rangle/dt\neq 0$. The effects of such inelastic scatterings, which are important for frequency broadening, are next considered.

4.3 Inelastic scattering of radio waves

When the density fluctuations are not static, but are instead due to either waves or density fluctuations advected by plasma motions, the scattering could be inherently inelastic with $d\langle\Delta k_{\perp_1}^2\rangle/dt\neq 0$, so that $|\mathbf{k}|\neq \mathrm{const}$, leading to a change in the wave frequency ω . Consider an electromagnetic (EM) wave with frequency $\omega(\mathbf{k})$ and wavevector \mathbf{k} that is scattered by a density fluctuation with wavenumber \mathbf{q} and fre-

quency $\Omega(\mathbf{q})$, resulting in a scattered EM wave with frequency $\omega(\mathbf{k}')$ and wavevector \mathbf{k}' . Momentum and energy conservation in such a three-wave process (Tsytovich 1995) demands that

$$\mathbf{k} + \mathbf{q} = \mathbf{k}', \quad \omega(\mathbf{k}) + \Omega(\mathbf{q}) = \omega(\mathbf{k}') .$$
 (4.9)

Using the dispersion relation for electromagnetic waves $\omega^2(\mathbf{k}) = \omega_{pe}^2 + c^2 k^2$ and using the resonance condition $\Omega(\mathbf{q}) = \mathbf{v} \cdot \mathbf{q}$ as a dispersion relation, one finds that, for $\omega \gg \omega_{pe}$, $|\mathbf{k}| \gg |\mathbf{q}|$, and $|\mathbf{k}'| \gg |\mathbf{q}|$,

$$\mathbf{q} \cdot \frac{\mathbf{k}}{|\mathbf{k}|} \simeq \frac{\Omega(\mathbf{q})}{c} = \frac{\mathbf{q} \cdot \mathbf{v}}{c}$$
 (4.10)

Hence to satisfy the conservation of energy and momentum relations (4.9), the density wavevector q should be quasi-perpendicular to k:

$$\frac{q_{\parallel \mathbf{k}}}{q_{\perp \mathbf{k}}} \left(1 - \frac{v_{\parallel \mathbf{k}}}{c} \right) \simeq \frac{v_{\perp \mathbf{k}}}{c} \simeq \frac{q_{\parallel \mathbf{k}}}{q_{\perp \mathbf{k}}} \ll 1 , \qquad (4.11)$$

showing that density fluctuations involving motions perpendicular to \mathbf{k} ($v_{\perp \mathbf{k}} \neq 0$) produce a shift in the magnitude $|\mathbf{k}|$ of the electromagnetic wavevector and hence in the frequency of the electromagnetic wave. In contrast, note that if we take $\mathbf{v} \parallel \mathbf{k}$ we arrive to the result $v_{\parallel \mathbf{k}} \simeq c$, stressing that momentum and energy conservation require $v_{\perp \mathbf{k}} \neq 0$.

4.3.1 Parallel propagating density fluctuations

The generalization of Equation (4.2) in the presence of non-static density fluctuations is

$$D_{ij} = \frac{\pi \omega_{pe}^4}{4 \omega^2} \int q_i q_j S(\mathbf{q}) \, \delta \left(\Omega(\mathbf{q}) - \mathbf{q} \cdot \mathbf{v}_g \right) \, \frac{d^3 q}{(2\pi)^3} , \qquad (4.12)$$

where $\Omega(\mathbf{q})$ is the dispersion relation for the density fluctuations, which is conceptually identical to plasma wave scattering on plasma density fluctuations (Sagdeev and Galeev 1969; Goldman and Dubois 1982; Ratcliffe et al. 2012).

We first consider density fluctuations moving along the radial direction \mathbf{B} , i.e., $\Omega(\mathbf{q}) = v_{\parallel} q_{\parallel}$. In this case, the change of frequency (or absolute value of the wavevector of the radio wave) is due to non-zero values of v_{\parallel} . One can include the effects of the moving waves in the calculation of the components D_{ij} of the diffusion tensor that affects both the direction of propagation (angular broadening) and change in wavenumber (frequency broadening). As shown in Equation (9) in Appendix A.1, the modified diffusion tensor takes the form

$$\mathbf{D} = \frac{\pi \omega_{pe}^4}{16 \,\omega^2 \,c} \,\overline{q \,\epsilon^2} \begin{pmatrix} \alpha^2 & 0 & 0 \\ 0 & 1 & 0 \\ 0 & 0 & \frac{\alpha^2 v_{\parallel}^2}{c^2} \end{pmatrix} . \tag{4.13}$$

Naturally, Equation (4.13) reduces to Equation (4.8) when $v_{\parallel} \rightarrow 0$.

4.3.2 Transverse density fluctuations

We can similarly evaluate the diffusion tensor components D_{ij} for the case of waves moving in the perpendicular (transverse) direction, with assumed dispersion relation $\Omega(\mathbf{q}) = v_{\perp_2} q_{\perp_2}$. Substituting this into Equation (4.12) gives the form of the diffusion tensor (see Equation (14) in Appendix A.2)

$$\mathbf{D} = \frac{\pi \omega_{pe}^4}{16 \,\omega^2 \,c} \,\overline{q \,\epsilon^2} \begin{pmatrix} \alpha^2 & 0 & 0 \\ 0 & 1 & 0 \\ 0 & 0 & \frac{v_{\perp 2}^2}{c^2} \end{pmatrix} , \qquad (4.14)$$

Equations (4.13) and (4.14) show that all motions in the plane of the sky, i.e., perpendicular to the radio wave propagation direction, lead to a change in the absolute magnitude of the radio-wave wavenumber. If there are waves in both the parallel (\parallel) and perpendicular (\perp_2) directions, the diffusion effects simply add together:

$$\mathbf{D} = \frac{\pi \omega_{pe}^4}{16 \,\omega^2 \,c} \,\overline{q \,\epsilon^2} \begin{pmatrix} \alpha^2 & 0 & 0 \\ 0 & 1 & 0 \\ 0 & 0 & \frac{\alpha^2 v_{\parallel}^2 + v_{\perp 2}^2}{c^2} \end{pmatrix} . \tag{4.15}$$

We note that since $\alpha < 1$ perpendicular motions are more effective at frequency broadening than radial (parallel) motions.

4.3.3 Random (turbulent) motions

The inferred turbulent velocities are dependent on the assumed ion temperature (Seely et al. 1997). Measurement of the width of spectral lines in the radio domain also provide a (temperature-independent) measure of velocity fluctuations.

Observation of solar corona UV spectral lines often show significant broadening in excess of the thermal width. Such non-thermal broadening of lines is normally interpreted as the unresolved motion of emitting ions: either fluid motions (unresolved flows or waves) or motion of accelerated non-thermal ions (e.g. Jeffrey et al. 2014). Excess width of EUV coronal spectral lines (compared to their thermal width) is often interpreted as evidence of perpendicular velocity fluctuations at speeds of a few tenths of the Alfvén speed (e.g., Doyle et al. 1998; Singh et al. 2011). Alfvén waves are the likely culprit for this phenomenon (Hassler et al. 1990; Chandrasekhar et al. 1991), with Banerjee et al. (1998), Doyle et al. (1998, 1999), Banerjee et al. (2009), Landi and Cranmer (2009) and Singh et al. (2011) finding non-thermal velocities

in agreement with undamped, radially propagating Alfvén waves. The non-thermal velocities are dependent on the assumed ion temperature (Seely et al. 1997), and are determined from the width ζ of the spectrum line profile, measured at the 1/e level. The standard deviation is retrieved through $v_{\rm nth}=\zeta/\sqrt{2}$.

$$FWHM^{2} = 4 \ln 2 \left(\frac{\lambda}{c}\right)^{2} \left(\frac{2k_{B}T_{i}}{m_{i}} + \zeta^{2}\right), \tag{4.16}$$

where v_{nth} is the non-thermal velocity derived from subtracting the thermal contribution, T_i is the ion temperature, and m_i is the ion mass. c and k_B are the speed of light and the Boltzmann constant, respectively.

Non-thermal velocities from Hassler et al. (1990), Chandrasekhar et al. (1991), Banerjee et al. (1998), Doyle et al. (1998, 1999), Esser et al. (1999), Contesse et al. (2004), Banerjee et al. (2009), Landi and Cranmer (2009) and Singh et al. (2011) and Bemporad and Abbo (2012) are presented in Figure 4.4.

Considering first random motions in the transverse (\bot_2) direction, we suggest that the small scale density fluctuations (mostly near the inner scale q_i^{-1} of density turbulence responsible for radio-wave scattering; Kontar et al. 2023) are advected by large-scale random plasma motions with speeds corresponding to the outer scale of the turbulence. Within this framework, the velocity fluctuations $\langle v_{\bot_2}^2 \rangle$ have a line broadening effect that is identical to that of non-thermal ion velocities, and so can be modeled by replacing the Dirac delta-function resonance condition by a finite-width Gaussian characterized by a turbulent velocity v_\perp :

$$\delta\left(\Omega(\mathbf{q}) - \mathbf{q} \cdot \mathbf{v}_g\right) \to \frac{1}{\sqrt{2\pi \, q_{\perp_2}^2 \langle v_{\perp_2}^2 \rangle}} \exp\left[-\frac{\left(\Omega(\mathbf{q}) - \mathbf{q} \cdot \mathbf{v}_g\right)^2}{2 \, q_{\perp_2}^2 \langle v_{\perp_2}^2 \rangle}\right] , \qquad (4.17)$$

where $\langle v_{\perp_2}^2 \rangle$ is the variance of large-scale motion velocities.

The presence of random motions superimposed on the large-scale flows thus gives diffusion tensor components

$$D_{ij} = \frac{\pi \omega_{pe}^4}{4 \omega^2} \int q_i \, q_j \, S(\mathbf{q}) \, \frac{1}{\sqrt{2\pi \, q_{\perp_2}^2 \langle v_{\perp_2}^2 \rangle}} \exp\left[-\frac{(\Omega(\mathbf{q}) - \mathbf{q} \cdot \mathbf{v}_g)^2}{2 \, q_{\perp_2}^2 \langle v_{\perp_2}^2 \rangle} \right] \, \frac{d^3 q}{(2\pi)^3} . \tag{4.18}$$

Integrating in the approximation $q_{\perp_2}^2\langle v_{\perp_2}^2\rangle\ll q^2c^2$ and taking $\Omega=0$ we obtain the diffusion tensor (see Equation (19) in Appendix B)

$$\mathbf{D} = \frac{\pi \omega_{pe}^4}{16 \,\omega^2 c} \, \overline{q \,\epsilon^2} \, \begin{pmatrix} \alpha^2 & 0 & 0 \\ 0 & 1 & 0 \\ 0 & 0 & \frac{\langle v_{\perp_2}^2 \rangle}{c^2} \end{pmatrix}$$
(4.19)

leading to a frequency broadening that is mathematically similar to Equation (4.14), but where $\langle v_{\perp_2}^2 \rangle$ now represents random velocity fluctuations.

Similar considerations apply to random motions in the parallel (i.e., radial) direction, with a factor of α^2 applied, so that if there are random motions in both directions (see Equation (24) in Appendix B.2),

$$\mathbf{D} = \frac{\pi \omega_{pe}^4}{16 \,\omega^2 c} \, \overline{q \,\epsilon^2} \, \begin{pmatrix} \alpha^2 & 0 & 0 \\ 0 & 1 & 0 \\ 0 & 0 & \frac{\alpha^2 \,\langle v_{\parallel}^2 \rangle + \langle v_{\perp_2}^2 \rangle}{c^2} \end{pmatrix} . \tag{4.20}$$

Again, since $\alpha < 1$, perpendicular motions are more effective at frequency broadening than radial (parallel) motions.

4.4 Observed frequency broadening

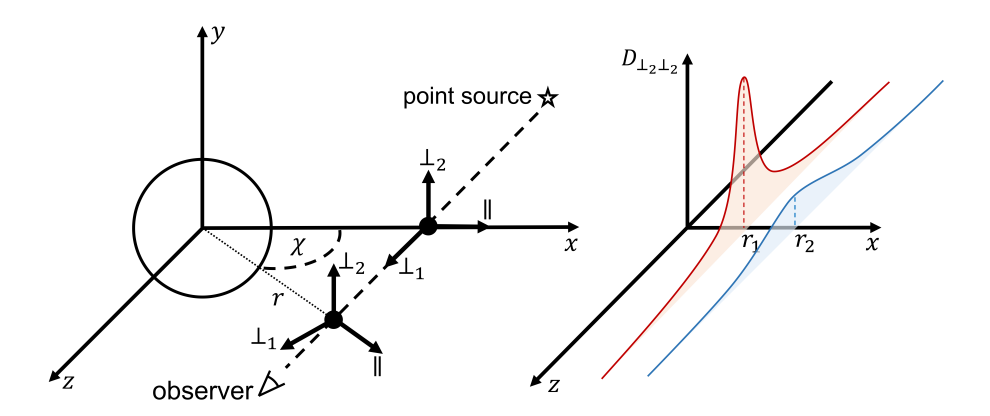


Figure 4.2: The left panel shows the Sun-centered coordinate system and its relation to heliocentric distance and the line of sight from a distant point source. The broadening of point sources is calculated as an integral along z. The right-hand panel qualitatively shows how the $D_{\perp_2\perp_2}$ diffusion tensor component (see e.g., Equation (4.8)) varies along the direction of propagation of the radio wave (z), as illustrated for sources at two different heliocentric distances r(z=0), with $r_1 < r_2$. Figure made by Daniel L. Clarkson.

To compare with the observations, we note that radio wave with wavevector $\mathbf k$ is propagating along the z-direction. We assign the \parallel direction with the (assumed radial) solar magnetic field $\mathbf B$ (Figure 4.2). We also assign the \perp_1 direction to the perpendicular direction that is aligned with the wave propagation direction at z=0, and \perp_2 to the perpendicular direction that is orthogonal to both \parallel and \perp_1 , i.e., perpendicular to the projection of the radial direction on the plane of the sky. The right-handed $(\parallel, \perp_2, \perp_1)$ coordinate system is obtained by rotating the (x, y, z) coordinate system by an angle $(-\chi)$ around the y-axis (Figure 4.2).

Analogously to the results from the three previous subsections, the variance of the wavenumber k along the path of the radio wave due to motions in the plane of the sky (here denoted by $v_{\perp \mathbf{k}}$) in the solar atmosphere can be written as

$$\frac{d\langle k_z^2 \rangle}{dt} = 2D_{zz} = \frac{\pi \omega_{pe}^4}{8 \,\omega^2 \,c} \, \overline{q \,\epsilon^2} \, \frac{\alpha^2 \langle v_{\parallel}^2 \rangle \cos^2 \chi + \langle v_{\perp_2}^2 \rangle + \langle v_{\perp_1}^2 \rangle \sin^2 \chi}{c^2} \quad , \tag{4.21}$$

where $\chi(z)$ is the angle between the radial direction of the magnetic field and the x-axis (see Figure 4.2). For perpendicular motions that are dominated by gyrotropic turbulence, $\langle v_{\perp_1}^2 \rangle = \langle v_{\perp_2}^2 \rangle = \langle v_{\perp}^2 \rangle$, this can be written as

$$\frac{d\langle k_z^2 \rangle}{dt} = \frac{\pi \omega_{pe}^4}{8 \,\omega^2 \,c} \,\overline{q \,\epsilon^2} \,\frac{v_{\perp \mathbf{k}}^2}{c^2} \ , \tag{4.22}$$

where

$$v_{\perp \mathbf{k}}^2 = \sqrt{\alpha^2 \langle v_{\parallel}^2 \rangle \cos^2 \chi + \langle v_{\perp}^2 \rangle (1 + \sin^2 \chi)}$$
 (4.23)

represents the weighted sum of all motions perpendicular to \mathbf{k} , i.e., in the (x,y) plane of the sky, and the $\langle v_\parallel^2 \rangle$ term is the sum of both steady flows (v^2) and random velocities $(\langle v^2 \rangle)$ in the parallel direction. Both random motions and oscillations with the same phase speed contribute at the same level. Such motions and/or oscillations of density fluctuations in the plane of the sky are perpendicular to the direction of radio wave propagation \mathbf{k} ; they hence lead to a change in wavenumber $\Delta \mathbf{k}$ that is aligned with \mathbf{k} and so to a change in the magnitude $|\mathbf{k}|$, i.e., to frequency broadening. In the limit $\omega \gg \omega_{pe}$, the group velocity of the radio wave $\mathbf{v}_{gr} = \partial \omega/\partial \mathbf{k} = c^2 k/\omega \simeq c$. The frequency broadening rates per unit travel distance $v_{gr} dt$ along the direction of propagation z can be written (similarly to Kontar et al. 2023) as

$$\frac{\langle \Delta f^2 \rangle}{f^2} = \int_{los} \frac{1}{k_z^2} \frac{d \langle k_z^2 \rangle}{c \, dt} dz = \int_{los} \frac{\pi}{8} \frac{v_{\perp \mathbf{k}}^2}{c^2} \frac{\omega_{pe}^4}{\omega^4} \, \overline{q \, \epsilon^2}(r) \, dz \quad , \tag{4.24}$$

which can be integrated for known $v_{\perp \mathbf{k}}^2$. The right panel of Figure 4.3 shows the predicted (taking analytical expression for n^2 \overline{q} $\overline{\epsilon}^2$ from Kontar et al. 2023, derived from solar observations) broadening for a typical perpendicular speed $v_{\perp}=30~\mathrm{km~s^{-1}}$ from non-thermal line measurements, and $v_{\parallel}=\sqrt{v_s^2+v_{\mathrm{sw}}^2}$ where the sound speed v_s is given by Equation (4.27) and the solar wind speed v_{sw} is given by Equation (4.28). Importantly, the result does not depend on the density model, but on the strength of density fluctuations n^2 \overline{q} $\overline{\epsilon}^2$ and the plasma velocities (note \overline{q} $\overline{\epsilon}^2$ $\propto 1/n^2$).

Noting that the largest contribution to frequency broadening comes from the high density region near z=0 (Figure 4.2), and hence, to a good approximation, we can take $\chi\simeq 0$ in Equation (4.24). Thus, we can write $v_{\perp \mathbf{k}}^2\simeq \alpha^2\langle v_\parallel^2\rangle+\langle v_\perp^2\rangle$ taking values at z=0. The frequency broadening integrated over the path of the radio wave is now given by

$$\frac{\langle \Delta f^2 \rangle}{f^2} \simeq \frac{\pi}{8} \frac{v_{\perp \mathbf{k}}^2}{c^2 \omega^4} \int_{los} \omega_{pe}^4 \overline{q \, \epsilon^2} \, dz = \frac{2\pi^3 e^4}{m_e^2 \, c^2 \, \omega^4} v_{\perp \mathbf{k}}^2 \int_{los} n^2 \, \overline{q \, \epsilon^2} \, dz \; ; \tag{4.25}$$

i.e.,

$$\frac{\Delta f}{f} \simeq \frac{1}{(8\pi)^{1/2}} \left(\frac{e^2}{m_e c}\right) \left(\int_{los} n^2 \overline{q \epsilon^2} dz\right)^{1/2} \frac{v_{\perp \mathbf{k}}}{f^2} . \tag{4.26}$$

which shows that the fractional frequency broadening $\Delta f/f$ depends on the carrier frequency f as $1/f^2$ and is determined by motions in the plane of the sky. Although both parallel and perpendicular velocities may be present, the parallel velocities (both steady flows and random motions) are weighted by the anisotropy parameter $\alpha < 1$ (cf. the expression for frequency broadening in an isotropic plasma; Equation (36) of Bian et al. 2019). Knowing the anisotropy factor α and the $n^2 \overline{q \, \epsilon^2}(z)$ density fluctuation profile from independent measurements, one can deduce the characteristic speeds of density fluctuations using Equation (4.26).

Sound and solar wind speeds are calculated as:

• Sound speed: The electron temperature of the solar wind is observed to decrease with heliocentric distance: $T_e \propto r^{-(0.3-0.7)}$ (e.g., Stverak et al. 2015). If we model the temperature as $T_e \simeq 2 \times 10^6 \, (r/R_\odot - 1)^{-0.5}$ K, where the index was taken to be the average from Stverak et al. (2015) and the coronal temperature is normalised to 2 MK, then the sound speed $v_s \simeq \sqrt{k_B T_e/m_i}$ varies with heliocentric distance r as

$$v_s(r) \simeq 130 \left(\frac{r}{R_{\odot}} - 1\right)^{-0.25} \text{ km s}^{-1}$$
 (4.27)

• Solar wind speed: In the spherically symmetric expanding corona (Parker 1958), mass conservation $v_{sw} r^2 n(r) = \text{const requires that, with a typical solar wind speed of } 400 \, \text{km s}^{-1}$ at 1 au,

$$v_{\rm SW}(r) \approx 400 \, \left(\frac{n \, (1 \, {\rm au})}{n(r)}\right) \, \left(\frac{1 \, {\rm au}}{r}\right)^2 \, {\rm km \, s^{-1}} \ ,$$
 (4.28)

where n(r) is the plasma density.

For the propagation of a radio wave from a distant radio source to the observer at the Earth (see, e.g., Kontar et al. 2023, and Figure 4.2), with $r_{\rm obs}=r(z=0)$, and assuming that the various quantities in the integral are functions of heliocentric distance $r=\sqrt{r_{\rm obs}^2+z^2}$, Equation (4.24) can be written as

$$\frac{\langle \Delta \omega^2 \rangle}{\omega^2} = \frac{2 \pi^3 e^4}{m_e^2 c^2 \omega^4} \int_{-\infty}^{1 \text{ au}} n^2 \left(\sqrt{r_{\text{obs}}^2 + z^2} \right) \overline{q \epsilon^2} \left(\sqrt{r_{\text{obs}}^2 + z^2} \right) \times \left[\alpha^2 \langle v_{\parallel}^2 \rangle \left(\sqrt{r_{\text{obs}}^2 + z^2} \right) \cos^2 \chi + \langle v_{\perp}^2 \rangle \left(\sqrt{r_{\text{obs}}^2 + z^2} \right) (1 + \sin^2 \chi) \right] dz .$$
(4.29)

With the substitution $z = r_{\text{obs}} \tan \chi$, this can be written

$$\frac{\langle \Delta \omega^{2} \rangle}{\omega^{2}} = \frac{2 \pi^{3} e^{4}}{m_{e}^{2} c^{2} \omega^{4}} \frac{r_{\text{obs}}}{R_{\odot}} \int_{-\pi/2}^{\tan^{-1}(215 R_{\odot}/r_{\text{obs}})} n^{2}(r_{\text{obs}} \sec \chi) \overline{q \epsilon^{2}} R_{\odot}(r_{\text{obs}} \sec \chi) \times \left[\alpha^{2} \langle v_{\parallel}^{2} \rangle (r_{\text{obs}} \sec \chi) \cos^{2} \chi + \langle v_{\perp}^{2} \rangle (r_{\text{obs}} \sec \chi) (1 + \sin^{2} \chi)\right] \sec^{2} \chi \, d\chi . \tag{4.30}$$

Figure 6 of Kontar et al. (2023) shows that, from observations of extra-solar radio sources,

$$n^2 (r_{\text{obs}} \sec \chi) \ \overline{q \, \epsilon^2} \, R_{\odot} (r_{\text{obs}} \sec \chi) \simeq 6.5 \times 10^{14} \left(\frac{r_{\text{obs}} \sec \chi}{R_{\odot}} - 1 \right)^{-5.17} \text{ cm}^{-6} \ .$$
 (4.31)

Using this expression and taking the velocity variances outside the integral as averages, yields

$$\frac{\langle \Delta \omega^{2} \rangle}{\omega^{2}} = 6.5 \times 10^{14} \left(\frac{e^{4}}{8\pi m_{e}^{2} c^{2} f^{4}} \right) \left(\frac{r_{\text{obs}}}{R_{\odot}} \right)^{-4.17} \times \left\{ \alpha^{2} \overline{\langle v_{\parallel}^{2} \rangle} \int_{-\pi/2}^{\tan^{-1}(215R_{\odot}/r_{\text{obs}})} \left(1 - \frac{R_{\odot} \cos \chi}{r_{\text{obs}}} \right)^{-5.17} \cos^{5.17} \chi d\chi + \overline{\langle v_{\perp}^{2} \rangle} \int_{-\pi/2}^{\tan^{-1}(215R_{\odot}/r_{\text{obs}})} \left(1 - \frac{R_{\odot} \cos \chi}{r_{\text{obs}}} \right)^{-5.17} \cos^{3.17} \chi \left(1 + \sin^{2} \chi \right) d\chi \right\}. \tag{4.32}$$

At closest-approach distances $r_{\rm obs}\gg R_{\odot}$, the term $(1-R_{\odot}\cos\chi/r_{\rm obs})^{-5.7}\simeq 1$. Adopting this approximation, the frequency broadening reduces to the relatively simple form

$$\frac{\langle \Delta \omega^2 \rangle}{\omega^2} = 6.5 \times 10^{14} \left(\frac{e^4}{8\pi m_e^2 c^2 f^4} \right) \left(\frac{r_{\text{obs}}}{R_{\odot}} \right)^{-4.17} \times \left\{ \alpha^2 \overline{\langle v_{\parallel}^2 \rangle} \int_{-\pi/2}^{\chi_{\text{obs}}} \cos^{5.17} \chi d\chi + \overline{\langle v_{\perp}^2 \rangle} \int_{-\pi/2}^{\chi_{\text{obs}}} \cos^{3.17} \chi \left(1 + \sin^2 \chi \right) d\chi \right\} .$$
(4.33)

where $\chi_{\rm obs}=\tan^{-1}{(215R_{\odot}/r_{\rm obs})}$. Each integral can be split into two parts: one from $\chi=-\pi/2$ to 0 (corresponding to the incoming ray from ∞ to the distance of closest approach $r_{\rm obs}$, and other from 0 to $\chi_{\rm obs}$, corresponding to the outgoing ray from $r_{\rm obs}$ to $1{\rm au}$. The integral can then be expressed in terms of beta functions and incomplete beta functions, respectively, viz.

$$\frac{\langle \Delta \omega^2 \rangle^{1/2}}{\omega} = 2.55 \times 10^7 \left(\frac{e^2}{m_e c} \right) \left(\frac{r_{\text{obs}}}{R_{\odot}} \right)^{-2.085} \left[\alpha^2 \, \beta_{\parallel}^2 \, v_{\parallel, \text{rms}}^2 + \beta_{\perp}^2 \, v_{\perp, \text{rms}}^2 \right]^{1/2} \times \frac{1}{f^2} , \quad (4.34)$$

where we have defined $v_{\parallel,\mathrm{rms}} = \overline{\langle v_\parallel^2 \rangle}^{1/2}$ and $v_{\perp,\mathrm{rms}} = \overline{\langle v_\perp^2 \rangle}^{1/2}$ and

$$\beta_{\parallel} \left(\frac{r_{\rm obs}}{R_{\odot}} \right) = \left[\frac{{\rm B}(1; 3.085, 0.5) + {\rm B}(\psi; 3.085, 0.5)}{16\pi} \right]^{1/2} \;\; , \label{eq:beta}$$

$$\beta_{\perp} \left(\frac{r_{\rm obs}}{R_{\odot}} \right) = \left[\frac{{\rm B}(1; 2.085, 0.5) + {\rm B}(\psi; 2.085, 0.5) + {\rm B}(1; 2.085, 1.5) + {\rm B}(\psi; 2.085, 1.5)}{16\pi} \right]^{1/2} \ .$$

Here $\mathrm{B}(\psi;u,v)$ are the (incomplete for $\psi<1$) beta functions corresponding to the integrals $2\int_0^{\pi/2}\cos^{5.17}\chi d\chi$, $2\int_0^{\pi/2}\cos^{3.17}\chi d\chi$, and $2\int_0^{\pi/2}\cos^{3.17}\chi\sin^2\chi d\chi$, and $\psi=\left[1+(r_{\mathrm{obs}}/215R_{\odot})^2\right]^{-1}$.

The ratio of the lead terms in the expressions for β_{\parallel} and β_{\perp} is

$$\sqrt{\frac{\Gamma(3.085)\ \Gamma(0.5)\ /\ \Gamma(3.585)}{\Gamma(2.085)\ \Gamma(0.5)\ /\ \Gamma(2.585)}} = \sqrt{\frac{2.085}{2.585}} \simeq 0.9 \ ,$$

showing that the contributions from motions in the \parallel and \perp_2 directions are similar (apart from the anisotropy factor α). But, since $\alpha^2 \ll 1$, we can, to a good approximation, neglect the contribution from $v_{\parallel, \rm rms}$ and write Equation (4.34) as

$$\frac{\langle \Delta \omega^2 \rangle^{1/2}}{\omega} = 2.55 \times 10^7 \,\beta_\perp \, \left(\frac{e^2}{m_e \, c}\right) \, \left(\frac{r_{\rm obs}}{R_\odot}\right)^{-2.085} \, v_{\perp,\rm rms} \, \times \frac{1}{f^2} \ . \tag{4.35}$$

Scaling to a nominal frequency of f = 1 GHz (Figure 4.3), this evaluates to

$$\frac{\Delta f}{f} \simeq 2.1 \times 10^{-13} \ \beta_{\perp} \ v_{\perp,\text{rms}} \left(\frac{r_{\text{obs}}}{R_{\odot}}\right)^{-2.085} \left(\frac{1 \,\text{GHz}}{f}\right)^{2} , \qquad (4.36)$$

where we have written Δf for $\langle \Delta f^2 \rangle^{1/2}$. Equation (4.36) provides a simple, but nevertheless accurate, analytical approximation for the frequency broadening, valid for $r_{\rm obs} \gg R_{\odot}$. With a nominal $r_{\rm obs} = 10\,R_{\odot}$, we obtain $\beta_{\perp} \simeq 0.25$ and so $\Delta f/f \simeq 4 \times 10^{-16}\,v_{\perp,\rm rms}\,(f[{\rm GHz}])^{-2}$, corresponding to $\Delta f \simeq 4 \times 10^{-7}\,v_{\perp,\rm rms}$ Hz at $f=1\,{\rm GHz}$. Figure 4.3 shows that $\Delta f \simeq 3$ Hz at $r=10\,R_{\odot}$, corresponding to $v_{\perp,\rm rms} \simeq 7.5 \times 10^6\,{\rm cm}\,{\rm s}^{-1}$, i.e., 75 km s⁻¹.

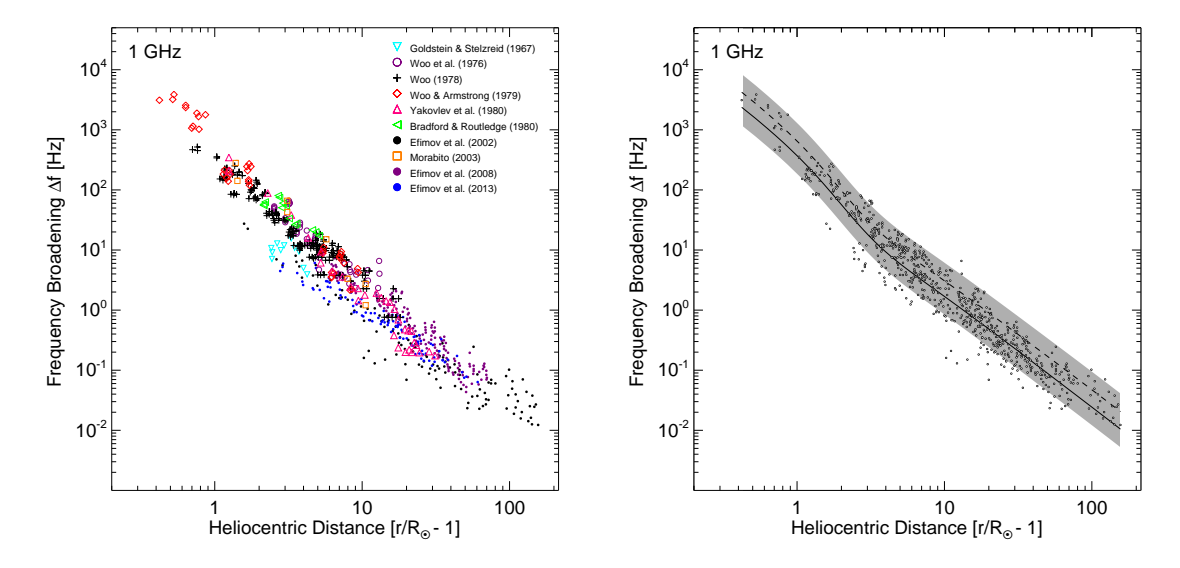


Figure 4.3: Left: Observed spectral broadening $\Delta f = \sqrt{\langle \Delta f^2 \rangle}$ (the square root of the variance) of spacecraft signals observed through the corona from various studies, where each carrier signal is scaled to f=1 GHz using $\Delta f/f \propto 1/f^2$. Right: Form of Δf derived from Equations (4.23) and (4.24), for $v_{\perp}=30$ km s⁻¹, and $v_{\parallel}=\sqrt{v_s^2+v_{\rm sw}^2}$, where the sound speed v_s is given by Equation (4.27) and the solar wind speed $v_{\rm sw}$ is given by Equation (4.28). The solid and dashed lines show Δf derived using $1\times \overline{q\,\epsilon^2}$ for $\alpha=0.25$ and $\alpha=0.4$, respectively, while the grey area shows the range in Δf . The lower bound is given by $1/2\times \overline{q\,\epsilon^2}$ for $\alpha=0.25$, and the upper bound is given by $2\times \overline{q\,\epsilon^2}$ for $\alpha=0.4$. Figures made by Daniel L. Clarkson.

4.5 Frequency broadening measurements

Frequency broadening observations have been conducted a number of times using signals from different spacecraft (Goldstein and Stelzried 1967; Woo et al. 1976; Woo 1978; Woo and Armstrong 1979; Bradford and Routledge 1980; Yakovlev et al. 1980; Efimov et al. 2002; Morabito et al. 2003; Efimov et al. 2008, 2013). When not already presented as a standard deviation σ , frequency broadening measurements are converted to give $\Delta f \equiv \sigma$ for use in Figure 4.3. Reported data that relate to solar transient events have been removed, and only one-way signals are being considered. Goldstein and Stelzried (1967) define the bandwidth as the width of an equivalent rectangle of the same height and area as the measured curves. Comparing with a normalized

Gaussian distribution, this implies that the reported bandwidth is $B=\sqrt{2\pi}\,\sigma$, so that $\Delta f=\sigma=B/\sqrt{2\pi}$. Yakovlev et al. (1980) define the bandwidth as the 'width of the spectral line', which, in the absence of more detailed specifications, is taken to be a measure of the standard deviation σ . The signal measurements of Morabito et al. (2003) are provided as $B={\rm FWHM}$, which converts to $\Delta f=\sigma=B/2\sqrt{2\ln 2}$. Finally, Woo et al. (1976), Woo (1978) and Woo and Armstrong (1979) and Bradford and Routledge (1980) define the bandwidth B through the relation

$$\int_0^{B/2} P(f) \, df = \frac{1}{2} \int_0^{\infty} P(f) \, df .$$

For a Gaussian distribution with standard deviation σ , this reduces to

$$\operatorname{erf}\left(\frac{B}{2\sqrt{2}\,\sigma}\right) = \frac{1}{2} \ ,$$

where the error function is $\operatorname{erf}(x) = \int_0^x e^{-t^2} dt$. Thus, for these data sets

$$\Delta f = \sigma = \left[2\sqrt{2}\operatorname{erf}^{-1}\left(\frac{1}{2}\right)\right]^{-1}B \simeq 0.75 B$$
.

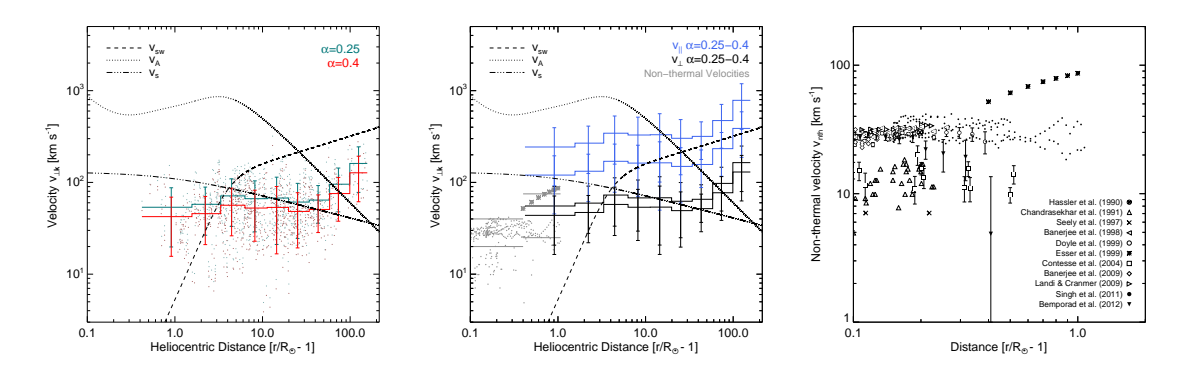


Figure 4.4: Left: Plane-of-sky velocity $v_{\perp k}$ calculated using frequency broadening measurements from Figure 4.3, Equation (4.37), and the $n^2 \, \overline{q} \, \epsilon^2$ values at various distances r derived from measurements of other phenomena, such as angular broadening of extra-solar sources and the location, size and timing of solar radio bursts (Kontar et al. 2023). The green and red points show the conversion of individual Δf data points from Figure 4.3, for different values of α , with binned averages and weighted uncertainties on each bin. **Middle:** Parallel and perpendicular velocities v_{\parallel} (blue) and v_{\perp} (black) required to solely explain the frequency broadening measurements in Figure 4.3. The grey dots and stars show a summary of the measured values of the non-thermal velocity standard deviation from the right panel. Also shown is the solar wind speed $v_{\rm SW}$ (Equation (4.28)), the ion-sound speed v_s (Equation (4.27)), and the Alfvén speed from Equation (4.38), obtained using the density and magnetic field models in Kontar et al. (2023), i.e. Equations (1.3,1.2). **Right:** 1σ non-thermal velocities $v_{\rm nth}$ from line-of-sight Doppler broadening of coronal lines. Figures made by Daniel L. Clarkson.

The left panel of Figure 4.3 shows the compilation of 1σ frequency broadening (the square root of the variance, $\Delta f \equiv \sqrt{\langle \Delta f^2 \rangle}$) of spacecraft signals as a function of heliocentric distance. For observation at different frequencies, the broadened quantity is scaled to 1 GHz using $\Delta f_{\rm 1GHz} = \Delta f_{\rm obs} \left(f_{\rm obs} [{\rm GHz}] \right)^2$. The trend of Δf with heliocentric distance follows a broken power-law, with a steeper power law index ~ -2 below $\sim 3\,R_\odot$, transitioning to a somewhat flatter power-law index of approximately -1.7 above $\sim 10\,R_\odot$.

Instead of assuming a flow (or turbulent) velocity value, we can alternatively use the measured frequency broadenings to determine the associated velocity, by rewriting Equation (4.26) in the form

$$v_{\perp \mathbf{k}} \equiv \sqrt{\alpha^2 \langle v_{\parallel}^2 \rangle + \langle v_{\perp}^2 \rangle} \simeq \frac{(8\pi)^{1/2}}{c \, r_o} \frac{f^2}{\left(\int_{los} n^2 \, \overline{q \, \epsilon^2} \, dz \right)^{1/2}} \, \frac{\Delta f}{f} \quad , \tag{4.37}$$

where $r_o=e^2/m_ec^2$ is the classical electron radius and the integral is evaluated taking $n(r[z])\overline{q\,\epsilon^2}\,(r[z])$ from Kontar et al. (2023). In the left panel of Figure 4.4 we show $v_{\perp \mathbf{k}}$ (in km s⁻¹) as a function of heliocentric distance r, for two different values of the anisotropy parameter α . Further, by taking $v_\perp=0$ or $v_\parallel=0$, one can obtain an upper limit on the magnitude of the remaining component of v_\perp . The middle panel of Figure 4.4 compares these maximum values of v_\parallel and v_\perp with various other speeds, including the solar wind speed $v_{\rm SW}$, the sound speed v_s , the Alfvén speed v_A , and nonthermal velocities deduced from UV spectral line broadening observations. These reference speeds are calculated as follows:

• Alfvén speed: The Alfvén speed

$$v_A(r) = \frac{B(r)}{\sqrt{4\pi m_i n(r)}} \tag{4.38}$$

is obtained using the magnetic field and density models in Equations (A1) and (A2) of Kontar et al. (2023).

• Nonthermal velocities: Nonthermal turbulent velocities are inferred through measurement of the excess width of EUV coronal spectral lines compared to their thermal widths. Figure 4.4 shows various measurements of 1σ nonthermal velocities at different heliocentric distances; this information is also summarized in the middle panel of Figure 4.4.

The middle panel of Figure 4.4 shows clearly that the velocities deduced from frequency broadening measurements become dominated by the solar wind speed at large heliocentric distances $r>10\,R_\odot$. However, closer to the Sun at $r\lesssim10\,R_\odot$, the solar wind speed contribution is much smaller than the inferred $v_{\perp \bf k}$ speeds, whether radial velocities v_{\parallel} in the range (100-300) km s⁻¹, or perpendicular motions v_{\perp} in the range (25-75) km s⁻¹, or a combination of such motions are considered. Both these inferred speed ranges are well below the Alfvén speed; however, perpendicular motions of this magnitude are quite consistent with the nonthermal speeds deduced from the observed widths of UV spectral lines in both open-field regions and closed-field loops. The next section discusses such nonthermal turbulent motions and their possible role in coronal heating.

4.6 Energy Cascade and Dissipation Rates

As discussed in Section 1.4.2, the quantity $\epsilon_{\ell_{\perp}}$ is the power per unit mass evaluated at the outer scale of the inertial range; it is the rate at which energy enters the turbulent cascade process at the largest scales, and it is a scale-invariant quantity within the inertial range of turbulence. The value of $\epsilon_{\ell_{\perp}}$ often serves as a measure of coronal heating via Alfvén turbulent cascade. The left panel of Figure 4.5 shows the values of $\epsilon_{\ell_{\perp}}$ deduced from the perpendicular velocities inferred from radio wave frequency broadening observations (Figure 4.4). They suggest an energy cascade rate $\epsilon_{\ell_{\perp}} \simeq 10^{11} \, \mathrm{erg} \, \mathrm{g}^{-1} \, \mathrm{s}^{-1}$ between 2-3 R_{\odot} , a value that is similar to earlier estimates (e.g., Hollweg 1986; Cranmer and van Ballegooijen 2005).

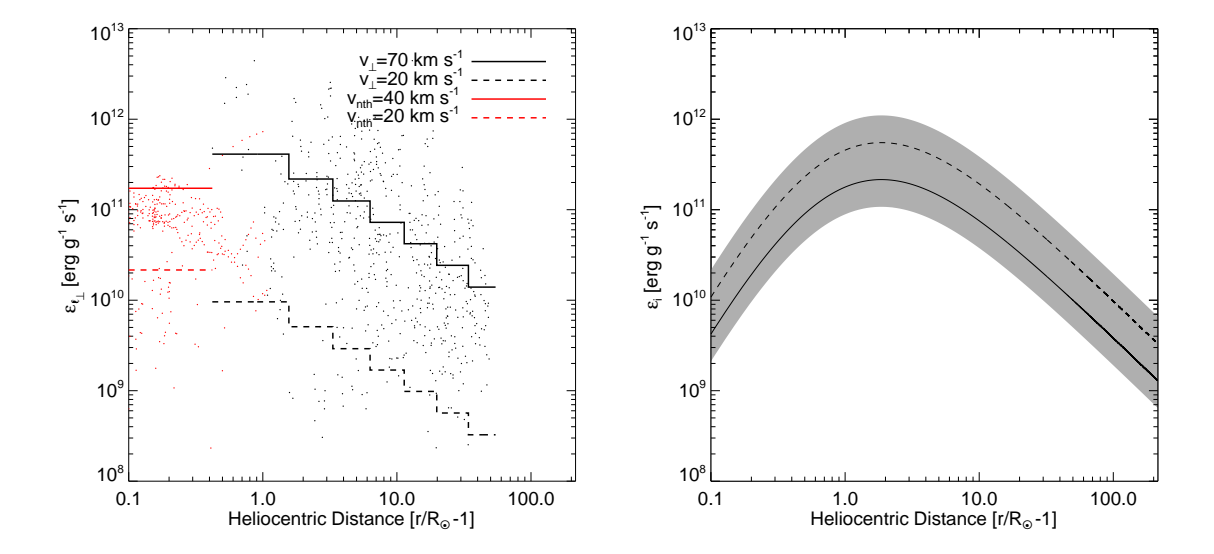


Figure 4.5: Left: Available power per unit mass, $\epsilon_{\ell_{\perp}}$ (erg g⁻¹ s⁻¹) from Equation (1.4), using perpendicular velocity fluctuations from Figure 4.4. The solid and dashed lines correspond to the range (20-70) km s⁻¹ (black) from frequency broadening measurements, and (20-40) km s⁻¹ for $r < 1.4\,R_{\odot}$ for non-thermal velocities from coronal lines (red). Right: Coronal heating rate per unit mass (erg g⁻¹ s⁻¹) from Landau damping of ion-sound waves given by Equation (1.10). As in the right panel of Figure 4.3, the solid and dashed lines show $1 \times \overline{q} \, \epsilon^2$ for $\alpha = 0.25$ and $\alpha = 0.4$, respectively, and the grey area corresponds to the range of values $[1/2, 2] \times \overline{q} \, \epsilon^2$, considering both values of α. Figures made by Daniel L. Clarkson.

At inner scales, power supplied to the corona through damping of ion-sound waves is calculated using the results of Section 1.4.3, with the heating rate given by Equation (1.10) shown in the right panel of Figure 4.5. The heating profile presents a broad maximum at (1-3) R_{\odot} , consistent with the observed increasing temperature of the solar corona out to this radius (Wheatland et al. 1997). The inferred energy deposition rate, integrated over the range of heights $(2-3R_{\odot})$ where it is most effective, corresponds to an energy flux, $\epsilon_i(2R_\odot)m_in(2R_\odot)R_\odot\sim 3\times 10^5~{\rm erg}~{\rm cm}^{-2}~{\rm s}^{-1}$ (300 W m $^{-2}$), where $\epsilon_i(2R_{\odot}) \simeq 5 \times 10^{11} {\rm \ erg \ g}^{-1} {\rm \ s}^{-1}$ and $n(2R_{\odot}) \simeq 5 \times 10^6 {\rm \ cm}^{-3}$. Note that, while this value represents a useful constraint on the heating and dynamic energy terms in the corona, directly comparing its magnitude to such terms represents a considerable over-simplification of the modeling of coronal heating and/or solar wind acceleration. In particular, these estimates are valid strictly under the assumption of a Maxwellian plasma, while the damping rate locally would instead go to zero as the gradient in the plateau goes to zero, substantially reducing Landau damping of ion-sound waves and implying that the damping and heating rates presented here should be regarded as upper limits, with the actual rates expected to be significantly weaker. Nevertheless, such an energy flux is broadly consistent with that required to balance energy losses and so heat the corona (e.g., Withbroe and Noyes 1977; Hollweg 1986; Withbroe 1988, find required energy fluxes of $\sim 4-6 \times 10^5 \ \rm ergs \ cm^{-2}$ s^{-1}).

The heating rate (1.10) is proportional to the quantity $\overline{q\,\epsilon^2}$, which can be inferred from observations related to radio-wave scattering. As shown in Figure 1 of Kontar et al. (2023), $\overline{q\,\epsilon^2}$ is dominated by fluctuations at short wavelengths near the inner scale $q_i^{-1} \sim c/\omega_{pi}$, so that:

$$\overline{q \,\epsilon^2} \simeq 5 \, q_i \, \frac{\langle \delta n_i^2 \rangle}{n^2} \ .$$
 (4.39)

The coronal heating rate per unit mass due to absorption at heliocentric distance r can therefore be expressed rather succinctly as $\epsilon_i(r) \simeq 4 \, \alpha \, q_i \, v_s^3 \, \langle \delta n_i^2 \rangle / n^2$.

The quantities $\epsilon_{\ell_{\perp}}$ and ϵ_i are associated with very different physical models, and they are associated with length scales that span five orders of magnitude: the power generated in large-scale Alfvén motions $\epsilon_{\ell_{\perp}}$ is dominated by scales $\ell_{\perp}(r=2\,R_{\odot})\simeq 10^4$ km (from Equation (1.5)), while the energy dissipation rate ϵ_i due to ion-sound wave damping is dominated by waves at the inner scale q_i^{-1} of the turbulence spectrum, which at $r = (2-3) R_{\odot}$ is of order 0.1 km (see Kontar et al. (2023)). Despite this vast difference in characteristic scales, the quantities $\epsilon_{\ell_{\perp}}$ and ϵ_i at $r \simeq (1-2) R_{\odot}$ are very similar; indeed, they are identical within the error bars, with $\epsilon_{\ell_\perp} \simeq \epsilon_i \simeq$ $10^{11} \ erg \ g^{-1} \ s^{-1}$ (Figure 4.5). This result is both unexpected and tantalizing, suggesting that the energy associated with large-scale magnetic field motions can effectively cascade over the entire inertial range, eventually appearing as small-scale ion-sound waves. In a Maxwellian plasma these waves would be very effectively damped, leading to plasma heating. In the solar wind, however, non-Maxwellian velocity distribution functions can substantially reduce this damping, so the heating rates inferred here should be regarded as upper limits. Even so, this intriguing result has significant implications for models of coronal heating.

4.7 Summary and Discussion

Using a density fluctuation model obtained from analysis of solar radio bursts, combined with frequency broadening measurements from various spacecraft, we have deduced the magnitude of the characteristic velocities in the solar corona and the solar wind. The inferred velocities depend on the anisotropy of the density turbulence. The amount of spacecraft signal broadening, and the anisotropic density fluctuation inferred from solar burst data, tell a remarkably coherent story about the level of density turbulence in the solar corona and the bulk flow speeds present; the latter are consistent with previously published values that employed different analysis

techniques. The perpendicular velocities are also consistent with the non-thermal speeds deduced from line-of-sight Doppler broadening of spectral lines in the low corona. Interpreted as Alfvén wave amplitudes, these results allow us to determine the amount of energy per unit time transferred in the turbulent cascade from large to small scales, and eventually deposited in the low corona and into the solar wind.

At distances $r \gtrsim 10\,R_\odot$, the frequency broadening is dominated by solar wind motion. The deduced velocity values (200-600) km s⁻¹ at ~100 R_\odot are consistent with previous scintillation measurements (e.g., Ekers and Little 1971; Armstrong and Woo 1981) and are also consistent with characteristic solar wind speeds at these distances (e.g., Bunting et al. 2024). The anisotropy of density fluctuations appears to be an important ingredient: if the spectrum of density fluctuations were isotropic, only much slower sub-solar-wind speeds (up to ~ $100~{\rm km~s^{-1}}$) would be consistent with the frequency broadening observations; alternatively, the observed frequency broadening would be consistent with observed solar wind speeds only if the level of density fluctuations were much lower than inferred from other observations, such as angular broadening of extra-solar sources.

Closer to the Sun $(r \lesssim 10\,R_\odot)$, however, the solar wind speed becomes small, while the velocities required to explain the frequency broadening observations remain large. The frequency observations require either speeds (20-70) km s⁻¹ in the perpendicular direction, or (100-300) km s⁻¹ in the parallel direction or both. Within the description adopted, these two scenarios (or a combination of the two) cannot be meaningfully distinguished.

Given the possible importance of waves and turbulence in the context of solar coronal heating, there are a number of reported results on plasma motions in the corona/solar wind. Plasma motions in the corona between $(1-2)\,R_\odot$ are normally detected using excess (i.e., larger than what would be from thermal motion of the emitting ion) broadening of emission lines from minor ions, and have velocities comparable to those required to realize the observed level of frequency broadening of radio sources. It should be noted that the non-thermal broadening is proportional to the line-of-sight speed (i.e. along the \bot_1 direction), as distinct from the speeds inferred from frequency broadening measurements, which are predominantly along the \bot_2 direction, perpendicular to the line of sight. The similar values of velocity thus suggest azimuthal symmetry in the velocity distribution perpendicular to the radial direction, i.e., to the magnetic field.

It is interesting to note that there is a broad agreement among the turbulent velocities inferred from interplanetary scintillation measurements (e.g., Ekers and Little 1971; Armstrong and Woo 1981). Our average values are somewhat smaller, with perpendicular velocities mostly below $100~{\rm km~s^{-1}}$, with a marginal decrease in speed towards the Sun. Importantly, our results, like those associated with previously reported measurements, show a large spread of values (10-200 km s⁻¹), re-emphasizing a high level of variability of the turbulence level in the solar corona.

Scattering of radio waves requires plasma density fluctuations, which could either be oscillatory in nature or carried by bulk plasma motions. Perpendicular large-scale motions (at scales much larger than the density fluctuation wavelength) could be random torsional or kink (e.g., Alfvén) waves that move around small scale fluctuations. In a turbulent plasma, the spectral broadening may also be associated with large-scale advection of eddies in a Kolmogorov turbulent cascade (e.g., Tennekes 1975). Quasi-parallel motions or waves parallel to the magnetic field with a speed

comparable to the sound (or ion thermal) speed would also produce a similar frequency broadening. Wexler et al. (2019) has interpreted the broadening as due to sound waves. If ion-sound waves are present, one can calculate the energy deposited to ions via Landau damping for a Maxwellian plasma, and we find a value of order 10^{11} erg g⁻¹ s⁻¹, comparable to the heating required to sustain a million-degree corona (e.g., Hollweg 1986; Cranmer and van Ballegooijen 2005).

Sound waves do not necessarily propagate from the low atmosphere, but could instead be locally generated via parametric decay of Alfvén waves. (e.g., Sagdeev and Galeev 1969; Del Zanna et al. 2001). Alternatively, sound waves could be a byproduct of MHD turbulence cascade (e.g., Goldreich and Sridhar 1995; Bian et al. 2010). Since the value of $\overline{q\,\epsilon^2}$ depends mostly on the level of density fluctuations near the ion-scale break scale $q_i^{-1} \sim c/\omega_{pi}$ (Kontar et al. 2023), the parallel-propagating ion-sound waves resonate mostly with protons and should be strongly Landau damped. This suggests that a constant re-supply of ion-sound waves is required, probably via the aforementioned parametric decay of Alfvén waves and/or the turbulent cascade. Interestingly, the estimate of Kolmogorov cascade power using large scale motions v_{\perp}^3/ℓ_{\perp} (at the outer scales ℓ_{\perp}) is consistent with the power that could be dissipated via ion-sound waves at inner scales q_i^{-1} , suggesting that ion-sound waves (or slow MHD mode waves) can act as an intermediate in the coronal heating chain and thus serve as a valuable diagnostic of ion heating in the solar corona.

Chapter 5

Conclusions and Closing Remarks

The aim of this thesis was to better understand the physical mechanisms driving solar radio emission, as well as the impact of turbulence in the solar corona on radio wave propagation. Chapters 2-3 investigate the transport of electron beams exciting type III solar radio bursts. Chapter 4 turns its attention to the characteristic velocities and density fluctuations in the solar corona and solar wind, derived using frequency broadening measurements.

Chapter 2 takes into account the finite size of electron beams to develop an analytical model of electron transport in type III solar radio bursts. The advection-nonlinear-diffusion equation derived in this chapter implies an electron beam propagating at a constant speed of $(v_0 + v_{\min})/2$, where v_0 and v_{\min} are respectively the maximum and minimum electron velocities in the beam, while exhibiting ballistic expansion, with their spatial width growing proportionally to time $(\propto t)$ at large distances $(x \gg d)$, where d is the initial beam size). This super-diffusion behavior contrasts with the

standard linear diffusion case ($\propto \sqrt{t}$) and explains the observed spatial characteristics of type III bursts. In particular, the model predicts a decrease in peak beam density proportional to 1/x, in agreement to the observed 1/x decrease in spectral energy density of Langmuir waves that produce radio emissions.

Chapter 3 analyses data from four type III bursts observed simultaneously by the PSP, STEREO-A, SolO and Wind spacecraft, to obtain the speeds and accelerations of type III exciters from simple and isolated type III solar bursts. For the first time, four simultaneous spacecraft observations allow to determine positions, and correct the resulting velocities and accelerations for the location between the spacecraft and the apparent source, revealing exciter velocities decreasing as $u(f) \propto f^{0.32\pm0.12}$. A simple gas-dynamic description of the electron beam moving through plasma with monotonically decreasing density predicts that the beam velocity decreases as $u(f) \propto f^{1/4}(r)$, so the acceleration changes $\propto r^{-1.58}$ (and speed as $\propto r^{-0.29}$) for the plasma density profile $n(r) \propto r^{-2.3}$. The measured velocity decreases with distance ($\beta_H \sim \beta_F \sim -0.37 \pm 0.15$) aligns well with previous studies and supports the model's predictions. Most significantly, the observed exciter acceleration decreases with heliocentric distance as $a(r) \propto r^{-1.71 \pm 0.20}$, matching the theoretical prediction of $a(r) \propto r^{-1.58}$. These findings support the hypothesis that interactions between beam-plasma structures and density inhomogeneities drive the deceleration of type III burst exciters, in agreement with numerical predictions from earlier studies. The observed differences in drift-rates between different spacecraft suggest that the temporal characteristics of the observed signals are affected by radio wave scattering off density inhomogeneities, pointing to propagation effects beyond the intrinsic properties of the exciter.

Chapter 4 uses frequency broadening measurements to deduce characteristic velocities in the solar corona and solar wind, revealing a remarkably coherent picture of density turbulence levels and bulk flow speeds. At distances beyond $10 R_{\odot}$, flow velocities are dominated by the solar wind. The anisotropy of density fluctuations emerges as a critical factor, with $\alpha = 1$ leading to slower sub-solar-wind speeds. Alternatively, the required level of density fluctuations would need to be much lower than those inferred from other observations. Closer to the Sun $(r \lesssim 10 R_{\odot})$, significant velocities of (20-70) km s⁻¹ in the perpendicular direction, or (100-300) km s⁻¹ in the parallel direction, are required to explain frequency broadening observations. If interpreted as Alfvén wave amplitudes, the perpendicular velocity measurements reveal the energy transferred in the turbulent cascade from large to small scales, ultimately deposited in the low corona and solar wind. Parallel velocities could be due to ion-sound waves, which, assuming a Maxwellian plasma, would deposit energy to ions via Landau damping at a rate of approximately 10^{11} erg g^{-1} s⁻¹, comparable to the heating required to sustain the million-degree corona. In the presence of non-Maxwellian velocity distributions, the actual damping and associated heating are expected to be weaker. Such waves could be locally generated through parametric decay of Alfvén waves or from the MHD turbulence cascade, serving as an intermediate step in the coronal heating process.

5.1 Closing Remarks

The results presented in this thesis show that the finite size of electron beams leads to a super-diffusive expansion, rather than the standard diffusive behavior, aligning well with observations and offering a more accurate description of beam evolution over large distances. Furthermore, multi-spacecraft observations have, for the first time, allowed for detailed corrections for source location effects, leading to reliable

measurements of exciter speeds and accelerations. The results confirmed that interactions with plasma density inhomogeneities can contribute significantly to beam deceleration and that propagation effects, such as radio-wave scattering, can significantly alter observed drift rates and source characteristics. The last chapter uses frequency broadening measurements to estimate characteristic velocities in the solar corona and solar wind. The results suggest that Alfvén wave turbulent cascade and damping of ion sound waves could play a crucial role in coronal heating.

Appendices

A Diffusion Tensor: Moving Density Fluctuations

A.1 Parallel Waves

Consider density fluctuations moving along the \parallel direction, i.e., $\Omega(\mathbf{q})=v_{\parallel}\,q_{\parallel}$. Then from Equation (4.12), and referring to Figure 4.1, we find

$$D_{\parallel\parallel} = \frac{\pi \omega_{pe}^4}{4 \,\omega^2} \,\alpha^3 \int_{\tilde{q}=0}^{\infty} \int_{\phi=0}^{2\pi} \int_{\mu=-1}^{1} \tilde{q}^2 \,(1-\mu^2) \cos^2\phi \,S(\tilde{q}) \,\delta\left(\tilde{v}_{\parallel} \,\tilde{q} \,\sqrt{1-\mu^2} \,\cos\phi - \tilde{q} \,\tilde{v}_g \,\mu\right) \,\frac{\tilde{q}^2 \,d\tilde{q} \,d\mu \,d\phi}{(2\pi)^3} , \tag{1}$$

$$D_{\perp_{2}\perp_{2}} = \frac{\pi\omega_{pe}^{4}}{4\omega^{2}} \alpha \int_{\tilde{q}=0}^{\infty} \int_{\phi=0}^{2\pi} \int_{\mu=-1}^{1} \tilde{q}^{2} (1-\mu^{2}) \sin^{2}\phi \, S(\tilde{q}) \, \delta\left(\tilde{v}_{\parallel} \, \tilde{q} \, \sqrt{1-\mu^{2}} \, \cos\phi - \tilde{q} \, \tilde{v}_{g} \, \mu\right) \, \frac{\tilde{q}^{2} \, d\tilde{q} \, d\mu \, d\phi}{(2\pi)^{3}} , \qquad (2)$$

and

$$D_{\perp_{1}\perp_{1}} = \frac{\pi\omega_{pe}^{4}}{4\omega^{2}} \alpha \int_{\tilde{q}=0}^{\infty} \int_{\phi=0}^{2\pi} \int_{\mu=-1}^{1} \tilde{q}^{2} \mu^{2} S(\tilde{q}) \delta\left(\tilde{v}_{\parallel}\sqrt{1-\mu^{2}}\,\tilde{q}\,\cos\phi - \tilde{q}\,\tilde{v}_{g}\,\mu\right) \frac{\tilde{q}^{2}\,d\tilde{q}\,d\mu\,d\phi}{(2\pi)^{3}} . \tag{3}$$

Noting that $\tilde{\mathbf{v}} = (\alpha \, v_{\parallel}, v_{\perp_2}, v_{\perp_1})$, the delta function can be expanded using the roots of $g(\mu) = A\sqrt{1-\mu^2} - \mu$, where $A = \left(\tilde{v}_{\parallel}/\tilde{v}_g\right)\cos\phi \simeq \alpha \, \left(v_{\parallel}/c\right)\cos\phi$, into

$$\delta\left(A\sqrt{1-\mu^2}\,-\mu\right) = \frac{1}{1+A^2}\,\delta\left(\mu - \frac{A}{\sqrt{1+A^2}}\right).$$

Thus, integrating over μ and retaining up to $\mathcal{O}(A^2)$ terms, we obtain

$$D_{\parallel\parallel} \simeq \frac{\pi \omega_{pe}^{4}}{4 \omega^{2} c} \alpha^{3} \int_{\tilde{q}=0}^{\infty} \int_{\phi=0}^{2\pi} \tilde{q} \left(1 - 2 \frac{\tilde{v}_{\parallel}^{2}}{c^{2}} \cos^{2} \phi\right) \cos^{2} \phi S(\tilde{q}) \frac{\tilde{q}^{2} d\tilde{q} d\phi}{(2\pi)^{3}} =$$

$$= \frac{\pi \omega_{pe}^{4}}{16 \omega^{2} c} \alpha^{2} \left(1 - \frac{3}{2} \alpha^{2} \frac{v_{\parallel}^{2}}{c^{2}}\right) \overline{q \epsilon^{2}} ,$$
(4)

$$D_{\perp_{2}\perp_{2}} = \frac{\pi\omega_{pe}^{4}}{4\,\omega^{2}\,c}\,\alpha\,\int_{\tilde{q}=0}^{\infty}\int_{\phi=0}^{2\pi}\tilde{q}\,\left(1-2\,\frac{\tilde{v_{\parallel}}^{2}}{c^{2}}\cos^{2}\phi\right)\,\sin^{2}\phi\,S(\tilde{q})\,\frac{\tilde{q}^{2}\,d\tilde{q}\,d\phi}{(2\pi)^{3}} = \\ = \frac{\pi\omega_{pe}^{4}}{16\,\omega^{2}\,c}\,\left(1-\frac{1}{2}\,\alpha^{2}\,\frac{v_{\parallel}^{2}}{c^{2}}\right)\,\overline{q\,\epsilon^{2}}\,\,, \tag{5}$$

and

$$D_{\perp_1 \perp_1} = \frac{\pi \omega_{pe}^4}{4 \,\omega^2 \,c} \,\alpha \, \int_{\tilde{q}=0}^{\infty} \int_{\phi=0}^{2\pi} \tilde{q} \, \left(\frac{\tilde{v}_{\parallel}^2}{c^2} \cos^2 \phi\right) \, S(\tilde{q}) \, \frac{\tilde{q}^2 \, d\tilde{q} \, d\phi}{(2\pi)^3} = \alpha^2 \, \frac{v_{\parallel}^2}{c^2} \, \frac{\pi \omega_{pe}^4}{16 \,\omega^2 \,c} \, \overline{q \,\epsilon^2} \, \, . \tag{6}$$

These are the modified scattering rate expressions. However, the corrections are generally small since $v_\parallel^2/c^2\ll 1$.

Further, because $\int_0^{2\pi} \sin \phi \, d\phi = 0$, $\int_0^{2\pi} \cos \phi \, d\phi = 0$, and $\int_0^{2\pi} \sin \phi \, \cos \phi \, d\phi = 0$, we have, respectively,

$$D_{\perp_1 \perp_2} = D_{\perp_2 \perp_1} = 0;$$
 $D_{\parallel \perp_1} = D_{\perp_1 \parallel} = 0;$ $D_{\parallel \perp_2} = D_{\perp_2 \parallel} = 0.$ (7)

Thus the diffusion tensor has the form

$$\mathbf{D} = \frac{\pi \omega_{pe}^4}{16 \,\omega^2 \,c} \,\, \overline{q \,\epsilon^2} \,\, \mathrm{diag} \left(\alpha^2 \, \left[1 - \frac{3}{2} \,\alpha^2 \, \frac{v_{\parallel}^2}{c^2} \right], \, 1 - \frac{1}{2} \,\alpha^2 \, \frac{v_{\parallel}^2}{c^2}, \, \alpha^2 \, \frac{v_{\parallel}^2}{c^2} \right) \,\,. \tag{8}$$

Both \parallel and \perp_2 directions are perpendicular to the wavevector \mathbf{k} in this analysis. Hence, for $\Delta\mathbf{k} \perp \mathbf{k}$ and hence the scattering corresponding to the $\perp_2 \perp_2$ and $\parallel \parallel$ terms is elastic. The change to the absolute value of $|\mathbf{k}|$, or equivalently the wave frequency $\omega(\mathbf{k}) \simeq c|\mathbf{k}|$, comes from the term $D_{\perp_1 \perp_1} \propto d \left\langle \Delta k_{\perp_1}^2 \right\rangle / dt \neq 0$. Henceforth, we can write

$$\mathbf{D} = \frac{\pi \omega_{pe}^4}{16 \,\omega^2 \,c} \,\overline{q \,\epsilon^2} \,\operatorname{diag}\left(\alpha^2, 1, \frac{\alpha^2 \,v_{\parallel}^2}{c^2}\right) \ . \tag{9}$$

A.2 Perpendicular Waves

For the case of waves moving in the \bot_2 direction, i.e., $\Omega(\mathbf{q}) = v_{\bot_2}q_{\bot_2}$, the same formalism can be applied here, with $A = (\tilde{v}_{\bot_2}/\tilde{v}_g) \sin \phi \simeq (v_{\bot_2}/c) \sin \phi$, to obtain

$$D_{\parallel\parallel} \simeq \frac{\pi \omega_{pe}^4}{4 \,\omega^2 \,c} \,\alpha^3 \int_{\tilde{q}=0}^{\infty} \int_{\phi=0}^{2\pi} \tilde{q} \,\left(1 - 2 \,\frac{\tilde{v}_{\perp_2}^2}{c^2} \sin^2 \phi\right) \,\cos^2 \phi \,S(\tilde{q}) \,\frac{\tilde{q}^2 \,d\tilde{q} \,d\phi}{(2\pi)^3} = \\ = \frac{\pi \omega_{pe}^4}{16 \,\omega^2 \,c} \,\alpha^2 \,\left(1 - \frac{1}{2} \,\frac{{v_{\perp_2}}^2}{c^2}\right) \,\overline{q \,\epsilon^2} \,\,, \tag{10}$$

$$D_{\perp_{2}\perp_{2}} = \frac{\pi\omega_{pe}^{4}}{4\omega^{2}c} \alpha \int_{\tilde{q}=0}^{\infty} \int_{\phi=0}^{2\pi} \tilde{q} \left(1 - 2\frac{\tilde{v}_{\perp_{2}}^{2}}{c^{2}}\sin^{2}\phi\right) \sin^{2}\phi S(\tilde{q}) \frac{\tilde{q}^{2} d\tilde{q} d\phi}{(2\pi)^{3}} =$$

$$= \frac{\pi\omega_{pe}^{4}}{16\omega^{2}c} \left(1 - \frac{3}{2}\frac{v_{\perp_{2}}^{2}}{c^{2}}\right) \overline{q\epsilon^{2}} ,$$
(11)

and

$$D_{\perp_1 \perp_1} = \frac{\pi \omega_{pe}^4}{4 \,\omega^2 \,c} \,\alpha \int_{\tilde{q}=0}^{\infty} \int_{\phi=0}^{2\pi} \tilde{q} \,\left(\frac{\tilde{v}_{\perp_2}^2}{c^2} \sin^2 \phi\right) \,S(\tilde{q}) \,\frac{\tilde{q}^2 \,d\tilde{q} \,d\phi}{(2\pi)^3} = \frac{v_{\perp_2}^2}{c^2} \,\frac{\pi \omega_{pe}^4}{16 \,c \,\omega^2} \,\overline{q \,\epsilon^2} \,\,. \tag{12}$$

Again, because $\int_0^{2\pi} \sin \phi \, d\phi = 0$, $\int_0^{2\pi} \cos \phi \, d\phi = 0$, and $\int_0^{2\pi} \sin \phi \, \cos \phi \, d\phi = 0$, we have, respectively,

$$D_{\perp_1 \perp_2} = D_{\perp_2 \perp_1} = 0;$$
 $D_{\parallel \perp_1} = D_{\perp_1 \parallel} = 0;$ $D_{\parallel \perp_2} = D_{\perp_2 \parallel} = 0$. (13)

Thus, following the same reasoning as in Equation (8), the diffusion tensor for perpendicular motions takes the form

$$\mathbf{D} = \frac{\pi \omega_{pe}^4}{16 \,\omega^2 \,c} \,\overline{q \,\epsilon^2} \,\operatorname{diag}\left(\alpha^2, 1, \frac{v_{\perp_2}^2}{c^2}\right) \ . \tag{14}$$

B Diffusion Tensor: Random Motions

B.1 Random Motions Superimposed on a Static Background

Integrating Equation (4.18) in the approximation $q_{\perp_2}^2\langle v_{\perp_2}^2\rangle\ll q^2c^2$ and taking $\Omega=0$ yields

$$D_{\parallel\parallel} = \frac{\pi \omega_{pe}^{4}}{4 \omega^{2}} \alpha^{3} \int_{\tilde{q}=0}^{\infty} \int_{\phi=0}^{2\pi} \int_{\mu=-1}^{1} \tilde{q}^{2} (1 - \mu^{2}) \cos^{2} \phi S(\tilde{q}) \frac{1}{\sqrt{2\pi \, \tilde{q}_{\perp_{2}}^{2} \langle \tilde{v}_{\perp_{2}}^{2} \rangle}} \exp \left[-\frac{(\tilde{q} \, c \, \mu)^{2}}{2 \, \tilde{q}_{\perp_{2}}^{2} \langle \tilde{v}_{\perp_{2}}^{2} \rangle} \right] \frac{d\mu \, d\phi \, \tilde{q}^{2} d\tilde{q}}{(2\pi)^{3}} =$$

$$= \frac{\pi \omega_{pe}^{4}}{16 \, \omega^{2} \, c} \alpha^{2} \left(1 - \frac{1}{4} \frac{\langle v_{\perp_{2}}^{2} \rangle}{c^{2}} \right) \, \overline{q \, \epsilon^{2}} \,, \tag{15}$$

where we have used the substitution $\xi=\mu\,c/\sqrt{\langle \tilde{v}_{\perp_2}^2\rangle}$, approximated $q_{\perp_2}^2\approx q^2\sin^2\chi$ and made use of the formula $\int_{-\infty}^\infty \xi^2\exp\left(-b\,\xi^2\right)d\xi=\sqrt{\pi/4\,b^3}$. In the same way, we find

$$D_{\perp_{2}\perp_{2}} = \frac{\pi\omega_{pe}^{4}}{4\omega^{2}}\alpha \int_{\tilde{q}=0}^{\infty} \int_{\phi=0}^{2\pi} \int_{\mu=-1}^{1} \tilde{q}^{2} (1-\mu^{2}) \sin^{2}\phi S(\tilde{q}) \frac{1}{\sqrt{2\pi\,\tilde{q}_{\perp_{2}}^{2}\langle\tilde{v}_{\perp_{2}}^{2}\rangle}} \exp\left[-\frac{(\tilde{q}\,c\,\mu)^{2}}{2\,\tilde{q}_{\perp_{2}}^{2}\langle\tilde{v}_{\perp_{2}}^{2}\rangle}\right] \frac{d\mu\,d\phi\,\tilde{q}^{2}d\tilde{q}}{(2\pi)^{3}} = \frac{\pi\omega_{pe}^{4}}{16\,\omega^{2}\,c} \left(1-\frac{3}{4}\frac{\langle v_{\perp_{2}}^{2}\rangle}{c^{2}}\right) \overline{q\,\epsilon^{2}},$$
(16)

$$D_{\perp_{1}\perp_{1}} = \frac{\pi\omega_{pe}^{4}}{4\omega^{2}} \alpha \int_{\tilde{q}=0}^{\infty} \int_{\phi=0}^{2\pi} \int_{\mu=-1}^{1} \tilde{q}^{2} \mu^{2} S(\tilde{q}) \frac{1}{\sqrt{2\pi \, \tilde{q}_{\perp_{2}}^{2} \langle \tilde{v}_{\perp_{2}}^{2} \rangle}} \exp \left[-\frac{(\tilde{q} \, c \, \mu)^{2}}{2 \, \tilde{q}_{\perp_{2}}^{2} \langle \tilde{v}_{\perp_{2}}^{2} \rangle} \right] \frac{d\mu \, d\phi \, \tilde{q}^{2} d\tilde{q}}{(2\pi)^{3}} = \frac{\langle v_{\perp_{2}}^{2} \rangle}{c^{2}} \frac{\pi\omega_{pe}^{4}}{16 \, \omega^{2} \, c} \, \overline{q \, \epsilon^{2}} , \qquad (17)$$

and

$$D_{\perp_1\perp_2} = D_{\perp_2\perp_1} = 0;$$
 $D_{\parallel\perp_1} = D_{\perp_1\parallel} = 0;$ $D_{\parallel\perp_2} = D_{\perp_2\parallel} = 0.$ (18)

The components of the diffusion tensor for random motions ("turbulence") can then be approximated as

$$\mathbf{D} = \frac{\pi \omega_{pe}^4}{16 \,\omega^2 \,c} \,\overline{q \,\epsilon^2} \,\operatorname{diag}\left(\alpha^2, 1, \frac{\langle v_{\perp_2}^2 \rangle}{c^2}\right) \ . \tag{19}$$

B.2 Random Motions Superimposed on Flows in a General Direction

Here we consider random motions superimposed on flows in a general direction perpendicular to k. For this purpose we can use the general result

$$\int_{\xi = -\infty}^{\infty} B \, \xi^2 \, \exp\left(-\frac{B^2}{2}(\xi - A)^2\right) d\xi = B \, \int_{\eta = -\infty}^{\infty} (A + \eta)^2 \, \exp\left(-\frac{B^2}{2}\eta^2\right) d\eta =$$

$$= B \int_{\eta = -\infty}^{\infty} (A^2 + \eta^2 + 2A\eta) \exp\left(-\frac{B^2}{2}\eta^2\right) d\eta = \sqrt{2\pi} \left(A^2 + \frac{1}{B^2}\right)$$
 (20)

to compute the components of the diffusion tensor.

We first consider radially propagating density fluctuations, with $\Omega(\mathbf{q}) = v_{\parallel} q_{\parallel}$. If we add random motions in the same direction we can evaluate the $D_{\perp_1 \perp_1}$ term that contributes to the frequency broadening:

$$D_{\perp_{1}\perp_{1}} = \frac{\pi\omega_{pe}^{4}}{4\omega^{2}} \alpha \int_{\tilde{q}=0}^{\infty} \int_{\phi=0}^{2\pi} \int_{\mu=-1}^{1} \tilde{q}^{2} \mu^{2} S(\tilde{q}) \frac{1}{\sqrt{2\pi \, \tilde{q}_{\parallel}^{2} \langle \tilde{v}_{\parallel}^{2} \rangle}} \exp \left[-\frac{(\tilde{q} \, c \, \mu - \tilde{q}_{\parallel} \tilde{v}_{\parallel})^{2}}{2 \, \tilde{q}_{\parallel}^{2} \langle \tilde{v}_{\parallel}^{2} \rangle} \right] \frac{d\mu \, d\phi \, \tilde{q}^{2} d\tilde{q}}{(2\pi)^{3}} = \frac{\pi\omega_{pe}^{4}}{16\omega^{2} \, c} \frac{q \, c^{2} \alpha^{2} (v_{\parallel}^{2} + \langle v_{\parallel}^{2} \rangle)}{c^{2}} , \qquad (21)$$

where we have approximated $\tilde{q}_{\parallel}^2 \approx \tilde{q}^2 \cos^2 \phi$, made use of the substitution $\mu = \xi \sqrt{\langle \tilde{v}_{\parallel}^2 \rangle} / c$, and used Equation (20).

If we then consider propagation and random motions that are both in the direction perpendicular to the solar radius vector, with dispersion relation $\Omega(\mathbf{q})=v_{\perp_2}\,q_{\perp_2}$, we find

$$D_{\perp_{1}\perp_{1}} = \frac{\pi\omega_{pe}^{4}}{4\omega^{2}}\alpha \int_{\tilde{q}=0}^{\infty} \int_{\phi=0}^{2\pi} \int_{\mu=-1}^{1} \tilde{q}^{2}\mu^{2}S(\tilde{q}) \frac{1}{\sqrt{2\pi\,\tilde{q}_{\perp_{2}}^{2}\langle\tilde{v}_{\perp_{2}}^{2}\rangle}} \exp\left[-\frac{(\tilde{q}\,c\,\mu - \tilde{q}_{\perp_{2}}\tilde{v}_{\perp_{2}})^{2}}{2\,\tilde{q}_{\perp_{2}}^{2}\langle\tilde{v}_{\perp_{2}}^{2}\rangle}\right] \frac{d\mu\,d\phi\,\tilde{q}^{2}d\tilde{q}}{(2\pi)^{3}} = \frac{\pi\omega_{pe}^{4}}{16\,\omega^{2}\,c}\,\overline{q}\,\epsilon^{2}\,\frac{v_{\perp_{2}}^{2} + \langle v_{\perp_{2}}^{2}\rangle}{c^{2}},$$
(22)

where we have made use of the substitution $\mu = \xi \sqrt{\langle \tilde{v}_{\perp_2}^2 \rangle} / c$, approximated $\tilde{q}_{\perp_2}^2 \approx \tilde{q}^2 \sin^2 \chi$, and used Equation (20).

If both parallel and perpendicular contributions are taken into account, the diffusion tensor takes the form

$$\mathbf{D} = \frac{\pi \omega_{pe}^4}{16 \,\omega^2 \,c} \,\overline{q \,\epsilon^2} \,\operatorname{diag}\left(\alpha^2, 1, \frac{\alpha^2 \left(v_{\parallel}^2 + \langle v_{\parallel}^2 \rangle\right) + v_{\perp_2}^2 + \langle v_{\perp_2}^2 \rangle}{c^2}\right) \ . \tag{23}$$

Since steady flows (v^2) and random motions $(\langle v^2 \rangle)$ contribute equally, we can rewrite this as simply

$$\mathbf{D} = \frac{\pi \omega_{pe}^4}{16\,\omega^2\,c}\,\overline{q\,\epsilon^2}\,\operatorname{diag}\left(\alpha^2, 1, \frac{\alpha^2\,\langle v_\parallel^2\rangle + \langle v_{\perp 2}^2\rangle}{c^2}\right) \ , \tag{24}$$

where now $\langle \cdots \rangle$ includes both steady and random flows, in the parallel or perpendicular directions, respectively.

Bibliography

- Abramowitz, Milton and Irene A. Stegun (1970). *Handbook of mathematical functions* : with formulas, graphs, and mathematical tables. U.S. Dept. of Commerce, National Bureau of Standards.
- Akbari, Hassanali, James W. LaBelle and David L. Newman (Mar. 2021). 'Langmuir Turbulence in the Auroral Ionosphere: Origins and Effects'. In: *Frontiers in Astronomy and Space Sciences* 7, 116, p. 116. DOI: 10.3389/fspas.2020.617792.
- Akhiezer, A. I., I. G. Prokhoda and A. G. Sitenko (Jan. 1958). 'Scattering of Electromagnetic Waves in a Plasma'. In: *Soviet Journal of Experimental and Theoretical Physics* 6, p. 576.
- Alexandrova, O. et al. (Dec. 2012). 'Solar Wind Turbulent Spectrum at Plasma Kinetic Scales'. In: *ApJ* 760.2, 121, p. 121. doi: 10.1088/0004-637X/760/2/121. arXiv: 1212.0412 [astro-ph.SR].
- Alexandrova, O. et al. (Oct. 2013). 'Solar Wind Turbulence and the Role of Ion Instabilities'. In: *SSRv* 178, pp. 101–139. DOI: 10.1007/s11214-013-0004-8. arXiv: 1306.5336 [astro-ph.SR].
- Alfvén, H. (Oct. 1942). 'Existence of Electromagnetic-Hydrodynamic Waves'. In: *Nature* 150.3805, pp. 405–406. doi: 10.1038/150405d0.
- (Jan. 1947). 'Magneto hydrodynamic waves, and the heating of the solar corona'.
 In: MNRAS 107, p. 211. DOI: 10.1093/mnras/107.2.211.

Allen, C. W. (Jan. 1947). 'Interpretation of Electron Densities from Corona Brightness'. In: *MNRAS* 107, p. 426. DOI: 10.1093/mnras/107.5-6.426.

- Alvarez, H. and F. T. Haddock (May 1973a). 'Decay Time of Type III Solar Bursts Observed at Kilometric Wavelengths'. In: *SoPh* 30, pp. 175–182. DOI: 10 . 1007 / BF00156186.
- Alvarez, Hector and F. T. Haddock (Mar. 1973b). 'Solar Wind Density Model from km-Wave Type III Bursts'. In: *SoPh* 29.1, pp. 197–209. DOI: 10.1007/BF00153449.
- Anantharamaiah, K. R., P. Gothoskar and T. J. Cornwell (Dec. 1994). 'Radio synthesis imaging of anisotropic angular broadening in the solar wind.' In: *Journal of Astrophysics and Astronomy* 15, pp. 387–414. DOI: 10.1007/BF02714823.
- Andrews, M. D. (Dec. 2003). 'A Search for CMEs Associated with Big Flares'. In: *SoPh* 218.1, pp. 261–279. DOI: 10.1023/B:SOLA.0000013039.69550.bf.
- Armstrong, J. W. and W. A. Coles (Jan. 1972). 'Analysis of three-station interplanetary scintillation'. In: *J. Geophys. Res.* 77.25, p. 4602. DOI: 10.1029/JA077i025p04602.
- Armstrong, J. W. and R. Woo (Nov. 1981). 'Solar wind motion within 30 R solar masses Spacecraft radio scintillation observations'. In: *A&A* 103.2, pp. 415–421.
- Armstrong, J. W. et al. (Jan. 1986). 'Solar Wind Observations Near the Sun'. In: *The Sun and the Heliosphere in Three Dimensions*. Ed. by R. G. Marsden and L. A. Fisk. Vol. 123, p. 59. DOI: 10.1007/978-94-009-4612-5_7.
- (Aug. 1990). 'Observations of Field-aligned Density Fluctuations in the Inner Solar Wind'. In: *ApJ* 358, p. 685. doi: 10.1086/169022.
- Arzner, K. and A. Magun (Nov. 1999). 'Radiowave propagation in a statistically inhomogeneous plasma'. In: A&A 351, pp. 1165–1189.
- Aschwanden, M. J. et al. (Dec. 1995). 'Solar Electron Beams Detected in Hard X-Rays and Radio Waves'. In: *ApJ* 455, pp. 347–+. doi: 10.1086/176582.
- Aschwanden, Markus J. (2004). Physics of the Solar Corona. An Introduction.

Azzollini, Francesco and Eduard P. Kontar (2025). 'A Multispacecraft Analysis and Modeling of Type III Radio Burst Exciter Deceleration in Inhomogeneous Heliospheric Plasma'. In: *The Astrophysical Journal* 989.1, p. 118. doi: 10.3847/1538-4357/adee22. URL: https://dx.doi.org/10.3847/1538-4357/adee22.

- Azzollini, Francesco et al. (June 2024). 'Plasma Motions and Compressive Wave Energetics in the Solar Corona and Solar Wind from Radio Wave Scattering Observations'. In: *ApJ* 968.2, 72, p. 72. doi: 10.3847/1538-4357/ad4154. arXiv: 2403.12680 [astro-ph.SR].
- Bale, S. D. et al. (Apr. 2008). 'The Electric Antennas for the STEREO/WAVES Experiment'. In: *SSRv* 136.1-4, pp. 529–547. DOI: 10.1007/s11214-007-9251-x.
- Bale, S. D. et al. (Dec. 2016). 'The FIELDS Instrument Suite for Solar Probe Plus. Measuring the Coronal Plasma and Magnetic Field, Plasma Waves and Turbulence, and Radio Signatures of Solar Transients'. In: *SSRv* 204.1-4, pp. 49–82. DOI: 10.1007/s11214-016-0244-5.
- Banerjee, D., D. Pérez-Suárez and J. G. Doyle (July 2009). 'Signatures of Alfvén waves in the polar coronal holes as seen by EIS/Hinode'. In: *A&A* 501.3, pp. L15–L18. DOI: 10.1051/0004-6361/200912242. arXiv: 0906.4600 [astro-ph.SR].
- Banerjee, D. et al. (Nov. 1998). 'Broadening of SI VIII lines observed in the solar polar coronal holes'. In: *A&A* 339, pp. 208–214.
- Bardwell, S. and M. V. Goldman (Nov. 1976). 'Three-dimensional Langmuir wave instabilities in type III solar radio bursts.' In: *ApJ* 209, pp. 912–926. doi: 10.1086/154790.
- Baselian, L. L. et al. (Nov. 1974). 'Frequency and Time Splitting of Decameter Solar Radio Bursts. I.: Elementary Events'. In: *SoPh* 39.1, pp. 213–222. DOI: 10 . 1007 / BF00154982.
- Bemporad, A. and L. Abbo (June 2012). 'Spectroscopic Signature of Alfvén Waves Damping in a Polar Coronal Hole up to 0.4 Solar Radii'. In: *ApJ* 751.2, 110, p. 110. DOI: 10.1088/0004-637X/751/2/110. arXiv: 1204.2544 [astro-ph.SR].

Benz, Arnold O. (Dec. 2017). 'Flare Observations'. In: *Living Reviews in Solar Physics* 14.1, 2, p. 2. Doi: 10.1007/s41116-016-0004-3.

- Bian, N. H., A. G. Emslie and E. P. Kontar (2019). 'A Fokker-Planck Framework for Studying the Diffusion of Radio Burst Waves in the Solar Corona'. In: *ApJ* 873.1, 33, p. 33. DOI: 10.3847/1538-4357/ab0411. arXiv: 1902.00239 [astro-ph.SR].
- Bian, N. H., E. P. Kontar and J. C. Brown (Sept. 2010). 'Parallel electric field generation by Alfvén wave turbulence'. In: *A&A* 519, A114+. DOI: 10.1051/0004-6361/201014048. arXiv: 1006.2662 [astro-ph.SR].
- Blesing, R. G. and P. A. Dennison (Mar. 1972). 'Coronal Broadening of the Crab Nebula 1969-71: Observations'. In: *PASA* 2.2, pp. 84–86. doi: 10.1017/S1323358000012947.
- Bougeret, J. L., J. H. King and R. Schwenn (Feb. 1984). 'Solar Radio Burst and In-Situ Determination of Interplanetary Electron Density'. In: *SoPh* 90.2, pp. 401–412. DOI: 10.1007/BF00173965.
- Bougeret, J. L. et al. (Feb. 1995). 'Waves: The Radio and Plasma Wave Investigation on the Wind Spacecraft'. In: *SSRv* 71.1-4, pp. 231–263. DOI: 10.1007/BF00751331.
- Bougeret, J. L. et al. (2008). 'S/WAVES: The Radio and Plasma Wave Investigation on the STEREO Mission'. In: *SSRv* 136.1-4, pp. 487–528. DOI: 10.1007/s11214-007-9298-8.
- Bradford, H. M. and D. Routledge (Mar. 1980). 'Coronal occultation of Voyager 2, 1979 August'. In: MNRAS 190, 73P–77P. DOI: 10.1093/mnras/190.1.73P.
- Bruno, Roberto and Vincenzo Carbone (Dec. 2013). 'The Solar Wind as a Turbulence Laboratory'. In: *Living Reviews in Solar Physics* 10.1, 2, p. 2. doi: 10.12942/lrsp-2013-2.
- Bunting, Kaine A. et al. (Jan. 2024). 'Constraints on Solar Wind Density and Velocity Based on Coronal Tomography and Parker Solar Probe Measurements'. In: *ApJ* 961.1, 64, p. 64. doi: 10.3847/1538-4357/ad1506.
- Cecconi, B. et al. (Apr. 2008). 'STEREO/Waves Goniopolarimetry'. In: *SSRv* 136.1-4, pp. 549–563. doi: 10.1007/s11214-007-9255-6.

Cecconi, Baptiste (May 2014). 'Goniopolarimetry: Space-borne radio astronomy with imaging capabilities'. In: *Comptes Rendus Physique* 15.5, pp. 441–447. doi: 10.1016/j.crhy.2014.02.005.

- Celnikier, L. M., L. Muschietti and M. V. Goldman (July 1987). 'Aspects of interplanetary plasma turbulence'. In: *A&A* 181.1, pp. 138–154.
- Celnikier, L. M. et al. (Oct. 1983). 'A determination of the electron density fluctuation spectrum in the solar wind, using the ISEE propagation experiment'. In: *A&A* 126.2, pp. 293–298.
- Chandrasekhar, T. et al. (Jan. 1991). 'Fabry-Pérot line profiles in the $\lambda 5303$ å and $\lambda 6374$ å coronal lines obtained during the 1983 Indonesian eclipse'. In: *SoPh* 131.1, pp. 25–39. doi: 10.1007/BF00151741.
- Che, H. et al. (Feb. 2017). 'How electron two-stream instability drives cyclic Langmuir collapse and continuous coherent emission'. In: *Proceedings of the National Academy of Science* 114, pp. 1502–1507. DOI: 10.1073/pnas.1614055114. arXiv: 1702.00784 [physics.space-ph].
- Chen, Naihwa, Wing-Huen Ip and Davina Innes (June 2013). 'Flare-Associated Type III Radio Bursts and Dynamics of the EUV Jet from SDO/AIA and RHESSI Observations'. In: *ApJ* 769.2, 96, p. 96. doi: 10.1088/0004-637X/769/2/96. arXiv: 1304.2907 [astro-ph.SR].
- Chen, P. F. (Dec. 2011). 'Coronal Mass Ejections: Models and Their Observational Basis'. In: *Living Reviews in Solar Physics* 8.1, 1, p. 1. DOI: 10.12942/lrsp-2011-1.
- Chen, Xingyao et al. (Dec. 2020). 'Subsecond Time Evolution of Type III Solar Radio Burst Sources at Fundamental and Harmonic Frequencies'. In: *ApJ* 905.1, 43, p. 43. DOI: 10.3847/1538-4357/abc24e. arXiv: 2010.08782 [astro-ph.SR].
- Chen, Xingyao et al. (Dec. 2023). 'Source positions of an interplanetary type III radio burst and anisotropic radio-wave scattering'. In: *A&A* 680, A1, A1. DOI: 10.1051/0004-6361/202347185. arXiv: 2306.09160 [astro-ph.SR].

Clarkson, Daniel L. et al. (Apr. 2025). 'Tracing the heliospheric magnetic field via anisotropic radio-wave scattering'. In: *Scientific Reports* 15.1, 11335, p. 11335. DOI: 10.1038/s41598-025-95270-w. arXiv: 2503.22553 [astro-ph.SR].

- Coles, W. A. and J. K. Harmon (Feb. 1989). 'Propagation Observations of the Solar Wind near the Sun'. In: *ApJ* 337, p. 1023. DOI: 10.1086/167173.
- Contesse, L., S. Koutchmy and C. Viladrich (Aug. 2004). 'Analysis of non-thermal velocities in the solar corona'. In: *Annales Geophysicae* 22.8, pp. 3055–3062. DOI: 10. 5194/angeo-22-3055-2004.
- Coste, J. et al. (June 1975). 'Propagation of an unstable spectrum of plasmons in the presence of random inhomogeneities'. In: *Physics of Fluids* 18.6, pp. 679–691. DOI: 10.1063/1.861192.
- Cranmer, S. R. and A. A. van Ballegooijen (Feb. 2005). 'On the Generation, Propagation, and Reflection of Alfvén Waves from the Solar Photosphere to the Distant Heliosphere'. In: *ApJS* 156.2, pp. 265–293. DOI: 10.1086/426507. arXiv: astro-ph/0410639 [astro-ph].
- de La Noe, J. (Oct. 1975). 'Spectral characteristics of stria, split pair and triple bursts.' In: *A&A* 43.2, pp. 201–214.
- de La Noe, J. and A. Boischot (Aug. 1972). 'The Type III B Burst'. In: A&A 20, p. 55.
- De Moortel, I. et al. (Jan. 2016). 'Transverse, propagating velocity perturbations in solar coronal loops'. In: *Plasma Physics and Controlled Fusion* 58.1, 014001, p. 014001. DOI: 10.1088/0741-3335/58/1/014001. arXiv: 1510.00976 [astro-ph.SR].
- DeForest, C. E. and J. B. Gurman (July 1998). 'Observation of Quasi-periodic Compressive Waves in Solar Polar Plumes'. In: *ApJL* 501.2, pp. L217–L220. doi: 10.1086/311460.
- Del Zanna, L., M. Velli and P. Londrillo (Feb. 2001). 'Parametric decay of circularly polarized Alfvén waves: Multidimensional simulations in periodic and open domains'. In: *A&A* 367, pp. 705–718. DOI: 10.1051/0004-6361: 20000455.

Dennison, P. A. and R. G. Blesing (Mar. 1972). 'Coronal Broadening of the Crab Nebula 1969-71: Interpretation'. In: *Proceedings of the Astronomical Society of Australia* 2.2, pp. 86–88. doi: 10.1017/S1323358000012959.

- Dikpati, M. (Jan. 2004). 'The importance of the solar tachocline'. In: *35th COSPAR Scientific Assembly*. Vol. 35, p. 1198.
- Dąbrowski, Bartosz P. et al. (June 2016). 'Prospects for Solar and Space Weather Research with Polish Part of the LOFAR Telescope'. In: *Acta Geophysica* 64.3, pp. 825–840. DOI: 10.1515/acgeo-2016-0028.
- Dougherty, J. P. and D. T. Farley (Nov. 1960). 'A Theory of Incoherent Scattering of Radio Waves by a Plasma'. In: *Proceedings of the Royal Society of London Series A* 259.1296, pp. 79–99. DOI: 10.1098/rspa.1960.0212.
- Doyle, J. G., D. Banerjee and M. E. Perez (July 1998). 'Coronal line-width variations'. In: *SoPh* 181.1, pp. 91–101. DOI: 10.1023/A:1005019931323.
- Doyle, J. G., L. Teriaca and D. Banerjee (Sept. 1999). 'Coronal hole diagnostics out to $8R_{sun}$ '. In: A&A 349, pp. 956–960.
- Drummond, W. E. and D. Pines (July 1964). 'Nonlinear plasma oscillations'. In: *Annals of Physics* 28, pp. 478–499. DOI: 10.1016/0003-4916(64)90205-2.
- Dulk, G. A. et al. (Feb. 1987). 'The speeds of electrons that excite solar radio bursts of type III'. In: *A&A* 173.2, pp. 366–374.
- Dulk, George A. and Martin D. Altschuler (Nov. 1971). 'A Moving Type IV Radio Burst and Its Relation to the Coronal Magnetic Field'. In: *SoPh* 20.2, pp. 438–447. DOI: 10.1007/BF00159777.
- Efimov, A. I. et al. (Jan. 2002). 'East-West scattering level asymmetry of the solar corona'. In: *Advances in Space Research* 30.3, pp. 453–458. DOI: 10 . 1016 / S0273 1177(02)00335–6.
- Efimov, A. I. et al. (July 2008). 'Solar wind turbulence during the solar cycle deduced from Galileo coronal radio-sounding experiments'. In: *Advances in Space Research* 42.1, pp. 117–123. DOI: 10.1016/j.asr.2008.03.025.

Efimov, A. I. et al. (Jan. 2013). 'Frequency fluctuations of coherent signals from space-craft observed during dual-frequency radio sounding of the circumsolar plasma in 2004-2008'. In: *Cosmic Research* 51.1, pp. 13–22. DOI: 10.1134/S0010952513010036.

- Ekers, R. D. and L. T. Little (Jan. 1971). 'The Motion of the Solar Wind Close to the Sun'. In: *A&A* 10, p. 310.
- Ellis, G. R. A. (Apr. 1969). 'Fine structure in the spectra of solar radio bursts.' In: *Australian Journal of Physics* 22, p. 177. DOI: 10.1071/PH690177.
- Emslie, A. G., J. A. Miller and J. C. Brown (Feb. 2004). 'An Explanation for the Different Locations of Electron and Ion Acceleration in Solar Flares'. In: *ApJL* 602, pp. L69–L72. DOI: 10.1086/382350.
- Emslie, A. G. et al. (Nov. 2005). 'Refinements to flare energy estimates: A followup to "Energy partition in two solar flare/CME events" by A. G. Emslie et al.' In: *Journal of Geophysical Research* (*Space Physics*) 110.A9, A11103, p. 11103. DOI: 10 . 1029 / 2005JA011305.
- Emslie, A. G. et al. (Nov. 2012). 'Global Energetics of Thirty-eight Large Solar Eruptive Events'. In: *ApJ* 759, 71, p. 71. doi: 10.1088/0004-637X/759/1/71. arXiv: 1209.2654 [astro-ph.SR].
- Esser, Ruth et al. (Jan. 1999). 'Plasma Properties in Coronal Holes Derived from Measurements of Minor Ion Spectral Lines and Polarized White Light Intensity'. In: *ApJL* 510.1, pp. L63–L67. DOI: 10.1086/311786.
- Fainberg, J., Larry G. Evans and R. G. Stone (Nov. 1972). 'Radio Tracking of Solar Energetic Particles through Interplanetary Space'. In: *Science* 178.4062, pp. 743–745. DOI: 10.1126/science.178.4062.743.
- Fainberg, J., S. Hoang and R. Manning (Dec. 1985). 'Measurements of Distributed Polarized Radio Sources from Spinning Spacecraft Effect of a Tilted Axial Antenna ISEE-3 Application and Results'. In: *A&A* 153, p. 145.
- Fainberg, Joseph and R. G. Stone (Nov. 1970). 'Type III Solar Radio Burst Storms Observed at Low Frequencies.' In: *SoPh* 15.1, pp. 222–233. doi: 10.1007/BF00149487.

Fletcher, L. et al. (Sept. 2011). 'An Observational Overview of Solar Flares'. In: *SSRv* 159.1-4, pp. 19–106. doi: 10.1007/s11214-010-9701-8. arXiv: 1109.5932 [astro-ph.SR].

- Fox, N. J. et al. (Dec. 2016). 'The Solar Probe Plus Mission: Humanity's First Visit to Our Star'. In: *SSRv* 204.1-4, pp. 7–48. DOI: 10.1007/s11214-015-0211-6.
- Frank, Till D. (2009). 'Linear and Non-linear Fokker–Planck Equations'. In: *Encyclopedia of Complexity and Systems Science*. New York, NY: Springer New York, pp. 5239–5265. ISBN: 978-0-387-30440-3. DOI: 10.1007/978-0-387-30440-3_311. URL: https://doi.org/10.1007/978-0-387-30440-3_311.
- Frasca, Marco (Jan. 2008). 'Green Functions and Nonlinear Systems:. Short Time Expansion'. In: *International Journal of Modern Physics A* 23.2, pp. 299–308. DOI: 10. 1142/S0217751X08038160. arXiv: 0704.1568 [hep-th].
- Gary, D. E. and C. U. Keller, eds. (Sept. 2004). *Solar and Space Weather Radiophysics Current Status and Future Developments*. Vol. 314. Astrophysics and Space Science Library.
- Gary, G. Allen (Oct. 2001). 'Plasma Beta above a Solar Active Region: Rethinking the Paradigm'. In: *SoPh* 203.1, pp. 71–86. DOI: 10.1023/A:1012722021820.
- Ginzburg, V. L. and V. V. Zhelezniakov (Oct. 1958). 'On the Possible Mechanisms of Sporadic Solar Radio Emission (Radiation in an Isotropic Plasma)'. In: *Soviet Ast.* 2, p. 653.
- Goldman, M. V. and D. F. Dubois (June 1982). 'Beam-plasma instability in the presence of low-frequency turbulence'. In: *Physics of Fluids* 25, pp. 1062–1072. DOI: 10.1063/1.863839.
- Goldreich, P. and S. Sridhar (Jan. 1995). 'Toward a Theory of Interstellar Turbulence. II. Strong Alfvenic Turbulence'. In: *ApJ* 438, p. 763. doi: 10.1086/175121.
- Goldstein, M. L., D. A. Roberts and W. H. Matthaeus (Jan. 1995). 'Magnetohydrodynamic Turbulence In The Solar Wind'. In: *ARA&A* 33, pp. 283–326. DOI: 10.1146/annurev.aa.33.090195.001435.

Goldstein, Richard M and CT Stelzried (1967). *The superior conjunction of Mariner IV*. Jet Propulsion Laboratory, California Institute of Technology.

- Grognard, R. J. M. (Nov. 1982). 'Numerical Simulation of the Weak Turbulence Excited by a Beam of Electrons in the Interplanetary Plasma'. In: *SoPh* 81.1, pp. 173–180. DOI: 10.1007/BF00151988.
- Gupta, G. R. et al. (Oct. 2012). 'Spectroscopic observations of propagating disturbances in a polar coronal hole: evidence of slow magneto-acoustic waves'. In: *A&A* 546, A93, A93. DOI: 10.1051/0004-6361/201219795. arXiv: 1209.3524 [astroph.SR].
- Hannah, I. G., E. P. Kontar and O. K. Sirenko (Dec. 2009). 'The Effect of Wave-Particle Interactions on Low-Energy Cutoffs in Solar Flare Electron Spectra'. In: *ApJL* 707, pp. L45–L50. doi: 10.1088/0004-637X/707/1/L45. arXiv: 0911.0314 [astro-ph.SR].
- Harrison, R. A. (Dec. 1995). 'The nature of solar flares associated with coronal mass ejection.' In: A&A 304, p. 585.
- Hasselmann, K. and G. Wibberenz (Dec. 1970). 'A Note on the Parallel Diffusion Coefficient'. In: *ApJ* 162, p. 1049. DOI: 10.1086/150736.
- Hassler, Donald M. et al. (Jan. 1990). 'Line Broadening of MG X lambda lambda 609 and 625 Coronal Emission Lines Observed above the Solar Limb'. In: *ApJL* 348, p. L77. DOI: 10.1086/185635.
- Hewish, A. (Jan. 1958). 'The scattering of radio waves in the solar corona'. In: *MNRAS* 118, p. 534. DOI: 10.1093/mnras/118.6.534.
- Hollweg, J. V. (Nov. 1978). 'Some physical processes in the solar wind.' In: *Reviews of Geophysics and Space Physics* 16, pp. 689–720. DOI: 10.1029/RG016i004p00689.
- (Apr. 1986). 'Transition region, corona, and solar wind in coronal holes'. In: *J. Geo-phys. Res.* 91.A4, pp. 4111–4125. DOI: 10.1029/JA091iA04p04111.
- (May 1990). 'Heating of the solar corona.' In: Computer Physics Reports 12.4, pp. 205–232. DOI: 10.1016/0167-7977(90)90011-T.

Holman, G. D. et al. (Sept. 2011). 'Implications of X-ray Observations for Electron Acceleration and Propagation in Solar Flares'. In: *SSRv* 159, pp. 107–166. DOI: 10. 1007/s11214-010-9680-9. arXiv: 1109.6496 [astro-ph.SR].

- Horbury, T. S. et al. (Dec. 1996). 'The rate of turbulent evolution over the Sun's poles.' In: *A&A* 316, pp. 333–341.
- Hughes, M. P. and R. L. Harkness (July 1963). 'Spectral Observations of Solar Radio Bursts.IV. The Exciters of Fast-Drift Bursts.' In: *ApJ* 138, p. 239. doi: 10.1086/147630.
- Ingale, M., P. Subramanian and Iver Cairns (Mar. 2015). 'Coronal turbulence and the angular broadening of radio sources the role of the structure function'. In: MNRAS 447.4, pp. 3486–3497. DOI: 10.1093/mnras/stu2703. arXiv: 1412.6620 [astro-ph.SR].
- Jeffrey, N. L. S. et al. (May 2014). 'On the Variation of Solar Flare Coronal X-Ray Source Sizes with Energy'. In: *ApJ* 787, 86, p. 86. doi: 10.1088/0004-637X/787/1/86. arXiv: 1404.1962 [astro-ph.SR].
- Jeffrey, Natasha L. S., Lyndsay Fletcher and Nicolas Labrosse (May 2016). 'First evidence of non-Gaussian solar flare EUV spectral line profiles and accelerated non-thermal ion motion'. In: *A&A* 590, A99, A99. DOI: 10.1051/0004-6361/201527986. arXiv: 1601.07308 [astro-ph.SR].
- Jokipii, J. R. (Nov. 1966). 'Cosmic-Ray Propagation. I. Charged Particles in a Random Magnetic Field'. In: *ApJ* 146, pp. 480–+. DOI: 10.1086/148912.
- Juan R. Esteban, Ana Rodríguez and Juan L. Vázquez (1988). 'A Nonlinear heat equation with singular diffusivity'. In: *Communications in Partial Differential Equations* 13.8, pp. 985–1039. DOI: 10 . 1080 / 03605308808820566. eprint: https://doi.org/10.1080 / 03605308808820566.
- Kaiser, M. L. et al. (Apr. 2008). 'The STEREO Mission: An Introduction'. In: *SSRv* 136.1-4, pp. 5–16. DOI: 10.1007/s11214-007-9277-0.
- Kaplan, S. A. and V. N. Tsytovich (1973). *Plasma astrophysics*. Oxford: Pergamon Press.

Karlicky, Marian (Jan. 1997). 'Effects of Particle Beams in the Solar Atmosphere'. In: SSRv~81, pp. 143–172. doi: 10.1023/A:1004939526282.

- Kellogg, Paul J. (Mar. 2020). 'Heating of the Solar Wind by Ion Acoustic Waves'.
 In: ApJ 891.1, 51, p. 51. DOI: 10.3847/1538-4357/ab7003. arXiv: 1906.09194
 [physics.space-ph].
- Kellogg, Paul J. et al. (May 1996). 'Early Wind observations of bow shock and fore-shock waves'. In: *Geophys. Res. Lett.* 23.10, pp. 1243–1246. DOI: 10.1029/96GL01067.
- Kheifets, S. (1984). 'APPLICATION OF THE GREEN'S FUNCTION METHOD TO SOME NONLINEAR PROBLEMS OF AN ELECTRON STORAGE RING. PART 1. THE GREEN'S FUNCTION FOR THE FOKKER-PLANCK EQUATION'. In: *Part. Accel.* 15, pp. 67–82.
- Konovalenko, A. et al. (Aug. 2016). 'The modern radio astronomy network in Ukraine: UTR-2, URAN and GURT'. In: *Experimental Astronomy* 42.1, pp. 11–48. DOI: 10. 1007/s10686-016-9498-x.
- Kontar, E. P. (Aug. 2001a). 'Dynamics of electron beams in the inhomogeneous solar corona plasma'. In: *Sol. Phys.* 202, pp. 131–149.
- (Aug. 2001b). 'Dynamics of electron beams in the solar corona plasma with density fluctuations'. In: A&A 375, pp. 629–637. DOI: 10.1051/0004-6361: 20010807.
- Kontar, E. P., V. I. Lapshin and V. N. Melnik (Sept. 1998). 'Numerical and analytical study of the propagation of a monoenergetic electron beam in a plasma'. In: *Plasma Physics Reports* 24.9, pp. 772–776.
- Kontar, E. P. and H. L. Pécseli (June 2002). 'Nonlinear development of electron-beam-driven weak turbulence in an inhomogeneous plasma'. In: *PhRvE* 65.6, pp. 066408–+. DOI: 10.1103/PhysRevE.65.066408.
- Kontar, E. P. et al. (Nov. 2017). 'Imaging spectroscopy of solar radio burst fine structures'. In: *Nature Communications* 8, 1515, p. 1515. DOI: 10.1038/s41467-017-01307-8. arXiv: 1708.06505 [astro-ph.SR].

Kontar, Eduard P. (Aug. 2001c). 'Numerical consideration of quasilinear electron cloud dynamics in plasma'. In: *Computer Physics Communications* 138.3, pp. 222–233. DOI: 10.1016/S0010-4655(01)00214-4. arXiv: 1903.08651 [physics.plasm-ph].

- Kontar, Eduard P., Francesco Azzollini and Olena Lyubchyk (Dec. 2024). 'Advection-nonlinear-diffusion Model of Flare Accelerated Electron Transport in Type III Solar Radio Bursts'. In: *ApJ* 976.2, 233, p. 233. doi: 10.3847/1538-4357/ad8560. arXiv: 2410.11409 [astro-ph.SR].
- Kontar, Eduard P. et al. (Oct. 2019). 'Anisotropic Radio-wave Scattering and the Interpretation of Solar Radio Emission Observations'. In: *ApJ* 884.2, 122, p. 122. doi: 10.3847/1538-4357/ab40bb. arXiv: 1909.00340 [astro-ph.SR].
- Kontar, Eduard P. et al. (Oct. 2023). 'An Anisotropic Density Turbulence Model from the Sun to 1 au Derived from Radio Observations'. In: *ApJ* 956.2, 112, p. 112. doi: 10.3847/1538-4357/acf6c1. arXiv: 2308.05839 [astro-ph.SR].
- Krafft, C. and P. Savoini (May 2023). 'Dynamics of Two-dimensional Type III Electron Beams in Randomly Inhomogeneous Solar Wind Plasmas'. In: *ApJ* 949.1, 24, p. 24. DOI: 10.3847/1538-4357/acc1e4.
- Krall, Nicholas A. and A. W. Trivelpiece (1973). *Principles of plasma physics*. Tokyo: McGraw-Hill.
- Krupar, V. et al. (Aug. 2014). 'Statistical Survey of Type III Radio Bursts at Long Wavelengths Observed by the Solar Terrestrial Relations Observatory (STEREO)/ Waves Instruments: Radio Flux Density Variations with Frequency'. In: *SoPh* 289.8, pp. 3121–3135. doi: 10.1007/s11207-014-0522-x. arXiv: 1410.2053 [astro-ph.SR].
- Krupar, V. et al. (Aug. 2015). 'On the speed and acceleration of electron beams triggering interplanetary type III radio bursts'. In: *A&A* 580, A137, A137. DOI: 10.1051/0004-6361/201425308. arXiv: 1507.06874 [astro-ph.SR].

Krupar, V. et al. (Apr. 2018). 'Interplanetary Type III Bursts and Electron Density Fluctuations in the Solar Wind'. In: *ApJ* 857, 82, p. 82. doi: 10.3847/1538-4357/aab60f.

- Kundu, M. R. and C. L. Spencer (Feb. 1963). 'Spectral Characteristics of Solar Continuum Radiation in the 500-1000 Mc/s Range.' In: *ApJ* 137, p. 572. doi: 10.1086/147530.
- Kundu, M. R. et al. (July 1995). 'Detection of Nonthermal Radio Emission from Coronal X-Ray Jets'. In: *ApJL* 447, p. L135. DOI: 10.1086/309567.
- Kundu, M. R. et al. (Feb. 1998). 'Two-Sided-Loop Type X-ray Jets and Metric Radio Bursts'. In: *SoPh* 178.1, pp. 173–178. DOI: 10.1023/A:1005018109815.
- Kuznetsov, A. A. and E. P. Kontar (Nov. 2019). 'First imaging spectroscopy observations of solar drift pair bursts'. In: *A&A* 631, L7, p. L7. doi: 10.1051/0004-6361/201936447. arXiv: 1910.09864 [astro-ph.SR].
- Kuznetsov, Alexey A. et al. (Aug. 2020). 'Radio Echo in the Turbulent Corona and Simulations of Solar Drift-pair Radio Bursts'. In: *ApJ* 898.2, 94, p. 94. doi: 10.3847/1538-4357/aba04a. arXiv: 2007.14648 [astro-ph.SR].
- Landi, E. and S. R. Cranmer (Jan. 2009). 'Ion Temperatures in the Low Solar Corona: Polar Coronal Holes at Solar Minimum'. In: *ApJ* 691.1, pp. 794–805. doi: 10.1088/0004-637X/691/1/794. arXiv: 0810.0018 [astro-ph].
- Landi, E. et al. (Dec. 2020). 'Hinode/EIS Measurements of Active-region Magnetic Fields'. In: *ApJ* 904.2, 87, p. 87. doi: 10.3847/1538-4357/abbf54. arXiv: 2008.03532 [astro-ph.SR].
- Leblanc, Y. and M. Hoyos (Feb. 1985). 'Storms of U-bursts and the stability of coronal loops'. In: *A&A* 143.2, pp. 365–373.
- Leblanc, Yolande, George A. Dulk and Jean-Louis Bougeret (Nov. 1998). 'Tracing the Electron Density from the Corona to 1 au'. In: *SoPh* 183.1, pp. 165–180. DOI: 10.1023/A:1005049730506.
- Ledenev, V. G. (Dec. 2000). 'On the group delay and the sign of frequency drift of solar type III radio bursts'. In: *SoPh* 197.2, pp. 387–397. DOI: 10.1023/A:1026516413624.

Leer, E., T. E. Holzer and T. Fla (Mar. 1982). 'Acceleration of the solar wind.' In: *SSRv* 33.1-2, pp. 161–200. DOI: 10.1007/BF00213253.

- Li, Bo, Iver H. Cairns and Peter A. Robinson (June 2008). 'Simulations of coronal type III solar radio bursts: 1. Simulation model'. In: *Journal of Geophysical Research* (*Space Physics*) 113.A6, A06104, A06104. DOI: 10.1029/2007JA012957.
- Lin, R. P. (May 1970). 'The Emission and Propagation of 40 keV Solar Flare Electrons. I: The Relationship of 40 keV Electron to Energetic Proton and Relativistic Electron Emission by the Sun'. In: *SoPh* 12.2, pp. 266–303. DOI: 10.1007/BF00227122.
- (June 1974). 'Non-relativistic Solar Electrons'. In: SSRv 16, pp. 189–256. doi: 10.
 1007/BF00240886.
- (Oct. 1985). 'Energetic solar electrons in the interplanetary medium'. In: *SoPh* 100, pp. 537–561. doi: 10.1007/BF00158444.
- Lorfing, Camille Y. and Hamish A. S. Reid (Apr. 2023). 'Solar Electron Beam Velocities That Grow Langmuir Waves in the Inner Heliosphere'. In: *SoPh* 298.4, 52, p. 52. DOI: 10.1007/s11207-023-02145-2.
- Lyubchyk, O. et al. (Sept. 2017). 'Solar Plasma Radio Emission in the Presence of Imbalanced Turbulence of Kinetic-Scale Alfvén Waves'. In: *SoPh* 292.9, 117, p. 117. DOI: 10.1007/s11207-017-1140-1. arXiv: 1707.02295 [physics.space-ph].
- Machin, K. E. and F. G. Smith (Aug. 1952). 'Occultation of a Radio Star by the Solar Corona'. In: *Nature* 170.4321, pp. 319–320. DOI: 10.1038/170319b0.
- Magelssen, G. R. and D. F. Smith (Nov. 1977). 'Nonrelativistic electron stream propagation in the solar atmosphere and type III radio bursts.' In: *SoPh* 55.1, pp. 211–240. DOI: 10.1007/BF00150886.
- Maksimovic, M. et al. (Oct. 2020). 'The Solar Orbiter Radio and Plasma Waves (RPW) instrument'. In: A&A 642, A12, A12. DOI: 10.1051/0004-6361/201936214.
- Mann, G. et al. (Aug. 1999). 'A heliospheric density model and type III radio bursts'. In: A&A 348, pp. 614–620.

Manning, R. and J. Fainberg (Jan. 1980). 'A new method of measuring radio source parameters of a partially polarized distributed source from spacecraft observations'. In: *Space Science Instrumentation* 5, pp. 161–181.

- McLean, D. J. and N. R. Labrum (1985). *Solar radiophysics : studies of emission from the sun at metre wavelengths.*
- McLean, D. J. and D. B. Melrose (1985). 'Propagation of radio waves through the solar corona'. In: *Solar Radiophysics: Studies of Emission from the Sun at Metre Wavelengths*. Ed. by D. J. McLean and N. R. Labrum, pp. 237–251.
- Mejia-Ambriz, J. C. et al. (Sept. 2015). 'Remote-Sensing of Solar Wind Speeds from IPS Observations at 140 and 327 MHz Using MEXART and STEL'. In: *SoPh* 290.9, pp. 2539–2552. DOI: 10.1007/s11207-015-0694-z.
- Mel'nik, V. N. (Jan. 1995). "Gas-dynamic" expansion of a fast-electron flux in a plasma". In: *Plasma Physics Reports* 21.1, pp. 89–91. doi: 10.48550/arXiv.1802.07806. arXiv: 1802.07806 [physics.plasm-ph].
- Mel'nik, V. N. and E. P. Kontar (Mar. 2000). 'To gasdynamic description of a hot electron cloud in a cold plasma'. In: *NewA* 5.1, pp. 35–42. DOI: 10.1016/S1384–1076(00)00004–X.
- Mel'nik, V. N., E. P. Kontar and V. I. Lapshin (Sept. 2000). 'Propagation of a Maxwellian Electron Cloud in a Plasma'. In: *SoPh* 196.1, pp. 199–212. DOI: 10.1023/A: 1005282324985.
- Mel'nik, V. N., V. Lapshin and E. Kontar (Feb. 1999). 'Propagation of a Monoenergetic Electron Beam in the Solar Corona'. In: *SoPh* 184.2, pp. 353–362. DOI: 10.1023/A: 1005191910544.
- Melnik, V. N. et al. (Sept. 2005). 'Solar Drift Pair Bursts in the Decameter Range'. In: *SoPh* 231.1-2, pp. 143–155. doi: 10.1007/s11207-005-8272-4.
- Melnik, V. N. et al. (Jan. 2010). 'Type IIIb bursts and their fine structure in frequency band 18-30 MHz'. In: *American Institute of Physics Conference Series*. Ed. by S. K. Chakrabarti, A. I. Zhuk and G. S. Bisnovatyi-Kogan. Vol. 1206. American Institute of Physics Conference Series, pp. 445–449. DOI: 10.1063/1.3292552.

Melnik, V. N. et al. (Apr. 2011). 'Observations of Powerful Type III Bursts in the Frequency Range 10 - 30 MHz'. In: *SoPh* 269.2, pp. 335–350. DOI: 10.1007/s11207-010-9703-4.

- Melnik, V. N. et al. (Jan. 2015). 'Decameter Type III Bursts with Changing Frequency Drift-Rate Signs'. In: *SoPh* 290.1, pp. 193–203. DOI: 10.1007/s11207-014-0577-8. arXiv: 1802.08336 [astro-ph.SR].
- Melrose, D. B. (Dec. 2017). 'Coherent emission mechanisms in astrophysical plasmas'. In: *Reviews of Modern Plasma Physics* 1.1, 5, p. 5. DOI: 10.1007/s41614-017-0007-0. arXiv: 1707.02009 [physics.plasm-ph].
- Morabito, D. D. et al. (Feb. 2003). 'The Cassini May 2000 solar conjunction'. In: *IEEE Transactions on Antennas and Propagation* 51.2, pp. 201–219. DOI: 10.1109/TAP.2003. 809055.
- Mulay, Sargam M. et al. (May 2016). 'Multiwavelength study of 20 jets that emanate from the periphery of active regions'. In: *A&A* 589, A79, A79. DOI: 10.1051/0004-6361/201527473. arXiv: 1602.00151 [astro-ph.SR].
- Müller, D. et al. (Oct. 2020). 'The Solar Orbiter mission. Science overview'. In: *A&A* 642, A1, A1. DOI: 10.1051/0004-6361/202038467. arXiv: 2009.00861 [astroph.SR].
- Muschietti, L. (Dec. 1990). 'Electron Beam Formation and Stability'. In: *SoPh* 130.1-2, pp. 201–228. DOI: 10.1007/BF00156790.
- Muschietti, L., M. V. Goldman and D. Newman (Mar. 1985). 'Quenching of the Beam Plasma Instability by Largescale Density Fluctuations in Three Dimensions'. In: *SoPh* 96.1, pp. 181–198. DOI: 10.1007/BF00239800.
- Musset, S. et al. (Dec. 2021). 'Simulations of radio-wave anisotropic scattering to interpret type III radio burst data from Solar Orbiter, Parker Solar Probe, STEREO, and Wind'. In: *A&A* 656, A34, A34. DOI: 10.1051/0004-6361/202140998. arXiv: 2109.13713 [astro-ph.SR].

Newkirk Jr., G. (May 1961). 'The Solar Corona in Active Regions and the Thermal Origin of the Slowly Varying Component of Solar Radio Radiation.' In: *ApJ* 133, p. 983. doi: 10.1086/147104.

- Nindos, A. et al. (Oct. 2000). 'Soft X-Ray and Gyroresonance Emission above Sunspots'. In: *ApJS* 130.2, pp. 485–499. DOI: 10.1086/317355.
- Okubo, A., J. Mitchell and V. Andreasen (Oct. 1984). 'Chaos-induced turbulent diffusion'. In: *Physics Letters A* 105.4-5, pp. 169–172. DOI: 10.1016/0375-9601(84)90389-X.
- Papadopoulos, K., M. L. Goldstein and R. A. Smith (May 1974). 'Stabilization of Electron Streams in Type III Solar Radio Bursts'. In: *ApJ* 190, pp. 175–186. doi: 10.1086/152862.
- Parker, E. N. (Dec. 1957). 'Sweet's Mechanism for Merging Magnetic Fields in Conducting Fluids'. In: *J. Geophys. Res.* 62.4, pp. 509–520. DOI: 10.1029/JZ062i004p00509.
- (Nov. 1958). 'Dynamics of the Interplanetary Gas and Magnetic Fields.' In: *ApJ* 128, pp. 664-+. DOI: 10.1086/146579.
- (Nov. 1960). 'The Hydrodynamic Theory of Solar Corpuscular Radiation and Stellar Winds.' In: *ApJ* 132, p. 821. doi: 10.1086/146985.
- Parker, Eugene N. (Sept. 1955a). 'Hydromagnetic Dynamo Models.' In: *ApJ* 122, p. 293. DOI: 10.1086/146087.
- (Mar. 1955b). 'The Formation of Sunspots from the Solar Toroidal Field.' In: *ApJ* 121, p. 491. DOI: 10.1086/146010.
- Pécseli, Hans (2012). *Waves and Oscillations in Plasmas*. Boca Raton: CRC Press. DOI: 10.1201/b12702.
- Poquérusse, M. et al. (July 1996). 'Ulysses-ARTEMIS radio observation of energetic flare electrons'. In: *Proceedings of the eigth International solar wind Conference: Solar wind eight*. Ed. by D. Winterhalter et al. Vol. 382. American Institute of Physics Conference Series. AIP, pp. 62–65. DOI: 10.1063/1.51360.
- Press, William H., Brian P. Flannery and Saul A. Teukolsky (1986). *Numerical recipes*. *The art of scientific computing*.

Priest, Eric (2014). *Magnetohydrodynamics of the Sun*. DOI: 10.1017/CB09781139020732.

- Ratcliffe, H., N. H. Bian and E. P. Kontar (Dec. 2012). 'Density Fluctuations and the Acceleration of Electrons by Beam-generated Langmuir Waves in the Solar Corona'. In: *ApJ* 761, 176, p. 176. DOI: 10.1088/0004-637X/761/2/176. arXiv: 1211.2587 [astro-ph.SR].
- Ratcliffe, H., E. P. Kontar and H. A. S. Reid (Dec. 2014). 'Large-scale simulations of solar type III radio bursts: flux density, drift rate, duration, and bandwidth'. In: *A&A* 572, A111, A111. DOI: 10.1051/0004-6361/201423731. arXiv: 1410.2410 [astro-ph.SR].
- Reid, Hamish A. S. and Eduard P. Kontar (Sept. 2010). 'Solar Wind Density Turbulence and Solar Flare Electron Transport from the Sun to the Earth'. In: *ApJ* 721.1, pp. 864–874. DOI: 10.1088/0004-637X/721/1/864. arXiv: 1007.5310 [astroph.SR].
- (July 2013). 'Evolution of the Solar Flare Energetic Electrons in the Inhomogeneous Inner Heliosphere'. In: SoPh 285.1-2, pp. 217–232. DOI: 10.1007/s11207-012-0013-x. arXiv: 1209.5347 [astro-ph.SR].
- (June 2018). 'Solar type III radio burst time characteristics at LOFAR frequencies and the implications for electron beam transport'. In: *A&A* 614, A69, A69. DOI: 10. 1051/0004-6361/201732298. arXiv: 1802.01507 [astro-ph.SR].
- Reid, Hamish A. S., Nicole Vilmer and Eduard P. Kontar (July 2014). 'The low-high-low trend of type III radio burst starting frequencies and solar flare hard X-rays'. In: *A&A* 567, A85, A85. DOI: 10.1051/0004-6361/201321973. arXiv: 1403.1839 [astro-ph.SR].
- Riddle, A. C. (1974). 'On the Observation of Scattered Radio Emission from Sources in the Solar Corona'. In: *SoPh* 35.1, pp. 153–169. DOI: 10.1007/BF00156964.
- Roberts, J. A. (June 1958). 'Evidence of Echoes in the Solar Corona from a New Type of Burst'. In: *Australian Journal of Physics* 11, p. 215. DOI: 10.1071/PH580215.
- Ryutov, D. D. (Jan. 1969). 'Quasilinear Relaxation of an Electron Beam in an Inhomogeneous Plasma'. In: *Soviet Journal of Experimental and Theoretical Physics* 30, p. 131.

Ryutov, D. D. (Oct. 2018). 'Scaling laws for dynamical plasma phenomena'. In: *Physics of Plasmas* 25.10, 100501, p. 100501. DOI: 10.1063/1.5042254.

- Ryutov, D. D. and R. Z. Sagdeev (1970). 'Quasi-gasdynamical Description of a Hot Electron Cloud in a Cold Plasma'. In: *Soviet Journal of Experimental and Theoretical Physics* 31, pp. 396–+.
- Sagdeev, R. Z. and A. A. Galeev (1969). Nonlinear Plasma Theory. New York: Benjamin.
- Saito, K., A. I. Poland and R. H. Munro (Nov. 1977). 'A study of the background corona near solar minimum.' In: *SoPh* 55.1, pp. 121–134. DOI: 10.1007/BF00150879.
- Sasikumar Raja, K. et al. (Dec. 2017). 'Turbulent Density Fluctuations and Proton Heating Rate in the Solar Wind from 9-20 R $_{\odot}$ '. In: *ApJ* 850.2, 129, p. 129. doi: 10. 3847/1538-4357/aa94cd. arXiv: 1710.06295 [astro-ph.SR].
- Sasikumar Raja, K. et al. (Jan. 2022). 'Spectral Analysis of Solar Radio Type III Bursts from 20 kHz to 410 MHz'. In: *ApJ* 924.2, 58, p. 58. DOI: 10.3847/1538-4357/ac34ed. arXiv: 2110.10935 [astro-ph.SR].
- Sauer, Konrad et al. (Jan. 2019). 'Parametric Decay of Beam-Generated Langmuir Waves and Three-Wave Interaction in Plateau Plasmas: Implications for Type III Radiation'. In: *Journal of Geophysical Research* (*Space Physics*) 124.1, pp. 68–89. DOI: 10.1029/2018JA025887.
- Schlickeiser, R. (Jan. 1989). 'Cosmic-ray transport and acceleration. I Derivation of the kinetic equation and application to cosmic rays in static cold media. II Cosmic rays in moving cold media with application to diffusive shock wave acceleration'. In: *ApJ* 336, pp. 243–293. DOI: 10.1086/167009.
- Schmahl, E. J. (Mar. 1972). 'A Model of the Evolution of the Flux Density and Polarization in Isolated Moving Type IV Bursts'. In: *PASA* 2.2, pp. 95–98. doi: 10.1017/S1323358000013035.
- Schwenn, Rainer (Dec. 2006). 'Space Weather: The Solar Perspective'. In: *Living Reviews in Solar Physics* 3.1, 2, p. 2. doi: 10.12942/1rsp-2006-2.

Seely, J. F. et al. (July 1997). 'Turbulent Velocities and Ion Temperatures in the Solar Corona Obtained from SUMER Line Widths'. In: *ApJL* 484.1, pp. L87–L90. DOI: 10.1086/310769.

- Sharykin, I. N., E. P. Kontar and A. A. Kuznetsov (Aug. 2018). 'LOFAR Observations of Fine Spectral Structure Dynamics in Type IIIb Radio Bursts'. In: *SoPh* 293.8, 115, p. 115. DOI: 10.1007/s11207-018-1333-2. arXiv: 1806.01046 [astro-ph.SR].
- Shen, Yuandeng (Feb. 2021). 'Observation and modelling of solar jets'. In: *Proceedings of the Royal Society of London Series A* 477.2246, p. 217. DOI: 10.1098/rspa.2020.0217. arXiv: 2101.04846 [astro-ph.SR].
- Shibata, K., T. Yokoyama and M. Shimojo (July 1994). 'Coronal X-ray Jets'. In: *Proceedings of Kofu Symposium*, pp. 75–78.
- Shibata, Kazunari et al. (Oct. 1992). 'Observations of X-Ray Jets with the YOHKOH Soft X-Ray Telescope'. In: *PASJ* 44, pp. L173–L179.
- Singh, Jagdev et al. (May 2011). 'Spectroscopic Observation of Oscillations in the Corona During the Total Solar Eclipse of 22 July 2009'. In: *SoPh* 270.1, 213, p. 213. DOI: 10.1007/s11207-011-9732-7.
- Steinberg, J. L. et al. (Feb. 1971). 'Coronal Scattering, Absorption and Refraction of Solar Radiobursts'. In: *A&A* 10, p. 362.
- Stewart, R. T. (Feb. 1975). 'An Example of a Fundamental Type IIIb Radio Burst'. In: *SoPh* 40.2, pp. 417–419. DOI: 10.1007/BF00162388.
- Sturrock, P. A. (1964). 'Type III Solar Radio Bursts'. In: *NASA Special Publication* 50, p. 357.
- Stverak, S., Pavel M. Trávníček and Petr Hellinger (Oct. 2015). 'Electron energetics in the expanding solar wind via Helios observations'. In: *Journal of Geophysical Research* (*Space Physics*) 120.10, pp. 8177–8193. DOI: 10.1002/2015JA021368.
- Suzuki, S. and D. E. Gary (Jan. 1979). 'Position and polarization of solar drift pair bursts'. In: *PASA* 3.5-6, pp. 379–383. DOI: 10.1017/S1323358000026151.

Sweet, P. A. (1958). 'The Neutral Point Theory of Solar Flares'. In: *Electromagnetic Phenomena in Cosmical Physics*. Ed. by B. Lehnert. Vol. 6. IAU Symposium, pp. 123–+.

- Takakura, T. (Jan. 1961). 'Acceleration of Electrons in the Solar Atmosphere and Type IV Radio Outbursts'. In: *PASJ* 13, p. 166.
- (May 1982). 'Numerical Simulation of Type-Iii Solar Radio Bursts on Meter-Waves and Hectometer-Waves'. In: SoPh 78.1, pp. 141–156. DOI: 10.1007/BF00151150.
- Takakura, T. and K. Kai (Jan. 1961). 'Spectra of Solar Radio Type IV Bursts'. In: *PASJ* 13, p. 94.
- Takakura, T. and H. Shibahashi (Feb. 1976). 'Dynamics of a Cloud of Fast Electrons Travelling Through the Plasma'. In: *SoPh* 46.2, pp. 323–346. DOI: 10.1007/BF00149860.
- Tasnim, Samira et al. (Apr. 2022). 'Density Turbulence and the Angular Broadening of Outer Heliospheric Radio Sources at High Latitudes and in the Ecliptic Plane'. In: *ApJ* 928.2, 125, p. 125. doi: 10.3847/1538-4357/ac5031.
- Tennekes, H. (Feb. 1975). 'Eulerian and Lagrangian time microscales in isotropic turbulence'. In: *Journal of Fluid Mechanics* 67, pp. 561–567. DOI: 10.1017/S0022112075000468.
- Thapa, Tulsi and Yihua Yan (Sept. 2024). 'Time Profile Study of Type III Solar Radio Bursts Using Parker Solar Probe'. In: *ApJ* 972.1, 2, p. 2. doi: 10.3847/1538-4357/ad5e77.
- Thejappa, G., R. J. MacDowall and M. L. Kaiser (Dec. 2007). 'Monte Carlo Simulation of Directivity of Interplanetary Radio Bursts'. In: *ApJ* 671, pp. 894–906. doi: 10. 1086/522664.
- Thompson, W. T. (Apr. 2006). 'Coordinate systems for solar image data'. In: *A&A* 449, pp. 791–803. DOI: 10.1051/0004–6361:20054262.
- Timofeev, I. V., V. V. Annenkov and A. V. Arzhannikov (Nov. 2015). 'Regimes of enhanced electromagnetic emission in beam-plasma interactions'. In: *Physics of Plasmas* 22.11, 113109, p. 113109. DOI: 10.1063/1.4935890.

Tomczyk, S. and S. McIntosh (Dec. 2008). 'Time Distance Coronal Seismology With the CoMP Instrument'. In: *AGU Fall Meeting Abstracts*. Vol. 2008, SH11A-01, SH11A-01.

- Treumann, Rudolf A. (July 1997). 'Theory of super-diffusion for the magnetopause'. In: *Geophys. Res. Lett.* 24.14, pp. 1727–1730. DOI: 10.1029/97GL01760.
- Tsytovich, V. N. (1995). *Lectures on Non-linear Plasma Kinetics*. Ed. by Tsytovich, V. N. & ter Haar, D.
- Tu, C. Y. and E. Marsch (July 1995). 'Magnetohydrodynamic Structures Waves and Turbulence in the Solar Wind Observations and Theories'. In: *SSRv* 73.1-2, pp. 1–210. DOI: 10.1007/BF00748891.
- van de Hulst, H. C. (Feb. 1950). 'The electron density of the solar corona'. In: *BAN* 11, p. 135.
- van Haarlem, M. P. et al. (2013). 'LOFAR: The LOw-Frequency ARray'. In: *A&A* 556, A2, A2. DOI: 10.1051/0004-6361/201220873. arXiv: 1305.3550 [astro-ph.IM].
- Vázquez, Juan Luis (2017). 'The Mathematical Theories of Diffusion: Nonlinear and Fractional Diffusion'. In: Nonlocal and Nonlinear Diffusions and Interactions: New Methods and Directions: Cetraro, Italy 2016. Cham: Springer International Publishing, pp. 205–278. ISBN: 978-3-319-61494-6. DOI: 10.1007/978-3-319-61494-6_5. arXiv: 1706.08241 [math.AP]. URL: https://doi.org/10.1007/978-3-319-61494-6_5.
- Vecchio, A. et al. (Dec. 2021). 'Solar Orbiter/RPW antenna calibration in the radio domain and its application to type III burst observations'. In: *A&A* 656, A33, A33. DOI: 10.1051/0004-6361/202140988. arXiv: 2109.07947 [astro-ph.SR].
- Vedenov, A. A., A. V. Gordeev and L. I. Rudakov (Jan. 1967). 'Oscillations and instability of a weakly turbulent plasma'. In: *Plasma Physics* 9.6, pp. 719–735. DOI: 10.1088/0032-1028/9/6/305.
- Vedenov, A. A. and E. P. Velikhov (1963). 'Quasilinear Approximation in the Kinetic Theory of a Low-density Plasma'. In: *Soviet Journal of Experimental and Theoretical Physics* 16, p. 682.

Vedenov, A. A., E. P. Velikhov and Roal'd. Z. Sagdeev (Feb. 1961). 'Special Issue: Stability of Plasma'. In: *Soviet Physics Uspekhi* 4.2, pp. 332–369. DOI: 10.1070/PU1961v004n02ABEH003341.

- Verscharen, D., K. G. Klein and B. Maruca (Dec. 2018). 'The Multi-Scale Nature of the Solar Wind'. In: *AGU Fall Meeting Abstracts*. Vol. 2018. AGU Fall Meeting Abstracts, SH53A-07, SH53A-07.
- Šafránková, J. et al. (Apr. 2015). 'Solar Wind Density Spectra around the Ion Spectral Break'. In: *ApJ* 803.2, 107, p. 107. DOI: 10.1088/0004-637X/803/2/107.
- Wang, T. J., L. Ofman and J. M. Davila (May 2009). 'Propagating Slow Magnetoacoustic Waves in Coronal Loops Observed by Hinode/EIS'. In: *ApJ* 696.2, pp. 1448–1460.

 DOI: 10.1088/0004-637X/696/2/1448. arXiv: 0902.4480 [astro-ph.SR].
- Weber, R. R. (Oct. 1978). 'Low frequency spectra of type III solar radio bursts.' In: *SoPh* 59.2, pp. 377–385. DOI: 10.1007/BF00951843.
- Weiss, Late A. A. and R. T. Stewart (Apr. 1965). 'Solar radio bursts of spectral type V'. In: *Australian Journal of Physics* 18, p. 143. DOI: 10.1071/PH650143.
- West, Matthew J. et al. (June 2023). 'Defining the Middle Corona'. In: *SoPh* 298.6, 78, p. 78. doi: 10.1007/s11207-023-02170-1. arXiv: 2208.04485 [astro-ph.SR].
- Wexler, D. et al. (Aug. 2020). 'Coronal Electron Density Fluctuations Inferred from Akatsuki Spacecraft Radio Observations'. In: *SoPh* 295.8, 111, p. 111. doi: 10.1007/s11207-020-01677-1.
- Wexler, David B. et al. (Feb. 2019). 'Spacecraft Radio Frequency Fluctuations in the Solar Corona: A MESSENGER-HELIOS Composite Study'. In: *ApJ* 871.2, 202, p. 202. DOI: 10.3847/1538-4357/aaf6a8.
- Wheatland, M. S., P. A. Sturrock and L. W. Acton (June 1997). 'Coronal Heating and the Vertical Temperature Structure of the Quiet Corona'. In: *ApJ* 482.1, pp. 510–518. DOI: 10.1086/304133.
- White, S. M. et al. (Sept. 2002). 'The Physical Properties of a Flaring Loop'. In: *ApJ* 576.1, pp. 505–518. DOI: 10.1086/341621.

Whiting, E.E. (1968). 'An empirical approximation to the Voigt profile'. In: *Journal of Quantitative Spectroscopy and Radiative Transfer* 8.6, pp. 1379–1384. ISSN: 0022-4073.

DOI: https://doi.org/10.1016/0022-4073(68)90081-2. URL: https://www.sciencedirect.com/science/article/pii/0022407368900812.

- Wild, J. P. (Dec. 1950). 'Observations of the Spectrum of High-Intensity Solar Radiation at Metre Wavelengths. III. Isolated Bursts'. In: *Australian Journal of Scientific Research A Physical Sciences* 3, p. 541. DOI: 10.1071/PH500541.
- Wild, J. P. and L. L. McCready (Sept. 1950). 'Observations of the Spectrum of High-Intensity Solar Radiation at Metre Wavelengths. I. The Apparatus and Spectral Types of Solar Burst Observed'. In: Australian Journal of Scientific Research A Physical Sciences 3, p. 387. DOI: 10.1071/CH9500387.
- Wilson III, Lynn B. et al. (May 2021). 'A Quarter Century of Wind Spacecraft Discoveries'. In: *Reviews of Geophysics* 59.2, e2020RG000714. DOI: 10.1029/2020RG00071410. 1002/essoar.10504309.2.
- Withbroe, G. L. and R. W. Noyes (Jan. 1977). 'Mass and energy flow in the solar chromosphere and corona.' In: *ARA&A* 15, pp. 363–387. DOI: 10.1146/annurev. aa.15.090177.002051.
- Withbroe, George L. (Feb. 1988). 'The Temperature Structure, Mass, and Energy Flow in the Corona and Inner Solar Wind'. In: *ApJ* 325, p. 442. doi: 10.1086/166015.
- Wohlmuth, R. et al. (May 2001). 'Radio Frequency Fluctuation Spectra During the Solar Conjunctions of the Ulysses and Galileo Spacecraft'. In: *SSRv* 97, pp. 9–12. DOI: 10.1023/A:1011845221808.
- Woo, R. (Jan. 1978). 'Radial dependence of solar wind properties deduced from Helios 1/2 and Pioneer 10/11 radio scattering observations.' In: *ApJ* 219, pp. 727–739. DOI: 10.1086/155831.
- Woo, R. and J. W. Armstrong (Dec. 1979). 'Spacecraft radio scattering observations of the power spectrum of electron density fluctuations in the solar wind'. In: *J. Geophys. Res.* 84.A12, pp. 7288–7296. DOI: 10.1029/JA084iA12p07288.

Woo, R., F. C. Yang and A. Ishimaru (Dec. 1976). 'Structure of density fluctuations near the sun deduced from Pioneer-6 spectral broadening measurements.' In: *ApJ* 210, pp. 593–602. DOI: 10.1086/154864.

- Woo, Richard (Mar. 1996). 'Structure in the Solar Corona from Radio Scintillation Measurements'. In: *Ap&SS* 243.1, p. 97. doi: 10.1007/BF00644038.
- Woo, Richard and Paul Gazis (Dec. 1993). 'Large-scale solar-wind structure near the Sun detected by Doppler scintillation'. In: *Nature* 366.6455, pp. 543–545. DOI: 10.1038/366543a0.
- Yakovlev, O. I. et al. (Aug. 1980). 'Inhomogeneous Structure and Velocity of the Circumsolar Plasma Based on VENERA-10'. In: *Soviet Ast.* 24, p. 454.
- Yashiro, S. et al. (July 2004). 'A catalog of white light coronal mass ejections observed by the SOHO spacecraft'. In: *Journal of Geophysical Research (Space Physics)* 109.A7, A07105, A07105. DOI: 10.1029/2003JA010282.
- Yashiro, S. et al. (Oct. 2006). 'Different Power-Law Indices in the Frequency Distributions of Flares with and without Coronal Mass Ejections'. In: *ApJL* 650.2, pp. L143–L146. DOI: 10.1086/508876. arXiv: astro-ph/0609197 [astro-ph].
- Yoon, P. H. et al. (Nov. 2012). 'Langmuir Turbulence and Suprathermal Electrons'. In: *SSRv* 173.1-4, pp. 459–489. DOI: 10.1007/s11214-012-9867-3.
- Zaitsev, V. V., N. A. Mityakov and V. O. Rapoport (June 1972). 'A Dynamic Theory of Type III Solar Radio Bursts'. In: *SoPh* 24, pp. 444–456. DOI: 10.1007/BF00153387.
- Zakharov, V. E. (Jan. 1972). 'Collapse of Langmuir Waves'. In: *Soviet Journal of Experimental and Theoretical Physics* 35, p. 908.
- Zank, Gary P. et al. (Mar. 2024). 'Characterization of Turbulent Fluctuations in the Sub-Alfvenic Solar Wind'. In: *arXiv e-prints*, arXiv:2403.14861, arXiv:2403.14861. DOI: 10.48550/arXiv.2403.14861. arXiv: 2403.14861 [astro-ph.SR].
- Zheleznyakov, V. V. and V. V. Zaitsev (Aug. 1968). 'The Origin of Type-V Solar Radio Bursts.' In: *Soviet Ast.* 12, p. 14.
- (Aug. 1970). 'Contribution to the Theory of Type III Solar Radio Bursts. I.' In: So-viet Ast. 14, pp. 47-+.

Ziebell, L. F., R. Gaelzer and P. H. Yoon (Mar. 2008). 'Dynamics of Langmuir wave decay in two dimensions'. In: *Physics of Plasmas* 15.3, 032303, p. 032303. DOI: 10.1063/1.2844740.

- Ziebell, L. F. et al. (Aug. 2011). 'Two-dimensional quasilinear beam-plasma instability in inhomogeneous media'. In: *Plasma Physics and Controlled Fusion* 53.8, 085004, p. 085004. DOI: 10.1088/0741-3335/53/8/085004.
- Zimbardo, G., P. Pommois and P. Veltri (Mar. 2006). 'Superdiffusive and Subdiffusive Transport of Energetic Particles in Solar Wind Anisotropic Magnetic Turbulence'. In: *ApJL* 639.2, pp. L91–L94. doi: 10.1086/502676.